Utilising Atomic Layer Deposition (ALD) to Develop Efficient Hematite-based Photoanodes for Photocatalytic Water-Splitting

Thesis submitted in accordance with the requirements of the University of Liverpool for the degree of Doctor in Philosophy by

Natalie Leah Bavis

March 2023

Supervisors:

Dr Richard J. Potter

Prof. Alex Cowan

UNIVERSITY OF LIVERPOOL

Contents

Abstract

Utilising Atomic Layer Deposition (ALD) to Develop Efficient Hematite-based Photoanodes for Photocatalytic Water-Splitting

Natalie Bavis

It is a scientific consensus that the consumption of fossil fuels result in carbon dioxide (CO_2) emissions that negatively impact the climate, in a phenomenon referred to as 'global warming' or 'climate change'.[1] To address this problem, novel fuels are required that have a lowered carbon footprint, with hydrogen often hailed as future fuel of combustion vehicles.[2] However, a low carbon, renewable means of hydrogen production is required to fully address this problem.[3] Water-splitting using solar energy offers a route to renewable, clean hydrogen production.

Hematite, α-Fe_2O_3, is an n-type semiconductor that shows promise as a photoanode in a water-splitting photoelectrochemical cell. Cheap, stable, abundant and with a suitable bandgap, α-Fe_2O_3 possesses many of the desirable criteria for use in this context.[4] However, it is also plagued with electronic issues such as poor charge transport, short carrier lifetimes and low conductivity. [5] This work attempts to address these problems by using plasma enhanced atomic layer deposition (PEALD) to produce nanostructured hematite films with improved properties. Using a ferrocene precursor in a vapour push setup, a process was designed with a pulse purge sequence of 2-5-5-4s (precursor-purge-coreactant-purge) and 0.05nm/cycle growth rate.

The performance of the films was then assessed using photoelectrochemical techniques, with film modifications, including Al_2O_3 underlayers and interlayer doping, explored as a means of improving performance. Specifically, a 0.5nm underlayer was found to improve photocurrent dramatically, exhibiting a peak performance of 1.29 mA cm^{-2} at 0.7 $V_{Ag/AgCl}$, coupled with a ~250mV cathodic shift in onset potential from the non-modified Fe_2O_3. Layer or delta doping with Al_2O_3 offered further improvements in onset potential, with the addition of discrete, 1.2nm thick Al_2O_3 interlayers generating an impressive V_{Onset} of 0.73 V_{RHE}. This was further lowered to 0.61 V_{RHE} with the addition of a CoPi surface layer.

Finally, the effects of heat exposure are addressed, with low energy ion scattering (LEIS) spectroscopy employed to discern compositional changes in the films following heating. Key observations here were the heat-induced migration of aluminium from the underlayers, as well as the suppression of Sn migration from the FTO substrate. In particular, these suppression effects were pronounced for the ALD films compared to other methods of deposition. This provided insight into the mechanisms behind the photoelectrochemical improvements witnessed, while raising questions on the effects of heat exposure on hematite/FTO based photoanodes.

Acknowledgements

There are multiple people that I would like to thank for their help and support throughout this PhD.

Firstly, I would like to thank my supervisor Dr. Richard Potter for giving me this opportunity and for his guidance from the very start. Richard has been the most understanding and dedicated supervisor I could have asked for. I'd also like to thank my other supervisor Prof. Alex Cowan for navigating me through the difficult world of electrochemistry. I wouldn't have been able to finish this without their help.

Secondly, I'd like to thank everyone in George Holt, for being the most resilient bunch of scientists I've ever met. Morning tea breaks were the highlight of this project and I thank everyone who ever gave me advice or insight into my PhD. In no particular order, Dr Tim Joyce, Dr Tim Bullough, Dr Paul Marshall, Dr Sophia Chalker, Prof Paul Chalker, Dave Atkinson, Dr Benjamin Peek; I couldn't have asked for better people to spend 4 years of my life working with.

I'd especially like to thank Dr. Matt Werner, for not only helping me with LEIS and clean room issues, but also for keeping me sane during the pandemic - sun bites and The Martian singlehandedly kept me going when I wanted to quit.

I'd also like to thank Dr Adrian Gardner for his work on LEIS and his thorough reviews of my thesis – I appreciate all the extra help.

I'm thankful to all of the colleagues and collaborators who provided measurements and expertise: Dr Shamsal Haq for XPS analysis, Dr Joseph

Horne for Raman, Dr SocMan Ho-Kimura for electrodeposition and Dr Keith Arnold and Dr Matt Bilton for helping with SEM. I'd like to thank everyone at the Stephenson Institute for offering advice and help when needed, and everyone at the Leverhulme Institute for processing orders and organizing fun meetings.

Finally, I'd like to thank some of my friends and family for their support during this project. Shaun for putting up with me at my most stressed, Joe for distracting me during the harder times, 'The Herd' for keeping me supplied with memes to make me laugh when I wanted to cry and Ryan for bringing me cake when I needed it most. You guys are the best.

Abbreviations

ALD	Atomic layer deposition
CB	Conduction band
α-Fe2O3	Iron oxide (Hematite)
FTO	Fluorine doped tin oxide
HER	Hydrogen evolution reaction
LEIS	Low Energy Ion Scattering
LSV	Linear Sweep Voltammetry
NHE	Standard hydrogen electrode
OER	Oxygen evolution reaction
PEC	Photoelectrochemical
RHE	Reversible hydrogen electrode
SEM	Scanning electron microscopy
STH	Solar to hydrogen
TA	Transient absorption
TMA	Trimethylaluminium
UV	Ultraviolet
XRD	X-ray diffraction
VB	Valence band
Vis	Visible

Chapter 1: Introduction

1.0 Foreword

This project aims to further the green hydrogen agenda by exploring the benefits of modified hematite photoanodes. Using plasma enhanced atomic layer deposition, novel structures are produced that exhibit interesting behaviour, while low energy ion scattering offers deep insight into the mechanisms of action.

1.1 The Future of Renewable Energy

As technology advances and global populations surge, so too does the need for additional energy sources. In 2019 there was a 2.9% increase in global energy consumption from the previous year; the largest incremental growth in a decade.[1] Since 2010, the human population has grown by almost 1 billion people, with the forecast by 2030 to be 8.5 billion.[2] In continuing with this trend and working under the assumption that as the population increases so too will global energy requirements, then fossil fuel consumption will need to surge to meet this growing demand.

It is the scientific consensus that fossil fuel combustion results in carbon dioxide (CO_2) emissions that negatively impact the global climate, in a phenomenon referred to as 'global warming 'or 'climate change'.[3] Fossil fuels follow a typical combustion reaction, with majority products of CO_2 and H_2O, along with other trace compounds. CO_2 then effectively forms a 'layer 'in the upper atmosphere, allowing the radiation from the sun to enter, but not efficiently exit the atmosphere of the Earth.[4] This 'trapped', reflected radiation increases the temperature of the planet, while simultaneously being absorbed by sea ice, resulting in melting that will increase sea levels and negatively impact the global climate.[5] This effect is predicted to compound as the ice melts, since the ice itself serves to reflect a large portion of the radiation away from itself.[6] Removing excess CO_2 from the atmosphere is a difficult task with current technology and deforestation hinders this removal further.[7] Furthermore, ocean acidification is yet one more problem caused by an excess of atmospheric carbon dioxide.[8] Using this knowledge it is clear that alternatives to fossil fuels are needed to reduce and potentially reverse these effects. Low carbon technologies such as wind, geothermal, tidal, nuclear and solar power are a few of the many methods that can replace fossil fuels for grid energy production.[9] Yet, these methods do not fully remove the need for fossil fuel combustion in mobile vehicles.

In 2017, EU emissions from transportation accounted for 27% of greenhouse gas emissions, an increase of 2.2% from 2016 levels, and almost 72% of these were due to road emissions from cars.[10] In the UK around 70% of oil consumption from 2018 was caused by the transport sector and from March 2018 to 2019 there was a 1.4% jump in licensed vehicles on the road, with around 850,000 more vehicles licensed every year.[11] In looking to these statistics one clear way to improve on emissions would be to find an alternative energy source to oil. Hydrogen powered vehicles have long been hailed as the solution to renewably powered transportation. Unlike typical electrical vehicles, hydrogen fueled engines are not limited by battery technology. Clean burning, reasonably stable for storage and with the potential for use in filling stations, hydrogen power combines the best aspects of fossil fuels with a renewable and carbon free edge.[12] However, many methods of extracting hydrogen gas are just as ‘dirty ’of an energy source as conventional fossil fuels, with around 95% of hydrogen acquired from natural gas or coal.[13,14] The environmental costs of such extraction are enormous, with high temperature and pressure requirements, along with higher carbon emissions than simply combusting the methane.[15,16] The solution to this is using renewable energy technologies to acquire hydrogen from water, removing the need for fossil fuels from every stage of the process.[17]

1.2 Water Splitting

Water is an abundant planetary resource that can be split into two useful, non-polluting elements: hydrogen and oxygen. The overall reaction is:

$$H_2O_{(l)} \rightarrow \frac{1}{2}O_{2\,(g)} + H_{2\,(g)} \quad (1)$$

However, each product is made in an individual step, called either the oxygen evolution reaction (OER) [Eq. 2] or hydrogen evolution reaction (HER) [Eq.3]. As the H^+ ions produced in the OER are required for the HER, and the hole formation step of the OER is very slow, the former reaction is usually considered the rate limiting one.[18–20]

$$2H_2O_{(l)} \rightarrow O_{2\,(g)} + 4H^+_{(aq)} + 4e^- \quad (2)$$

$$2H^+_{(aq)} + 2e^- \rightarrow H_{2\,(g)} \quad (3)$$

Due to the natural stability of H_2O, hydrolysis is not a thermodynamically favourable process and requires the input of energy. Typically, water is split via electrolysis, using electrical energy to drive the reaction foreword.[21] If this electrical energy is generated from fossil fuel combustion, this process will be carbon intensive.[22] However, this splitting can be achieved using renewable solar energy, with light acting as the primary energy source to drive the decomposition of water in a photoelectrochemical (PEC) cell. Photocatalysis methods mimic natural photosynthesis in plants, with light being the energy source.[23] Here, the photons drive the reaction forward, converting electrical energy (e^-) to chemical energy (O_2/H_2), in a process called photoelectrolysis.[24,25] In a PEC cell, a material which facilitates the reaction is submerged in an electrolyte and exposed to light, expediting the OER, HER, or more rarely, both. Photoelectrolysis of water is difficult to achieve and is yet to be considered a commercially viable solution to fossil fuels, yet the highlighted benefits above are what drive additional research in this area.[26]

Poor reaction kinetics and thermodynamic requirements plague this process and there are many energy barriers to overcome to progress this technology.[26] One way to improve the issues facing PEC reactions is by altering the chemical structure of the light active component in the cell: the photoanode or photocathode.[27] These structures form the main components of the PEC cell and are the location and driving force of the OER and HER, respectively. In advancing our scientific knowledge and design processes for photoelectrode production, the possibilities involving PEC technology increase, bringing sustainable hydrogen energy closer to a mainstream reality.

1.3 Research Overview

The initial goals of this project were to use a thin film technology, atomic layer deposition (ALD), to create a new and novel way to modify photoanodes for photoelectrochemistry. Early research indicated that one of the most effective ways to improve the efficiency of many common photoactive compounds is the use of nanostructuring; that is, to produce the compound in a way that controls the structure down to the nanometre[28,29] Since ALD allows the material to be built atomic layer by atomic layer, this was the ideal technique for such an endeavor.

Transition metal compounds that exhibit semi-conductor behaviour are the typical candidates for use in PEC setups, as they facilitate the movement of electrons in a controlled manner. Hematite, Fe_2O_3, is a semi-conducting metal oxide that is abundant, stable and non-toxic, yet is plagued by electronic issues.[30] Poor charge transport, hole diffusion length and conductivity increases recombination of carriers, severely limiting efficiency.[31] Previous attempts to create a high performing hematite photoanode have been met with some limited success, though hematite is lacking behind many of its semi-conducting competitors.[32] Photocurrent performance peaks around 3.5mA cm^{-2} for hematite, versus for 11.7mA cm^{-2} for ZnO/CdS based structures – though compared to hematite, these high performing metal oxide films often come with a greater stability or environmental concerns.[33,34] Nanostructured hematite is a promising avenue for exploration, with previous research indicating that thinner films offer many advantages over thicker alternatives.[35] However, many thin film deposition methods used to grow hematite have achieved less than optimal results. Slow processes and expensive reactants are a common blight; ALD processes may have dose times exceeding 30 seconds or utilise precursors such as $Fe(thd)_3$, limiting commercial viability [36,37] Hence, this research project aimed to address these issues by utilising plasma enhanced ALD to manufacture hematite films that exhibit improved photoelectrochemical properties. ALD also allows for further structural alterations, including the addition of surface layers, interfacial layers between the semiconductor/substrate (“underlayers”) and dopant layers throughout. The composition, placement and thickness of these layers can be tuned to offer improved electrochemical properties. This project assesses various metal oxide dopants in this role and explores how altering these layers affects the properties of the photoanode.

1.4 Key Questions

There are three main questions this thesis aims to address, which arose from a combination of early research and experimental observation. In doing so it is hoped that multiple new insights will be offered towards the scientific field in question. These questions can be broken down into the following:

- What role does annealing temperature play with respect to composition and properties? Do these observations line-up with our current knowledge of substrate annealing steps?
- How does the use of underlayers affect the photoelectrochemical properties and what is the mechanism behind this?
- Do layer/gradient doping techniques yield any additional benefit to the photo-active films and if so, is there a clear rational behind this?

These recurring themes will be woven into chapters of this thesis and referenced at multiple points.

References

1 H. Ritchie, M. Roser and P. Rosado, *Our world data.*

2 M. M. Maja and S. F. Ayano, *Earth Syst. Environ.*, 2021, **5**, 271–283.

3 K. Gillingham and J. H. Stock, *J. Econ. Perspect.*, 2018, **32**, 53–72.

4 P. Ceppi and P. Nowack, *Proc. Natl. Acad. Sci.*, 2021, **118**, e2026290118.

5 S. I. Zandalinas, F. B. Fritschi and R. Mittler, *Trends Plant Sci.*, 2021, **26**, 588–599.

6 B. Wu and Z. Li, *Int. J. Climatol.*, 2022, **42**, 1818–1827.

7 T. Herzog, *World Resour. Inst.*, 2009, **7**, 2009.

8 F. Yang, Z. Wei and L. Long, *Mar. Freshw. Res.*

9 IRENA, *Hydrogen: A Renewable Energy Perspective*, 2019.

10 A. A. Alola, S. Saint Akadiri and O. Usman, *Sustain. Dev.*, 2021, **29**, 388–397.

11 J. Davison, R. A. Rose, N. J. Farren, R. L. Wagner, T. P. Murrells and D. C. Carslaw, *Environ. Sci. Technol.*, 2021, **55**, 4452–4461.

12 J. Hoelzen, D. Silberhorn, T. Zill, B. Bensmann and R. Hanke-Rauschenbach, *Int. J. Hydrogen Energy.*

13 A. Midilli, H. Kucuk, M. E. Topal, U. Akbulut and I. Dincer, *Int. J. Hydrogen Energy*, 2021, **46**, 25385–25412.

14 E. Shoko, B. McLellan, A. L. Dicks and J. C. D. Da Costa, *Int. J. Coal Geol.*, 2006, **65**, 213–222.

15 D. Gray and G. Tomlinson, *Mitretek Tech. Pap. MTR*, 2002, **31**, 2002.

16 P. Burmistrz, T. Chmielniak, L. Czepirski and M. Gazda-Grzywacz, *J. Clean. Prod.*, 2016, **139**, 858–865.

17 J. Tollefson, *Nature*, 2010, **464**, 1262–1264.

18 E. L. Miller, *Energy Environ. Sci.*, 2015, **8**, 2809–2810.

19 M. D. Bhatt and J. S. Lee, *J. Mater. Chem. A*, 2015, **3**, 10632–10659.

20 M. Walter, E. Warren, J. Mckone, S. Boettcher, Q. Mi, E. A Santori and N. S Lewis, *Solar Water Splitting Cells*, 2010, vol. 110.

21 S. Shen, *J. Mater. Res.*, 2014, **29**, 29–46.

22 S. Sadeghi and H. Vahidi, *Environ. Energy Econ. Res.*, 2020, **4**, 83–96.

23 F. E. Osterloh, *ACS Energy Lett.*, 2017, **2**, 445–453.

24 L. J. Minggu, W. R. W. Daud and M. B. Kassim, *Int. J. Hydrogen Energy*, 2010, **35**, 5233–5244.

25 Z. Chen, H. N. Dinh and E. Miller, *Photoelectrochemical water splitting*, Springer, 2013, vol. 344.

26 F. E. Osterloh and B. A. Parkinson, *MRS Bull.*, 2011, **36**, 17–22.

27 C. Jiang, S. J. A. Moniz, A. Wang, T. Zhang and J. Tang, *Chem. Soc. Rev.*, 2017, **46**, 4645–4660.

28 Y. Lin, G. Yuan, R. Liu, S. Zhou, S. W. Sheehan and D. Wang, *Chem. Phys. Lett.*, 2011, **507**, 209–215.

29 G. Wang, Y. Ling, H. Wang, L. Xihong and Y. Li, *J. Photochem. Photobiol. C Photochem. Rev.*, 2014, **19**, 35–51.

30 Y. W. Phuan, W.-J. Ong, M. N. Chong and J. D. Ocon, *J. Photochem. Photobiol. C*

Photochem. Rev., 2017, **33**, 54–82.

31 D. Zhou and K. Fan, *Chinese J. Catal.*, 2021, **42**, 904–919.

32 K. Sivula, F. Le Formal and M. Grätzel, *ChemSusChem*, 2011, **4**, 432–449.

33 R. Wang, L. Wang, Y. Zhou and Z. Zou, *Appl. Catal. B Environ.*, 2019, **255**, 117738.

34 J.-W. Jang, C. Du, Y. Ye, Y. Lin, X. Yao, J. Thorne, E. Liu, G. McMahon, J. Zhu, A. Javey, J. Guo and D. Wang, *Nat. Commun.*, 2015, **6**, 7447.

35 A. G. Tamirat, J. Rick, A. A. Dubale, W.-N. Su and B.-J. Hwang, *Nanoscale Horizons*, 2016, **1**, 243–267.

36 B. M. Klahr, A. B. F. Martinson and T. W. Hamann, *Langmuir*, 2011, **27**, 461–468.

37 M. Lie, H. Fjellvåg and A. Kjekshus, *Thin Solid Films*, 2005, **488**, 74–81.

Chapter 2: Photoassisted water-splitting: α-Fe_2O_3 Photoanodes

2.1 Introduction

This chapter is intended to inform on the over-arching issues surrounding the topic at hand, considering the multi-disciplinary nature of the project. The first section of this chapter will cover existing knowledge on electrochemistry and semi-conductor photoanodes, ensuring that readers from both an engineering or chemistry background are familiar the terminology and concepts mentioned throughout this thesis.

The second section will focus more closely on the literature surrounding hematite, specifically addressing known problems with hematite photoanodes and related ALD processes. By the end of this chapter, it is anticipated that the reader will be fully aware of the issues facing this project from the start. In doing so, the thought process throughout the PhD and this thesis should become clear.

2.2 Water-splitting for Hydrogen Production

2.2.1 Green hydrogen

As touched upon previously, hydrogen is considered a green fuel source, yet is often produced in a carbon intensive manner. The method of hydrogen production is important in determining the carbon footprint of hydrogen fuel, similar to how electricity can be green if produced by renewables, or carbon intensive if derived from fossil fuel combustion.[1] 'Blue' and 'grey' hydrogen originate from fossil fuel sources, though blue hydrogen includes carbon capture to reduce emissions, whereas green hydrogen is produce via either renewable feedstock or with renewable energy.[2] However, this wide description for green hydrogen often leads to confusion when characterizing hydrogen as 'green', since the definition can vary wildly per source.[3] Additionally, international standards vary on what define green hydrogen, including hydrogen that originates from fossil fuels but is extracted fully or partially with renewable energy, and hydrogen produced from the hydrolysis of water that uses grid electricity.[4] Add to this further discussion on whether photoassisted water-splitting is 'green' when using toxic photoanodes/cathodes and it is clear there is a high degree of scrutiny for 'green' hydrogen production technologies.[5] Thus, non-toxic, sustainable, renewable energy systems that can produce hydrogen are the goal to aim for in this field of study, though these systems face other issues, as assessed in this chapter.

2.2.2 Water Oxidation – The Challenges

Water splitting is an endothermic process, with an energy requirement of $\Delta G = 237.2$ kJ mol-1 under standard conditions.[6] At 298K, according to the Nernst equation:

$$E = E^0 - \frac{0.0592\ V}{n} log_{10} Q$$

Where n is the number of electrons transferred in the reaction, Q is the ratio of products over reactants and $\Delta G = nFE$, for water splitting this corresponds to E^0 of 1.23V per electron transferred.[7] The overall reaction for water splitting can be defined as:

$$H_2O_{(l)} \rightarrow \frac{1}{2}O_{2\,(g)} + H_{2\,(g)} \quad (1) \quad E^0 = 1.23\ V_{RHE}$$

With the oxygen evolution reaction (OER) the rate limiting step and the hydrogen evolution reaction (HER) energetically favourable[8]:

$$2H_2O_{(l)} \rightarrow O_{2\,(g)} + 4H^+_{(aq)} + 4e^- \quad (2) \quad E^0 = 1.23\ V_{RHE}$$

$$2H^+_{(aq)} + 2e^- \rightarrow H_{2\,(g)} \quad (3) \quad E^0 = 0.00\ V_{RHE}$$

Hence, to satisfy the thermodynamic requirements an applied voltage of at least $1.23V_{RHE}$ is needed.[9,10] As with any nonideal process, thermodynamic losses occur and a large overpotential is needed. The overpotential is defined as the difference between the thermodynamically-determined reduction potential, and the potential where the event is experimentally observed.[11,12] For electrolytic cells, these overpotentials indicate more energy is required to drive the reaction forward, and are a result of the high number of ions and electrons involved.[13,14]

The water-splitting process is also highly pH dependent, with the reaction in alkaline solution differing from that in neutral or acidic media. Alkaline electrolytes are often used due to their high ion content and increased conductivity, with NaOH and KOH common electrolytes in water-splitting cells.[15–17] At pH=14 OH^- ions dictate the OER [Eq.4].[18]

$$4OH^-_{(aq)} \rightarrow 2H_2O_{(l)} + O_{2(g)} + 4e^- \quad (4)$$

The half-cell potential for Eq.1 is 0.404V and, though this reaction is kinetically favourable, the multistep nature of the process adds additional energy hurdles at every step.[19] The consensus is that this occurs in a four-step process, where * represents an active surface site:

$$H_2O + * \rightarrow HO^* + H^+ + e^- \quad (5)$$

$$HO^* \rightarrow O^* + H^+ + e^- \quad (6)$$

$$H_2O + O^* \rightarrow HOO^* + H^+ + e^- \quad (7)$$

$$HOO^* \rightarrow * + O_2 + H^+ + e^- \quad (8)$$

Losses may occur at multiple points throughout the process.[20] For most common photoanodes that are made from semiconductors, the photons must possess the correct energy to promote an electron from the valence band (V_B) to the conduction band (C_B), leaving a hole (*) in its wake.[21] This is known as carrier generation [Figure 1].[22]

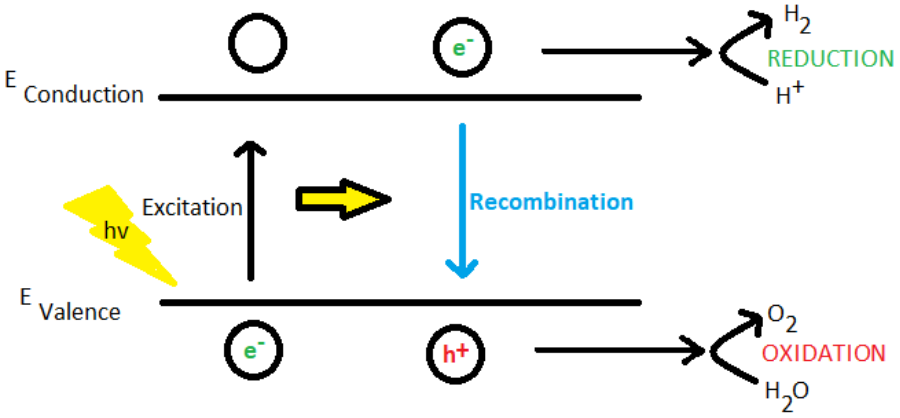

Figure 1: The basic water-splitting process via a semi-conducting material is outlined above. A photon (hv) initiates the process by electron excitation, promoting an electron from the valence to the conduction band and leaving a hole in its wake. This electron can either react to reduce hydrogen ions or recombine with the hole to stop any further reactions.

The electron should then be able to travel through both the substrate and the circuit to the cathode, where it will reduce hydrogen ions (H^+).[23] The hole must also be labile to facilitate the oxidation of water. Every aspect of the circuit must allow the progression of the reaction and movement of reactive species and ions.[24]

2.2.3 Recombination and Trap States

Recombination is a giant hurdle for this kind of process. In semiconductors it is not uncommon for an electron generated to recombine with a hole, thus preventing further reaction: carrier recombination.[25] There are multiple ways this can happen, however only three happen at any significant level in indirect bandgap semiconductors: band-band, trap-assisted and auger recombination [Figure 2].[26]

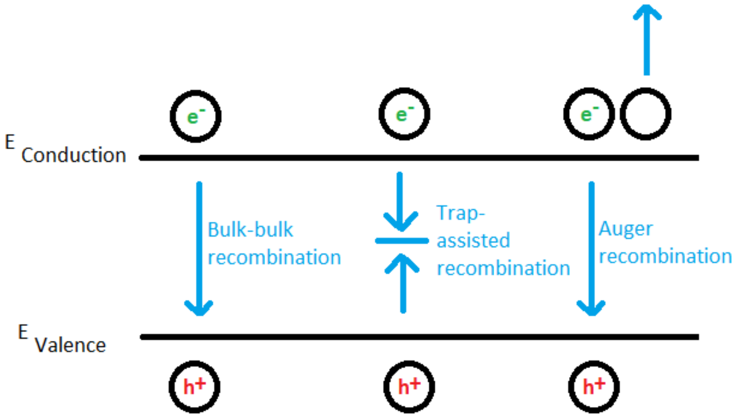

Figure 2: The way in which recombination can occur varies, as shown here. Band-band, also known as bulk-bulk, is a common form, with trap-assisted and auger recombination undergoing a more complex process.

2.2.3.1 Types of Recombination

Band-band recombination results from an electron spontaneously jumping down from the conduction band in a radiative manner, releasing a photon as it goes.[27] This is typically a function of e^-/h^+ density, with higher levels of band-band recombination occurring as the number of electrons and holes increases.[28] Auger is similar in that the recombination event results in an electron dropping down in energy to combine with a hole, however the energy instead passes to a third carrier, typically another electron in the conduction band.[29] This then thermalises down and relaxes back to the edge of the band. As this is a multi-step process that depends on the ability of the charge carriers to exchange energy, this form increases as a function of charge carrier density, i.e. this is more likely to occur in heavily doped semiconductors.[30,31] Trap-assisted or Shockley-Read-Hall recombination differs in that it is a non-radiative process that is a very real issue in semiconductor photoanodes possessing an indirect bandgap.[29] Here, defects in the material create an energy level in a forbidden region of the bandgap in which electrons can get 'trapped'. Normally a result of foreign atoms in the lattice or structural defects, the electron can either jump up to the conduction band or drop back down, in a two-step process. [32,33]

An amalgamation of factors form the overall recombination rate for a material. Thus, it is nigh impossible to 'fix' this problem in its entirety, though it is possible to target certain known causes of recombination.[34] In looking to semiconductors, some of these solutions offer marginal improvements in recombination properties.

2.3 Semiconductors: Role in Photocatalysis

2.3.1 Semiconductor Properties

Semiconductors are materials that fall between insulators and metals in terms of properties and band structure. Similar to insulators, semiconductors have a gap between their valence and conduction bands, but unlike insulators this gap (called the bandgap) is small enough to allow energised electrons to jump to the conduction band (Figure 3).[35] The fermi level, the highest energy point an e^- can occupy at 0K, lies close to the middle of this bandgap for pure semiconductors. In conducting metals, these bands overlap and allow the continuous flow of charge. For semiconductors, the gap can fall between 0eV and 5eV, though the wider the gap, the more energy it will take to allow the excitation of an electron[36,37]

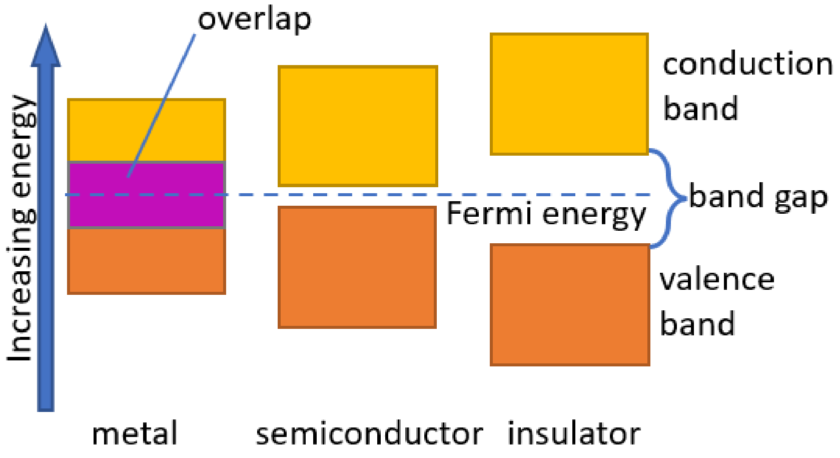

Figure 3: Schematic highlighting differences in bandgap across different material types. Recreated from reference.

However, for photolysis the bandgap must also be sufficient enough to maximise the absorption of light, with narrow bandgaps also unfavourable.[38] The optimum range for absorbing solar radiation is between 1.1 and 1.7 eV, anything below this will result in the photon energy mostly dissipating as heat and above this will suffer decreased absorption.[39,40] As semiconductors have a continuum of states in their conduction and valence bands, the absorption coefficient does not decrease with increased excitation energy.[41] This means that higher energy photons can be absorbed, allowing for semiconductors with bandgaps >1.7eV to still be feasible for this light absoption[39] When entropy losses and overpotentials for water-splitting are taken into account, the minimum bandgap sits nearer to 2eV.[42] As well as this, the position of the band edges is also important, with the valence band needing to exceed the OER ($1.23V_{RHE}$) and the conduction band having to sit below the HER ($0.00V_{RHE}$).[43,44] This further narrows down the list of viable semiconductors, with many of the remaining excluded based on their stability in alkaline media. Fortunately, the application of an external bias

2.3.2 Band structure

There are other factors relating to band structure and alignment to consider when exploring semiconductors as photoelectrodes. As mentioned, there is a gap between the valence and conduction band of semiconductors. However, the structure of this gap may vary across different semiconductors, with the maximum and minimum energy states aligned in momentum for some or misaligned in others. When the electrons in these states are aligned in momentum, this is referred to as a direct bandgap, with the opposite known as an indirect bandgap (Figure 4).[45–47]

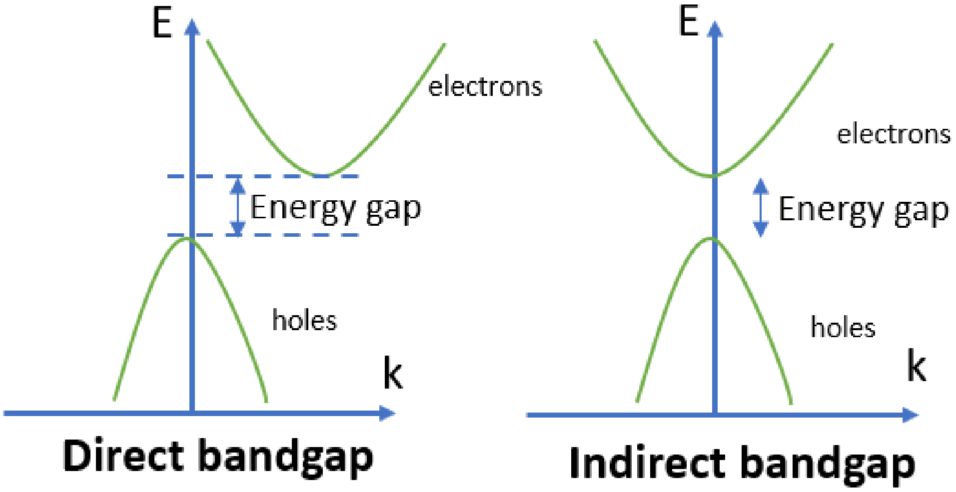

Figure 4: Energy structure of direct and indirect bandgap semiconductors. Adapted from reference.[48]

Photons possess very small amounts of energy and as highlighted earlier, a photon with enough energy can excite an electron to the conduction band, leaving a hole in its wake. For direct bandgap semiconductors this process occurs easily as the electrons are already aligned in momentum.[49] Whereas in indirect bandgap semiconductors this process requires a change in energy and momentum, thus this transition requires interactions with lattice vibrations (phonons) and occurs much slower as a result.[45,50] Hence for the carrier generation process direct bandgaps are favourable. However, the same principles apply for the reverse of this process, with radiative recombination occurring easily in direct bandgaps compared to indirect. For indirect bandgaps, recombination is typically non-radiative, occurring at point defects and grain boundaries.[51,52] Light absorption for indirect bandgaps is also a consideration, with light able to pass further into the semiconductor before being absorbed. This is beneficial for thicker films but may mean light passes through thinner films, and hence is a consideration for photoelectrode design for light harvesting purposes.[53,54]

2.3.3 Band-bending

When there is contact between a semi-conductor and a dissimilar material such as an electrolyte, a potential difference forms at the interface, effectively creating a heterojunction between the electrode/electrolyte.[55] This results from semiconductors having lower conductivity than the electrolytes, creating a drop in potential in the boundary layer of the electrode, with little change in the electrolyte. Charge carrier transfer occurs until an equilibrium is reached and the potential difference has dissipated.[56,57] This is achieved by bending of the conduction and valence bends to reduce the potential, with the synergistic movement of charge carriers. If the potential difference is positive electrons will be moved to the surface (an accumulation layer), or if the difference is negative electrons will move from the surface (a depletion layer).[58,59] This is reflected with the band bending, which moves upwards towards the surface at positive potential and bends downwards towards the bulk when negative.

The potential at which the equilibrium is established is known as the flat-band potential.[60]

A consequence of these effects is that the fermi level at the semiconductor surface differs from that of the bulk in typical PEC setups and the high density of charge carriers at the surface creates new electronic surface states.[61] This can lead to fermi level pinning that ultimately hampers performance.[62] Fortunately, the application of external bias in PEC cells helps to preserve the band bending in the semiconductor. The applied electric field also maintains the charge separation layer, which allows for the separation of photogenerated charges in photoelectrodes. This separation facilitates the sweeping of electrons from the surface into the bulk, reducing recombination rates.[63–65]

2.3.4 Doped Semiconductors

The properties of semiconductors can also be tuned by doping with additional elements. Depending on the element added, a semiconductor can either be doped with additional electrons or additional holes. When electron donating elements are added, this is known as n-type doping (n = negative), with electron acceptors being p-type (positive).[66,67] For n-type semiconductors, the fermi level lies closer to the conduction band, whereas for p-type the fermi level is shifted towards the valence band.[68] Undoped semiconductors are referred to as intrinsic semiconductors, with p/n-doped known as extrinsic. Intrinsic semiconductors tend to have lower electrical conductivity than their extrinsic counterparts, as doping increases the number of charge carriers.[69] N-type semiconductors are often favoured in photovoltaic applications due to this increased electron presence and tend to exhibit band bending towards the surface as a result of this accumulation. Hence, n-type semiconductors are often used as photoanodes (where oxidation occurs), whereas p-type semiconductors function well as photocathodes.[70]

2.3.5 Common Metal Oxide Photoanodes

As indicated, there are a couple of qualities a semiconductor should possess in order to considered ideal for water splitting, these are: [11]

- Possesses a suitable band-gap – Ideally spans the redox potentials for water and band-gap must also exceed 1.23V to make the process thermodynamically favourable, yet not be so large that the energy requirements for electron excitation will be too great.[34]
- Good charge transport properties.
- High stability in pH 14 alkaline solution – Degradation over time would mean that the electrodes would need replacing frequently. This isn't economically desirable.
- Low toxicity, where possible.

There are a number of potential semiconductors that meet most, if not all of these criteria. This can be seen in Figure 5.

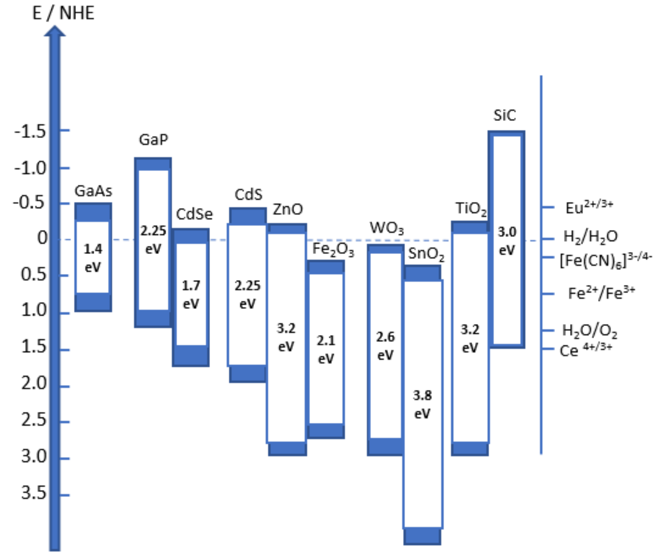

Figure 5: This graphic shows the relative band-edge positions and bandgaps for the most researched semi-conductors in this field, as compared to the HER and OER potentials. [71]

For a material to successfully drive the redox reaction forward, the C_B edge must be more negative than the HER and more positive than the OER for H^+ to be sufficiently reduced. However, it is uncommon for a material to favourably drive this multi-step reaction independently. It is common to focus on improving a material to benefit either the OER, or the HER, with the idea that a good photoanode can pair with a good photocathode to create an overall efficient system, known as a tandem cell.[72]

The most commonly researched semiconductors for photoassisted water-splitting were highlighted in Figure 5. The properties of these semiconductors for this purpose can be summarized as the following:

Gallium based: GaAs/GaP

Gallium arsenide (GaAs) has an incredibly favourable bandgap of 1.4eV for this process, but its stability in solution is incredibly poor, with the electrodes degrading within an hour of use.[73] Coating GaAs appears to be the main strategy for addressing this, with a TiO_2/Ni layer exhibiting an impressive maximum photocurrent of 15mA cm^{-2}.[74] On the other hand, gallium phosphide (GaP) exhibits good long-term stability, but has poor charge transport properties.[75] The main drawback of using gallium based photoelectrodes is cost, with toxicity issues also a factor for GaAs compounds.[76]

Cadmium based: CdSe/CdS

Cadmium Selenide and cadmium sulfide (CdSe/CdS) have favourable bandgaps for water-splitting and are most commonly used in the form of quantum dots, known as quantum dot solar cells (QDSCs).[77] In this capacity, photocurrents of 12.6mA cm^{-2} have been recorded, highlighting the potential for these cells.[78] However, as with GaAs, toxicity is a large drawback to cadmium-based semiconductors.[79]

Zinc oxide: ZnO

Zinc oxide has the advantage of being a low cost, low toxicity semiconductor, but has a larger than ideal bandgap of 3.2eV. On its own, ZnO suffers from high recombination rates and poor photoelectrochemical performance, however when coupled with other semiconductors this can be improved.[80,81] Photocurrents over 10mA cm^{-2} have been reported in this instance, though these high performing samples incorporated cadmium-based semiconductors.[82]

Tin Oxide (SnO_2)

Due to its wider bandgap of 3.8eV, tin oxide finds more frequent use as a dopant to other metals than as a bulk component for solar applications.[83] SnO_2 is widely used as a transparent conductive glass coating when doped with elements such as fluorine and indium (FTO/ITO).[84]

Tungsten oxide: WO_3

Tungsten oxide has a bandgap of ~2.6eVand improved charge transfer properties compared to other semiconductors such as ZnO and TiO_2, though still suffers from high recombination rates and poor surface chemistry.[85] Photocurrents for WO_3 are slightly diminished from the previous examples, with peak performance ~6mA cm^{-2}.[86,87] An additional drawback to tungsten-based semiconductors is the high cost compared to other cheap semiconductors.[88]

Titanium dioxide: TiO_2

Titanium dioxide also possesses a larger bandgap of 3.2eV, but is cheap, non-toxic and stable in solution. Unfortunately, TiO_2 has lower electron mobility than ZnO, which is a comparable semiconductor in most aspects.[89] However, TiO_2 finds common use as a dopant or additive layer to many other semiconductors, highlighting its value for this purpose.[90]

Silicon carbide: SiC

Silicon carbide is a stable compound, with a typical bandgap of 3.02eV for the most common polytype and band edges that satisfy both the OER and HER.[91] As n-type SiC suffers from photocorrosion, it is mostly commonly p-doped and used as a photocathode.[92] In this role, a photocurrent of -5.3mA cm^{-2} was achieved when paired with a palladium cocatalyst.[93]

2.3.6 Hematite

The remaining semiconductor to assess is hematite. Hematite is one of the many forms of the compound iron oxide, with the chemical formula α-Fe_2O_3. Due its stable nature, it is a common iron ore found within the earth.[94] Though it exhibits extremely mild magnetism, it is not considered a magnetic compound, differing from magnetite and other forms of iron oxide.[95] There are multiple known polymorphs of Fe_2O_3. Hematite is one form, with the specific notation α-Fe_2O_3. Other polymorphs include γ-Fe_2O_3 (maghemite) and β-Fe_2O_3, though only the α and γ forms occur naturally.[96]

Hematite belongs to the rhombohedral lattice system, as part of the hexagonal crystal family, along with other compounds such as corundum (α-Al_2O_3). Here, the Fe^{3+} ions are octahedrally coordinated and sandwiched between layers of oxygen in a hexagonal close-packed structure.[97,98]

It is a naturally conductive n-type metal oxide, with a band-gap in the order of 1.9-2.2eV and C_B/V_B edges that sit favourably in the range of the OER. These properties result in a maximum theoretical output of 12.6mA/cm^2 at 1.23V vs the reversible hydrogen electrode (RHE) and a theoretical solar to hydrogen (STH) conversion efficiency of 15.3%.[59]

Though its electrical properties are desirable for a photoanode, its theoretical capabilities currently far exceed its actual performance in a PEC cell. Due to inherent electronic flaws hematite is limited in its water splitting capabilities. These flaws include: having high surface levels of recombination, possessing poor charge carrier kinetics, low electrical conductivity and low carrier lifetimes and electron mobility.[99]

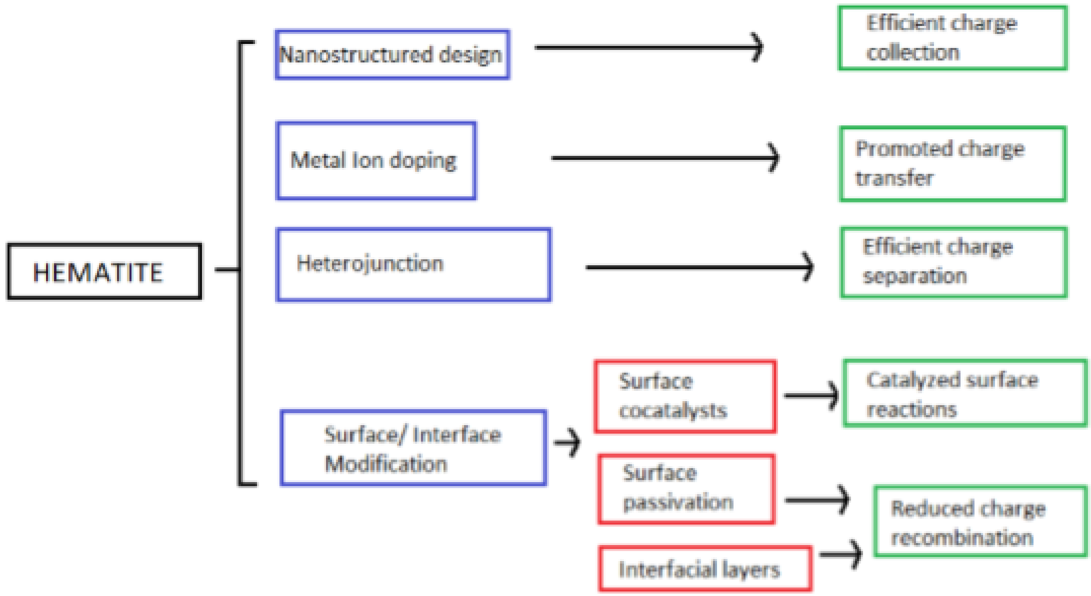

Figure 6: This figure depicts common ways of overcoming the limitations of hematite-based photoanodes. The red and blue boxes show the adaptations that can be added to the structures, with the green box highlighting the method of action, based on prior research. Recreated from Zhang et al., Doping-Promoted Solar Water Oxidation on Hematite Photoanodes, 2016.[100]

Many methods have been explored to reduce these issues (Figure 6). This project utilises multiple of these adaptations in an effort to create an improved hematite photoanode, though some relevant forms will be explored a little further here.

2.4 Photoanode Modifications

2.4.1 Elemental Doping

Elemental doping involves introducing foreign atoms into the hematite lattice and is achieved in a variety of ways. Quite commonly, hematite is produced using a one-pot synthesis known as the hydrothermal method. Hydrolysis of iron chloride occurs under acidic conditions, with Fe_2O_3 precipitating with heat exposure.[101] As established previously, semiconductors can be n- or p-doped depending on the element added, with both metals and non-metals used for this purpose. A variety of elements have been tested as dopants in hematite, with each acting in various ways on the hematite semiconductor.

DFT and computational methods have characterised the interactions of elements such as Co, Ni, Cu, and Zn with Fe_2O_3, surmising that first row transition elements lower the LUMO of hematite in such a way that it behaves like a p-type conductor.[102] This is due to the high spin nature of the metals, which add electrons to half-filled 3d dopant-centered orbitals. When focusing on nickel, the t_{2g} orbitals are in a high energy state as they are 5/6 filled. This results in a low energy empty LUMO state which lowers the HOMO-LUMO gap energy.[103] This theory is corroborated with other works, which show the band gap reducing effect of doping these cations into metal frameworks.[104–107] Nickel doping in particular has proved effective for hematite, with improved charge separation and band bending resulting in a 10-fold enhancement in photocurrent.[108] However the method of action for zinc is different, as the Zn^{2+} d orbitals are filled with only two electrons provided to the O 2p band. A hole is therefore produced, as a Zn^{2+} replaces the 3 electron Fe^{3+} species. This phenomenon has been explored in other studies, which suggest that zinc ions will replace ions of similar size in a lattice, causing local defects but increasing carrier mobility.[109,110] This presents as a photocurrent increase of ~0.3mA cm^{-2} for $Zn\text{-}Fe_2O_3$ compared to pristine hematite, as well as a cathodically shifted onset potential.[111]

Other elements such as titanium have been explored heavily as a hematite dopant. For Ti^{4+}, the excess electrons are donated to nearby Fe centres, increasing conductivity via n-doping. The smaller Ti^{4+} ions replace Fe^{3+} in the crystal lattice, improving donor density and charge transport.[112–114] For thin film hematite samples this has resulted in a peak photocurrent close to 4mAcm^{-2}, compared to ~1mA cm^{-2} at 1.5V$_{RHE}$.[115] Zirconium, tungsten, rhodium and ruthenium have all showed to improve the optical properties of hematite, whereas iridium and molybdenum doping had the opposite effect.[87,116–119] P-block elements Al, Ga, In, and Tl with a 3+ oxidation state have little effect on the bandgap properties of hematite, but offer a degree of improvement in photo response, commonly due to increased charge carrier concentration and conduction.[120–126]

Tin, one of the most utilised dopants in hematite, has been shown to improve the efficiency of hematite in multiple different arrangements. The band edges of SnO_2 are similar to hematite, with a valence band and conduction band of ~ -8eV and ~ -4eV respectively, compared to -7eV and -4.8eV for Fe_2O_3. Having a similarly aligned band gap is beneficial for preventing charge transfer between ions, with particular benefits for overlayers.[127] Overall tin doping is shown to improve the transfer of surface holes to the electrolyte and partially lower onset potentials, creating a general enhancement in efficiency.[128] One partial explanation here is that tin oxide possesses a high conduction band energy, so it has been theorised that it may provide the best electrical contact to n-type conductors like hematite. This is only held to be true however if strong interfacial dipoles and/or Fermi level pinning are not present.[129]

Overall, the HOMO-LUMO gap and the bandgap in hematite can be affected by the addition of dopant elements, which occurs due to a breaking in the symmetry around the iron centre. The altering of the band gap adjusts the wavelength of light that is absorbed for the hematite species, which can be identified with techniques such as UV-Vis spectroscopy.[130] On the whole, doping as a strategy offers benefits by increasing charge carrier densities which improve conductivity, though each doping element interacts with hematite in a different way.

2.4.2 Underlayers

Previous research has established there is an unfavourable nature to the hematite/FTO interface, due to a severe mismatch in the material lattices.[131] When adding hematite to FTO glass, a so-called 'dead layer' is known to form, in which the crystallinity of the hematite is poor and an increased number of trap states exist.[132] Electron movement through this interface is required as part of the PEC cell circuit. Hence, targeted alterations to this region result in improved photocurrent responses and reduced recombination rates.[133] A homogenous interface can prevent back diffusion of electrons from the FTO to the hematite, thus increasing photocurrent. [134] However, due to the possibility of introducing contamination between the interfacial layer and the hematite, research in this area is reduced when compared to modifications such as overlayers.

Previous studies have looked in to different underlayers for hematite, including SnO_2,[135] TiO_2 and Nb_2O_5,[136] Ga_2O_3,[137] SiO_2,[138] FeOOH,[101] WO_3[132] and ZrO_2[139]. Adding an underlayer without introducing contamination is difficult for films produced hydrothermally, but possible when thin film deposition techniques such as ALD are used.[140] Due to poor growth rates ALD is not commonly employed to produce the hematite layer, but the consensus remains that an underlayer often improves electron transport properties.[98] The agreed mechanism of action seems to vary, as some metal oxide layers offer a degree of doping via increased carrier concentrations.[131] However, this seems to be more prominent for ultrathin (>20nm) films, as morphological effects are more pronounced and doping lowered for thicker samples.[137] Another explanation is that the thinner 'dead layer' results in stronger band bending effects, which lead to improved charge separation in the space charge layer.[134] Unexpectedly, an additional underlayer effect is lowered surface recombination rates for these samples. Here it is theorised that the faster electron movement through the sample also reduces the chance of a recombination event at the surface.[132]

When comparing interfacial layers overall, thinner layers seemed to be more effective than thicker ones. Using heat to drive Sn doping from FTO glass is commonplace and hence thinner layers allow this movement of Sn to occur.[139] Though, some thinner layers allow conduction band alignment with that of hematite, facilitating the electron movement.[141] Hence, compounds with large C_B discrepancies that require increased degrees of electron tunnelling, such as TiO_2, benefit from a thin underlayer.[136,142]

Overall, the research is indicative of a beneficial underlayer effect, with thin interfacial layers a good starting point to proceed from. One of the benefits of using ALD is the ability to vary the compositional layers of a material, with low levels of contamination. In this subject area it is known that these compositional variations can yield interesting and advantageous properties for the materials altered. Consequently, the opportunity was taken to study the effects firsthand.

2.4.3 Layer Doping

Gradient doping is a way of adding layers of dopant to a material in a controlled fashion.[143] Typically this is done by adding an underlayer and using heat to diffuse, but as the main material here (Fe_2O_3) was produced using ALD, it is possible to add layers of dopant in situ.[144] This has been achieved for other ALD experiments, so this is an exciting possibility to address a known hematite flaw.[145] Gradient doping in particular has been studied for other photoanodes such as $BiVO_4$, using methods such as spray pyrolysis to build layered concentrations of dopant into the structures.[146] In doing so, it is possible to create built in electric fields that facilitate the movement of charge carriers through the substrates.[147] Additionally, as the initial research established a possible self-limiting growth pattern for hematite ALD sequences, this could be an innovative way to address this problem and continuously reset the surface - encouraging growth throughout the ALD process.[98]

On the whole, dopants are widely employed to improve photoanode properties, and there is a plethora of well-researched candidates to choose from. For example, tin, one of the most utilised dopants in hematite, has been shown to improve the efficiency of hematite photoanodes, with both surface and gradient doping being used effectively.[148] An ideal doping candidate should possess high electronic conductivity, good visible transparency (in thin film form), and energy band alignment with the bulk substrate.[129] Other transition metal oxides typically pair well with hematite and the candidates chosen will be covered in later sections.

2.5 ALD of α-Fe_2O_3

2.5.1 Nanostructuring: A Solution?

An effective method found to address several electronic issues is nanostructuring. Many structures of hematite have been explored for use as a photoanode, including nanorods, nanowires, nanotubes, nanosheets, nanoparticles, nanospheres and nanocorals/flowers.[149–155] Typically, the reaction conditions and annealing temperature play a large part in the resulting structure created. It is already known that crystallite size and lattice properties determine a large degree of the photoactivity for a compound, with structure governing the mobility of the electrons – in forming electron hole pairs or travelling through to the conducting interfaces.[138,156] In changing the annealing temperature and the reaction conditions a degree of control can be exerted over the structure, with multiple benefits ensuing as a result. For instance, smaller sized nanoparticles were found to be able to hold on to charge carriers for longer amounts of time than their larger counterparts, thus diminishing recombination.[157] Moreover, variations in particle shape altered the absorption region for some compounds, with hollow nanoring species exhibiting increased absorption bands from 300-1000nm.[158] Similarly, nanotubes and nanoporous films have been shown to possess charge transport properties up to 50x higher than even nanoparticles.[159,160] These novel research methods illustrate the need for further research into this area, in the quest to overcome the electronic failings of materials such as hematite.

2.5.2 Atomic Layer Deposition (ALD) of Hematite

ALD is a proven method of nanoscale film production offering incredible advantages over its counterparts. Particularly, the ability to grow high aspect ratio thin films, layer by layer, allows for an extreme degree of design control not possible with conventional wet bench methods.[161] However, ALD of hematite is uncommon compared to other metal oxides due to its low growth rate, constricted temperature windows and low reactivity precursors.[98] In this project, plasma enhanced ALD

(PEALD) is utilised to bolster the growth rate and create a favourable ALD process. Previous literature exploring similar ALD processes formed the foundation of the work, with a notoriously poor growing precursor, ferrocene ($Fe(Cp)_2$), the target of this research. Ferrocene is cheap and stable, thus an ideal industrial candidate.[162] This is a requirement should this form of hydrogen production be scaled up for commercial use.

ALD of hematite is not a new concept, yet there are few detailed studies on the topic. Along with $Fe(Cp)_2$, other precursor examples include $Fe(thd)_3$ and $Fe_2(O^tBu)_6$ – none with results that would make the procedure commercially viable.[98,163–166] Coreactants often include H_2O, O_2 and O_3, each with varying definitions of 'success'. Oftentimes processes require growth temperatures >300°C, which in itself restricts the number of possible substrates for depostion.[167,168] When $Fe(Cp)_2$ studies are viewed in isolation, a few trends are observable.

Firstly, it was noted that an average chamber temperature of around 250°C generated lower levels of carbon impurity, had the optimal growth rate and produced a more crystalline product, when compared to both higher and lower values.[169–171] Coreactants were of importance in respect to film structure/composition, with alterations to type and exposure time resulting in changes to the composition of the iron oxides made. Some examples are the need for high doses of O_3 to shift film composition in favour of hematite, H_2O usage resulting in a mixture of Fe_3O_4/Fe_2O_3 and O_2 gas coreactants requiring high temperatures to yield a final hematite product.[172–175] Furthermore, to overcome the low vapour pressure ferrocene possesses, typical exposure/ precursor dose times often exceeded 20s, ranging as high as 200s; this is impractical for film growth over 100nm.[176] However, Li et al. employed a heated vapour push bubbler in their setup, shortening the pulse sequence to 10s-20s-10s-20s for precursor dose and purges.[177] Literature in this area was light, though using these observations as a starting point, a plasma enhanced ALD process for making hematite was created.

2.6 Historic Electrochemical Hematite Performance

Comparing the peak onset and maximum photocurrents obtained for different photoanodes is often difficult due to variations in the structure, conditions and measurement techniques used to assess performance. Any number of parameters can be varied between research groups, which makes for non-equivalent numerical comparisons. Some attempts to standardise conditions have been made, such as using the Reversible Hydrogen Electrode (RHE) as the quoted reference electrode in literature, which removes variations between commonly used reference electrodes.[178] However, it is still difficult to make side by side comparisons of photoanodes as composition, structure and substrate can also vary widely. As a result, this subsection will highlight high performing hematite films that are relevant to this project, while also indicating key differences that make direct comparisons between studies difficult.

Firstly, impressive photocurrents have been achieved across a wide array of hematite morphologies. One study used a cold spray deposition technique to produce Fe_2O_3 nanoparticles on ITO glass.[179] These nanoparticles exhibited a photocurrent of 1.3 mA cm^{-2} in 1M KOH (at $0.7V_{Ag/AgCl}$), which increased to 4.25 mA cm^{-2} in 1M NaOH when coated with ZnO and TiO_2 surface layers. Notably, 0.7 $V_{Ag/AgCl}$ is approximately $1.9V_{RHE}$ depending on conditions – far greater than the 1.23 V_{RHE} benchmark sought after in these reactions. Mesoporous films have been created using an SiO_2 scaffold that in 1M NaOH exhibits a photocurrent of ~1 mA cm^{-2} at 1.7 V_{RHE}.[180] This increased to ~3 mA cm^{-2} when Ti doping was incorporated. Furthermore, the inclusion of IrO_2 nanoparticles on Fe_2O_3 nanorods provided photocurrents of 3.2 mA cm^{-2} at 1.23 V_{RHE}, while CoPi surface layers on electrodeposited Fe_2O_3 had an impressive maximum of 2.75 mA cm^{-2} at 0.5 $V_{Ag/AgCl}$.[181,182] Notably, unaltered hydrothermally produced hematite on FTO often exhibits low photoactivity, with photocurrents in the range of 0.075 mA cm^{-2} at 0.7 VAg/AgCl not uncommon.[128] This highlights the benefit of structural and compositional modifications.

In looking to onset potential, the values achieved for other semiconductor materials are much lower than the lowest found for hematite. As an example, one study highlighted that CoFe Prussian blue analogues coupled with antimony-doped TiO_2 produced an onset potential of 0.05 V_{RHE}.[183]. Comparatively, the best onset potentials for minimally altered hematite photoanodes were found to hover around ~0.62 V_{RHE}.[184,185] Meanwhile hydrothermally produced, undoped hematite has a photo-onset far exceeding the 1.23 V_{RHE} goal – this was previously highlighted as the minimum applied voltage required to drive the OER.[59] On the lowest end of the scale, an etching/regrowth method achieved an onset of ~0.45 V_{RHE}.[186] In this study the Fe_2O_3 was partially destroyed in acidic media, with simultaneous addition of $NiFeO_x$ in the regrowth phase to further improve the structure. Another study accomplished an onset potential of 0.58 V_{RHE} for Fe_2O_3 produced by heating iron foil in a H_2-O_2 flame.[187] This highlights that even with large modifications to the hematite photoanodes, success has been limited when compared to other non-hematite based electrodes.

In looking to electrochemical performance, shifting the onset potential cathodically is impressive if achieved with minimal design interventions. Ideally, making improvements to both photocurrent and onset potential is the ultimate aim for this project, with the above benchmarks considered the peak performance currently achieved for hematite in this field of study.

2.7 Conclusions

To sum up, this section has covered the fundamentals of the electrochemistry used in this project and established the base literature which guided the research decisions later in this PhD. The key concepts behind photoassisted water splitting have been covered, along with the basics of semiconductor science which will be referenced in this work. The properties of common semiconductor photoelectrodes were summarized to highlight the benefits of hematite based photoanodes, along with typical methods of improving the poor electronic properties of hematite.

Further literature exploration will occur in the subsequent experimental chapters while investigating the data acquired. The next chapter will cover the experimental techniques used in this project prior to any further experimental discussion.

References

1 W. W. Clark II and J. Rifkin, *Energy Policy*, 2006, **34**, 2630–2639.

2 S. Atilhan, S. Park, M. M. El-Halwagi, M. Atilhan, M. Moore and R. B. Nielsen, *Curr. Opin. Chem. Eng.*, 2021, **31**, 100668.

3 A. M. Oliveira, R. R. Beswick and Y. Yan, *Curr. Opin. Chem. Eng.*, 2021, **33**, 100701.

4 A. Velazquez Abad and P. E. Dodds, *Energy Policy*, 2020, **138**, 111300.

5 A. A. Basheer and I. Ali, *Int. J. Hydrogen Energy*, 2019, **44**, 11564–11573.

6 M. Walter, E. Warren, J. Mckone, S. Boettcher, Q. Mi, E. A Santori and N. S Lewis, *Solar Water Splitting Cells*, 2010, vol. 110.

7 A.-S. Feiner and A. J. McEvoy, *J. Chem. Educ.*, 1994, **71**, 493.

8 I. Holmes-Gentle and K. Hellgardt, *Sci. Rep.*, 2018, **8**, 12807.

9 E. Ravera, G. Parigi and C. Luchinat, *J. Magn. Reson.*, 2017, **282**, 154–169.

10 T. Shinagawa and K. Takanabe, *ChemSusChem*, 2017, **10**, 1318–1336.

11 *Russ. J. Electrochem.*, 2002, **38**, 1364–1365.

12 S. Niu, S. Li, Y. Du, X. Han and P. Xu, *ACS Energy Lett.*, 2020, **5**, 1083–1087.

13 S. Wang, A. Lu and C.-J. Zhong, *Nano Converg.*, 2021, **8**, 4.

14 G. Renger, *Photosynth. Res.*, 2007, **92**, 407–425.

15 J. N. Hausmann, B. Traynor, R. J. Myers, M. Driess and P. W. Menezes, *ACS Energy Lett.*, 2021, **6**, 3567–3571.

16 N. K. Biswas, A. Srivastav, S. Saxena, A. Verma, R. Dutta, M. Srivastava, S. Upadhyay, V. R. Satsangi, R. Shrivastav and S. Dass, *RSC Adv.*, 2023, **13**, 4324–

4330.

17 J. H. Lim, J. Hou, J. Chun, R. D. Lee, J. Yun, J. Jung and C. H. Lee, *Membranes (Basel).*, , DOI:10.3390/membranes12060556.

18 Z.-Y. Yu, Y. Duan, X.-Y. Feng, X. Yu, M.-R. Gao, S.-H. Yu, Z. Yu, Y. Duan, X. Feng, X. Yu, M. Gao and S. Yu, , DOI:10.1002/adma.202007100.

19 M. I. Jamesh, *J. Power Sources*, 2016, **333**, 213–236.

20 R. van de Krol, Y. Liang and J. Schoonman, *J. Mater. Chem.*, 2008, **18**, 2311–2320.

21 C. Hu, L. Zhang and J. Gong, *Energy Environ. Sci.*, 2019, **12**, 2620–2645.

22 F. E. Osterloh and B. A. Parkinson, *MRS Bull.*, 2011, **36**, 17–22.

23 P. Millet, R. Ngameni, S. A. Grigoriev and V. N. Fateev, *Int. J. Hydrogen Energy*, 2011, **36**, 4156–4163.

24 P. Zhang, T. Wang and J. Gong, *Adv. Mater.*, 2015, **27**, 5328–5342.

25 S. Wheeler, F. Deledalle, N. Tokmoldin, T. Kirchartz, J. Nelson and J. R. Durrant, *Phys. Rev. Appl.*, 2015, **4**, 24020.

26 P. Cendula, A. Sancheti and P. Simon, *Adv. Theory Simulations*, 2021, **4**, 2100312.

27 T. Goudon, V. Miljanović and C. Schmeiser, *SIAM J. Appl. Math.*, 2007, **67**, 1183–1201.

28 F. Le Formal, S. R. Pendlebury, M. Cornuz, S. D. Tilley, M. Grätzel and J. R. Durrant, *J. Am. Chem. Soc.*, 2014, **136**, 2564–2574.

29 F. Olivier, A. Daami, C. Licitra and F. Templier, *Appl. Phys. Lett.*, 2017, **111**, 22104.

30 V. Sarritzu, N. Sestu, D. Marongiu, X. Chang, S. Masi, A. Rizzo, S. Colella, F.

Quochi, M. Saba and A. Mura, *Sci. Rep.*, 2017, **7**, 44629.

31 J. T. Graham, M. L. Crespillo, F. Agulló-López and W. J. Weber, *Acta Mater.*, 2022, **229**, 117829.

32 Z.-Y. Zhang, H.-Y. Wang, Y.-X. Zhang, Y.-W. Hao, C. Sun, Y. Zhang, B.-R. Gao, Q.-D. Chen and H.-B. Sun, *Sci. Rep.*, 2016, **6**, 1–7.

33 L. Li and E. A. Carter, *J. Am. Chem. Soc.*, 2019, **141**, 10451–10461.

34 Z. Zhou, J. Liu, R. Long, L. Li, L. Guo and O. V Prezhdo, *J. Am. Chem. Soc.*, 2017, **139**, 6707–6717.

35 C. Siu, in *Electronic Devices, Circuits, and Applications*, Springer, 2022, pp. 35–39.

36 K. Seeger, *Semiconductor physics*, Springer Science & Business Media, 2013.

37 C. Jiang, S. J. A. Moniz, A. Wang, T. Zhang and J. Tang, *Chem. Soc. Rev.*, 2017, **46**, 4645–4660.

38 B. J. Van Zeghbroeck, 2011.

39 N. S. Lewis, *Inorg. Chem.*, 2005, **44**, 6900–6911.

40 M. Valenti, M. P. Jonsson, G. Biskos, A. Schmidt-Ott and W. A. Smith, *J. Mater. Chem. A*, 2016, **4**, 17891–17912.

41 A. Fahrenbruch and R. Bube, *Fundamentals of solar cells: photovoltaic solar energy conversion*, Elsevier, 2012.

42 A. H. Reshak, *Phys. Chem. Chem. Phys.*, 2018, **20**, 8848–8858.

43 N. T. Hahn and C. B. Mullins, *Chem. Mater.*, 2010, **22**, 6474–6482.

44 W.-J. Yin, H. Tang, S.-H. Wei, M. M. Al-Jassim, J. Turner and Y. Yan, *Phys. Rev. B*, 2010, **82**, 45106.

45 M. Califano, R. Lu and Y. Zhou, *ACS Nano*, 2021, **15**, 20181–20191.

46 K. M. Reddy, S. V Manorama and A. R. Reddy, *Mater. Chem. Phys.*, 2003, **78**, 239–245.

47 J. Guo, in *Proc.SPIE*, 2007, vol. 6650.

48 M. I. Abedin, A. Islam and Q. D. Hossain, in *2015 IEEE International Conference on Telecommunications and Photonics (ICTP)*, 2015, pp. 1–4.

49 I. G. Lezama, A. Arora, A. Ubaldini, C. Barreteau, E. Giannini, M. Potemski and A. F. Morpurgo, *Nano Lett.*, 2015, **15**, 2336–2342.

50 J. Kangsabanik, M. K. Svendsen, A. Taghizadeh, A. Crovetto and K. S. Thygesen, *J. Am. Chem. Soc.*, 2022, **144**, 19872–19883.

51 M. A. Hadi, M. N. Islam and J. Podder, *RSC Adv.*, 2022, **12**, 15461–15469.

52 L.-D. Yuan, H.-X. Deng, S.-S. Li, S.-H. Wei and J.-W. Luo, *Phys. Rev. B*, 2018, **98**, 245203.

53 N. Huang, C. Lin and M. L. Povinelli, *J. Opt.*, 2012, **14**, 24004.

54 D. Liu, W. Zha, R. Yuan, B. Lou and R. Sa, *RSC Adv.*, 2020, **10**, 36734–36740.

55 F. Odobel, L. Le Pleux, Y. Pellegrin and E. Blart, *Acc. Chem. Res.*, 2010, **43**, 1063–1071.

56 M. T. Mayer, *Curr. Opin. Electrochem.*, 2017, **2**, 104–110.

57 Z. Zhang and J. T. Yates Jr, *Chem. Rev.*, 2012, **112**, 5520–5551.

58 L. Chen, J. Yang, S. Klaus, L. J. Lee, R. Woods-Robinson, J. Ma, Y. Lum, J. K. Cooper, F. M. Toma, L.-W. Wang, I. D. Sharp, A. T. Bell and J. W. Ager, *J. Am. Chem. Soc.*, 2015, **137**, 9595–9603.

59 B. Iandolo, B. Wickman, I. Zorić and A. Hellman, *J. Mater. Chem. A*, 2015, **3**, 16896–16912.

60 S. Li, W. Xu, L. Meng, W. Tian and L. Li, *Small Sci.*, 2022, **2**, 2100112.

61 J. R. Lince, D. J. Carré and P. D. Fleischauer, *Phys. Rev. B*, 1987, **36**, 1647.

62 E. Yablonovitch, B. J. Skromme, R. Bhat, J. P. Harbison and T. J. Gmitter, *Appl. Phys. Lett.*, 1989, **54**, 555–557.

63 S. Corby, E. Pastor, Y. Dong, X. Zheng, L. Francàs, M. Sachs, S. Selim, A. Kafizas, A. A. Bakulin and J. R. Durrant, *J. Phys. Chem. Lett.*, 2019, **10**, 5395–5401.

64 M. Barzgar Vishlaghi, A. Kahraman and S. Kaya, *J. Phys. Chem. C*, 2019, **124**, 1337–1345.

65 Z. Pan, J. A. Röhr, Z. Ye, Z. S. Fishman, Q. Zhu, X. Shen and S. Hu, *Sustain. Energy Fuels*, 2019, **3**, 850–864.

66 P. F. Weller, *J. Chem. Educ.*, 1971, **48**, 831.

67 N. Balkan, A. Erol, N. Balkan and A. Erol, *Semicond. Optoelectron. Basics Appl.*, 2021, 37–78.

68 J. C. Inkson, *J. Phys. C Solid State Phys.*, 1976, **9**, 1177.

69 M. P. Mazzeo and L. Restuccia, *Energy*, 2011, **36**, 4577–4584.

70 Y. J. Jang and J. S. Lee, *ChemSusChem*, 2019, **12**, 1835–1845.

71 S. Y. Tee, K. Y. Win, W. S. Teo, L.-D. Koh, S. Liu, C. P. Teng and M.-Y. Han, *Adv. Sci.*, 2017, **4**, 1600337.

72 M. W. Wanlass, K. A. Emery, T. A. Gessert, G. S. Horner, C. R. Osterwald and T. J. Coutts, *Sol. Cells*, 1989, **27**, 191–204.

73 C. Jiang, J. Wu, S. J. A. Moniz, D. Guo, M. Tang, Q. Jiang, S. Chen, H. Liu, A. Wang, T. Zhang and J. Tang, *Sustain. Energy Fuels*, 2019, **3**, 814–822.

74 S. Hu, M. R. Shaner, J. A. Beardslee, M. Lichterman, B. S. Brunschwig and N. S. Lewis, *Science*, 2014, **344**, 1005–1009.

75 I. V Bagal, M. Arunachalam, A. Waseem, A. Abdullah, S. H. Kang and S.-W. Ryu, *Appl. Surf. Sci.*, 2021, **558**, 149873.

76 H. J. T. Nkuissi, F. K. Konan, B. Hartiti and J.-M. Ndjaka, in *Reliability and Ecological Aspects of Photovoltaic Modules*, IntechOpen, 2020.

77 Y. Park and B. Park, *Results Phys.*, 2018, **11**, 162–165.

78 M. M. Rahman, M. R. Karim, H. F. Alharbi, B. Aldokhayel, T. Uzzaman and H. Zahir, *Chem. – An Asian J.*, 2021, **16**, 902–921.

79 J. Godt, F. Scheidig, C. Grosse-Siestrup, V. Esche, P. Brandenburg, A. Reich and D. A. Groneberg, *J. Occup. Med. Toxicol.*, 2006, **1**, 22.

80 J. Kegel, I. M. Povey and M. E. Pemble, *Nano energy*, 2018, **54**, 409–428.

81 P. V Raghavendra and J. S. Bhat, in *AIP Conference Proceedings*, AIP Publishing, 2017, vol. 1832, p. 80067.

82 J. Han and Z. Liu, *ACS Appl. Energy Mater.*, 2021, **4**, 1004–1013.

83 S. Goldsmith, E. Çetinörgü and R. L. Boxman, *Thin Solid Films*, 2009, **517**, 5146–5150.

84 E. Elangovan and K. Ramamurthi, *Appl. Surf. Sci.*, 2005, **249**, 183–196.

85 G. Zheng, J. Wang, H. Liu, V. Murugadoss, G. Zu, H. Che, C. Lai, H. Li, T. Ding, Q. Gao and Z. Guo, *Nanoscale*, 2019, **11**, 18968–18994.

86 B. S. Kalanoor, H. Seo and S. S. Kalanur, *Mater. Sci. Energy Technol.*, 2018, **1**, 49–62.

87 H. Fallah Moafi, M. Zanjanchi and A. Fallah shojaei, *Tungsten-doped ZnO nanocomposite: Synthesis, characterization, and highly active photocatalyst toward dye photodegradation*, 2013, vol. 139.

88 K. Manthiram and A. P. Alivisatos, *J. Am. Chem. Soc.*, 2012, **134**, 3995–3998.

89 A. Awsha, S. Alazoumi and B. Elhub, *Albahit J. Appl. Sci.*, 2021, **2**, 98936.

90 Y. Bai, I. Mora-Sero, F. De Angelis, J. Bisquert and P. Wang, *Chem. Rev.*, 2014, **114**, 10095–10130.

91 J.-X. Jian, V. Jokubavicius, M. Syväjärvi, R. Yakimova and J. Sun, *ACS Nano*, 2021, **15**, 5502–5512.

92 M. Xu, Y. R. Girish, K. P. Rakesh, P. Wu, H. M. Manukumar, S. M. Byrappa, Udayabhanu and K. Byrappa, *Mater. Today Commun.*, 2021, **28**, 102533.

93 J. Jian and J. Sun, *Sol. RRL*, 2020, **4**, 2000111.

94 M. J. Katz, S. C. Riha, N. C. Jeong, A. B. F. Martinson, O. K. Farha and J. T. Hupp, *Coord. Chem. Rev.*, 2012, **256**, 2521–2529.

95 R. Zboril, M. Mashlan and D. Petridis, *Chem. Mater.*, 2002, **14**, 969–982.

96 A. M. Jubb and H. C. Allen, *ACS Appl. Mater. Interfaces*, 2010, **2**, 2804–2812.

97 Z. Landolsi, I. Ben Assaker, R. Chtourou and S. Ammar, *J. Mater. Sci. Mater. Electron.*, 2018, **29**, 8176–8187.

98 M. Rooth, A. Johansson, K. Kukli, J. Aarik, M. Boman and A. Hårsta, *Chem. Vap. Depos.*, 2008, **14**, 67–70.

99 M. Barroso, C. A. Mesa, S. R. Pendlebury, A. J. Cowan, T. Hisatomi, K. Sivula, M. Grätzel, D. R. Klug and J. R. Durrant, *Proc. Natl. Acad. Sci.*, 2012, **109**, 15640–15645.

100 Y. Zhang, H. Ji, W. Ma, C. Chen, W. Song and J. Zhao, *Mol.* , 2016, 21.

101 T.-Y. Yang, H.-Y. Kang, K. Jin, S. Park, J.-H. Lee, U. Sim, H.-Y. Jeong, Y.-C. Joo and K. T. Nam, *J. Mater. Chem. A*, 2014, **2**, 2297–2305.

102 Z. D. Pozun and G. Henkelman, *J. Chem. Phys.*, 2011, **134**, 224706.

103 P. RAJAPANDI, G. VIRUTHAGIRI and N. SHANMUGAM, *J. Mol. Struct.*,

2023, 135397.

104 Y. Negishi, K. Munakata, W. Ohgake and K. Nobusada, *J. Phys. Chem. Lett.*, 2012, **3**, 2209–2214.

105 S. Jensen and D. S. Kilin, *J. Phys. Condens. Matter*, 2015, **27**, 134207.

106 L. Dong, B. Yin, L. Zhang, Y. Yin and Y. Zhang, *Synth. Met.*, 2012, **162**, 119–125.

107 A. E. Shalan and M. M. Rashad, *Appl. Surf. Sci.*, 2013, **283**, 975–981.

108 S. Gahlawat, J. Singh, A. K. Yadav and P. P. Ingole, *Phys. Chem. Chem. Phys.*, 2019, **21**, 20463–20477.

109 S. Dewan, M. Tomar, R. P. Tandon and V. Gupta, *J. Appl. Phys.*, 2017, **121**, 215307.

110 K. Tang, S.-L. Gu, J.-D. Ye, S.-M. Zhu, R. Zhang and Y.-D. Zheng, *Chinese Phys. B*, 2017, **26**, 47702.

111 N. Mirbagheri, D. Wang, C. Peng, J. Wang, Q. Huang, C. Fan and E. E. Ferapontova, *ACS Catal.*, 2014, **4**, 2006–2015.

112 D. Zheng, X. He, W. Xu and X. Lu, *Mater. Res. Bull.*, 2017, **96**, 354–359.

113 J. Deng, J. Zhong, A. Pu, D. Zhang, M. Li, X. Sun and S.-T. Lee, *J. Appl. Phys.*, 2012, **112**, 84312.

114 D. Wang, H. Chen, G. Chang, X. Lin, Y. Zhang, A. Aldalbahi, C. Peng, J. Wang and C. Fan, *ACS Appl. Mater. Interfaces*, 2015, **7**, 14072–14078.

115 P. Biswas, A. Ainabayev, A. Zhussupbekova, F. Jose, R. O’Connor, A. Kaisha, B. Walls and I. V Shvets, *Sci. Rep.*, 2020, **10**, 7463.

116 S. Krehula, G. Štefanić, K. Zadro, L. Kratofil Krehula, M. Marciuš and S. Musić, *J. Alloys Compd.*, 2012, **545**, 200–209.

117 M. Zhang, W. Luo, Z. Li, T. Yu and Z. Zou, *Rare Met.*, 2011, **30**, 38–41.

118 M. Seki, H. Yamahara and H. Tabata, *Appl. Phys. Express*, 2012, **5**, 115801.

119 J. Su, J. Wang, C. Liu, B. Feng, Y. Chen and L. Guo, *RSC Adv.*, 2016, **6**, 101745–101751.

120 S. S. Shinde, R. A. Bansode, C. H. Bhosale and K. Y. Rajpure, *J. Semicond.*, 2011, **32**, 13001.

121 A. Kleiman-Shwarsctein, M. N. Huda, A. Walsh, Y. Yan, G. D. Stucky, Y.-S. Hu, M. M. Al-Jassim and E. W. McFarland, *Chem. Mater.*, 2010, **22**, 510–517.

122 A. Zaleska-Medynska, *Metal Oxide-based Photocatalysis: Fundamentals and Prospects for Application*, Elsevier, 2018.

123 S. Krehula, M. Ristić, M. Reissner, S. Kubuki and S. Musić, *J. Alloys Compd.*, 2017, **695**, 1900–1907.

124 S. Li, J. Cai, Y. Mei, Y. Ren and G. Qin, *Int. J. Photoenergy*.

125 T. Kotrla, Š. Paušová, M. Zlámal, M. Neumann-Spallart and J. Krýsa, *Catal. Today*, 2018, **313**, 2–5.

126 L. Courtney-Davies, C. Ciobanu, M. W. Richardson, N. Prosser, M. Verdugo Ihl, B. Wade, S. Gilbert, K. Ehrig and N. Cook, *Synthesis of U-Pb doped hematite using a hydrated ferric oxide approach*, 2019, vol. 513.

127 H. K. Dunn, J. M. Feckl, A. Müller, D. Fattakhova-Rohlfing, S. G. Morehead, J. Roos, L. M. Peter, C. Scheu and T. Bein, *Phys. Chem. Chem. Phys.*, 2014, **16**, 24610–24620.

128 M. Forster, R. J. Potter, Y. Yang, Y. Li and A. J. Cowan, *ChemPhotoChem*, 2017, **2**, 183–189.

129 A. Klein, C. Körber, A. Wachau, F. Säuberlich, Y. Gassenbauer, S. P. Harvey, D. E. Proffit and T. O. Mason, *Materials (Basel).*, 2010, **3**, 4892–4914.

130 P. I. Kyesmen, N. Nombona and M. Diale, *Surfaces and Interfaces*, 2019, **17**, 100384.

131 L. Steier, I. Herraiz-Cardona, S. Gimenez, F. Fabregat-Santiago, J. Bisquert, S. D. Tilley and M. Grätzel, *Adv. Funct. Mater.*, 2014, **24**, 7681–7688.

132 C. Ding, Z. Wang, J. Shi, T. Yao, A. Li, P. Yan, B. Huang and C. Li, *ACS Appl. Mater. Interfaces*, 2016, **8**, 7086–7091.

133 K. C. Bedin, B. Mouriño, I. Rodríguez-Gutiérrez, J. B. S. Junior, G. T. dos Santos, J. Bettini, C. A. R. Costa, L. Vayssieres and F. L. Souza, *Chinese J. Catal.*, 2022, **43**, 1247–1257.

134 Z. Luo, T. Wang, J. Zhang, C. Li, H. Li and J. Gong, *Angew. Chemie Int. Ed.*, 2017, **56**, 12878–12882.

135 Y. Liang, C. S. Enache and R. van de Krol, *Int. J. Photoenergy*.

136 T. Hisatomi, H. Dotan, M. Stefik, K. Sivula, A. Rothschild, M. Graetzel and N. Mathews, *Adv. Mater.*, 2012, **24**, 2699–2702.

137 O. Zandi, J. A. Beardslee and T. Hamann, *J. Phys. Chem. C*, 2014, **118**, 16494–16503.

138 K. Sivula, R. Zboril, F. Le Formal, R. Robert, A. Weidenkaff, J. Tucek, J. Frydrych and M. Grätzel, *J. Am. Chem. Soc.*, 2010, **132**, 7436–7444.

139 A. Subramanian, A. Annamalai, H. H. Lee, S. H. Choi, J. Ryu, J. H. Park and J. S. Jang, *ACS Appl. Mater. Interfaces*, 2016, **8**, 19428–19437.

140 S. Pancharatnam, G. Karve, J. Wynne, B. Mendoza, S. DeVries, R. N. Pujari, M. Breton, A. Carr, L. White and G. Rodriguez, *IEEE Trans. Semicond. Manuf.*, 2019, **32**, 374–380.

141 J. W. Park, M. A. Mahadik, H. Ma, G. W. An, H. H. Lee, S. H. Choi, W.-S. Chae,

H.-S. Chung and J. S. Jang, *ACS Sustain. Chem. Eng.*, 2019, **7**, 6947–6958.

142 T. Hisatomi, F. Le Formal, M. Cornuz, J. Brillet, N. Tétreault, K. Sivula and M. Grätzel, *Energy Environ. Sci.*, 2011, **4**, 2512–2515.

143 Z. Luo, C. Li, S. Liu, T. Wang and J. Gong, *Chem. Sci.*, 2017, **8**, 91–100.

144 D. Chen and Z. Liu, *ChemSusChem*, 2018, **11**, 3438–3448.

145 O. Zandi, B. M. Klahr and T. W. Hamann, *Energy Environ. Sci.*, 2013, **6**, 634–642.

146 L. Han, F. F. Abdi, R. van de Krol, R. Liu, Z. Huang, H.-J. Lewerenz, B. Dam, M. Zeman and A. H. M. Smets, *ChemSusChem*, 2014, **7**, 2832–2838.

147 P. Liu, C. Wang, L. Wang, X. Wu, L. Zheng and H. G. Yang, *Research*.

148 A. M. Ganose and D. O. Scanlon, *J. Mater. Chem. C*, 2016, **4**, 1467–1475.

149 Y. Yang, H. Ma, J. Zhuang and X. Wang, *Inorg. Chem.*, 2011, **50**, 10143–10151.

150 S. K. Mohapatra, S. E. John, S. Banerjee and M. Misra, *Chem. Mater.*, 2009, **21**, 3048–3055.

151 C. Hu, Z. Gao and X. Yang, *Chem. Lett.*, 2006, **35**, 1288–1289.

152 L.-S. Zhong, J.-S. Hu, H.-P. Liang, A.-M. Cao, W.-G. Song and L.-J. Wan, *Adv. Mater.*, 2006, **18**, 2426–2431.

153 Z. Zhang, M. F. Hossain and T. Takahashi, *Appl. Catal. B Environ.*, 2010, **95**, 423–429.

154 L. Vayssieres, N. Beermann, S.-E. Lindquist and A. Hagfeldt, *Chem. Mater.*, 2001, **13**, 233–235.

155 R. Wang, Y. Chen, Y. Fu, H. Zhang and C. Kisielowski, *J. Phys. Chem. B*, 2005, **109**, 12245–12249.

156 A. Kleiman-Shwarsctein, Y.-S. Hu, A. J. Forman, G. D. Stucky and E. W.

McFarland, *J. Phys. Chem. C*, 2008, **112**, 15900–15907.

157 Y. Wang, W. Tian, L. Chen, F. Cao, J. Guo and L. Li, *ACS Appl. Mater. Interfaces*, 2017, **9**, 40235–40243.

158 H. M. Fan, G. J. You, Y. Li, Z. Zheng, H. R. Tan, Z. X. Shen, S. H. Tang and Y. P. Feng, *J. Phys. Chem. C*, 2009, **113**, 9928–9935.

159 P. Kissinger and W. R. Heineman, *Laboratory Techniques in Electroanalytical Chemistry, Revised and Expanded*, CRC Press, 2018.

160 F. E. Bedoya-Lora, A. Hankin, I. Holmes-Gentle, A. Regoutz, M. Nania, D. J. Payne, J. T. Cabral and G. H. Kelsall, *Electrochim. Acta*, 2017, **251**, 1–11.

161 S. de Gendt, *Atomic Layer Deposition Applications 5*, Electrochemical Society, 2009.

162 D. Astruc, *Eur. J. Inorg. Chem.*, 2017, **2017**, 6–29.

163 O. Nilsen, M. Lie, S. Foss, H. Fjellvåg and A. Kjekshus, *Appl. Surf. Sci.*, 2004, **227**, 40–47.

164 M. Lie, H. Fjellvåg and A. Kjekshus, *Thin Solid Films*, 2005, **488**, 74–81.

165 J. Bachmann, J. Jing, M. Knez, S. Barth, H. Shen, S. Mathur, U. Gösele and K. Nielsch, *J. Am. Chem. Soc.*, 2007, **129**, 9554–9555.

166 M. H. Lee, J. H. Park, H. S. Han, H. J. Song, I. S. Cho, J. H. Noh and K. S. Hong, *Int. J. Hydrogen Energy*, 2014, **39**, 17501–17507.

167 A. Tamm, K. Kalam, H. Seemen, J. Kozlova, K. Kukli, J. Aarik, J. Link, R. Stern, S. Dueñas and H. Castán, *ACS omega*, 2017, **2**, 8836–8842.

168 K. Kukli, M. C. Dimri, A. Tamm, M. Kemell, T. Käämbre, M. Vehkamäki, M. Puttaswamy, R. Stern, I. Kuusik, A. Kikas, M. Tallarida, D. Schmeißer, M. Ritala and M. Leskelä, *ECS J. Solid State Sci. Technol.*, 2012, **2**, N45–N54.

169 A. B. F. Martinson, M. J. DeVries, J. A. Libera, S. T. Christensen, J. T. Hupp, M. J. Pellin and J. W. Elam, *J. Phys. Chem. C*, 2011, **115**, 4333–4339.

170 B. Klahr, S. Gimenez, F. Fabregat-Santiago, J. Bisquert and T. W. Hamann, *Energy Environ. Sci.*, 2012, **5**, 7626–7636.

171 B. Klahr, S. Gimenez, F. Fabregat-Santiago, T. Hamann and J. Bisquert, *J. Am. Chem. Soc.*, 2012, **134**, 4294–4302.

172 J. R. Schneider, J. G. Baker and S. F. Bent, *Adv. Mater. Interfaces*, 2020, **7**, 2000318.

173 D. Peeters, A. Sadlo, K. Lowjaga, O. Mendoza Reyes, L. Wang, L. Mai, M. Gebhard, D. Rogalla, H.-W. Becker, I. Giner, G. Grundmeier, D. Mitoraj, M. Grafen, A. Ostendorf, R. Beranek and A. Devi, *Adv. Mater. Interfaces*, 2017, **4**, 1700155.

174 J. R. Scheffe, A. Francés, D. M. King, X. Liang, B. A. Branch, A. S. Cavanagh, S. M. George and A. W. Weimer, *Thin Solid Films*, 2009, **517**, 1874–1879.

175 H. Van Bui, F. Grillo and J. R. van Ommen, *Chem. Commun.*, 2017, **53**, 45–71.

176 B. M. Klahr, A. B. F. Martinson and T. W. Hamann, *Langmuir*, 2011, **27**, 461–468.

177 X. Li, N. C. Fan and H. J. Fan, *Chem. Vap. Depos.*, 2013, **19**, 104–110.

178 G. Jerkiewicz, *ACS Catal.*, 2020, **10**, 8409–8417.

179 T.-G. Kim, B. Joshi, C.-W. Park, E. Samuel, M.-W. Kim, M. T. Swihart and S. S. Yoon, *J. Alloys Compd.*, 2019, **798**, 35–44.

180 C. Toussaint, H. L. Le Tran, P. Colson, J. Dewalque, B. Vertruyen, B. Gilbert, N. D. Nguyen, R. Cloots and C. Henrist, *J. Phys. Chem. C*, 2015, **119**, 1642–1650.

181 S. D. Tilley, M. Cornuz, K. Sivula and M. Grätzel, *Angew. Chemie Int. Ed.*, 2010,

49, 6405–6408.

182 X. Shi, K. Zhang and J. H. Park, *Int. J. Hydrogen Energy*, 2013, **38**, 12725–12732.

183 D. Pal, D. Maity, A. Sarkar, D. De, A. Raj and G. G. Khan, *ACS Appl. Energy Mater.*, 2022, **5**, 15000–15009.

184 C. Du, X. Yang, M. T. Mayer, H. Hoyt, J. Xie, G. McMahon, G. Bischoping and D. Wang, *Angew. Chemie Int. Ed.*, 2013, **52**, 12692–12695.

185 C. Li, Z. Luo, T. Wang and J. Gong, *Adv. Mater.*, 2018, **30**, 1707502.

186 J.-W. Jang, C. Du, Y. Ye, Y. Lin, X. Yao, J. Thorne, E. Liu, G. McMahon, J. Zhu, A. Javey, J. Guo and D. Wang, *Nat. Commun.*, 2015, **6**, 7447.

187 J. Han, X. Zong, Z. Wang and C. Li, *Phys. Chem. Chem. Phys.*, 2014, **16**, 23544–23548.

Chapter 3
Experimental Techniques

3.0 Introduction

Throughout this research project it has been necessary to use a multitude of techniques to achieve the outcomes desired for each study. This chapter will discuss the techniques used in this project, such as Atomic Layer Deposition (ALD) and electrochemistry, which have been used extensively throughout the PhD and formed the foundation of the work.

This chapter will also cover other experimental techniques utilised in various capacities in the research and touch upon the role they played in forming the final conclusions reached.

3.1 Atomic Layer Deposition

Atomic Layer Deposition, or ALD, is a deposition method used to create thin films on surfaces. It gets its name from the way in which it builds thin films, which is atomic layer by atomic layer. Due to the precision involved in the process, it allows for the building of highly-ordered films, even on topographically challenging substrates.

Belonging to the overarching group of chemical vapour deposition (CVD), it is part of the vacuum deposition family, along physical vapour deposition (PVD) techniques such as laser ablation, sputtering and evaporation deposition. Differing from one another, CVD techniques are somewhat monophasic in nature, using chemical vapours to form the thin films created.[1] In contrast, PVD methods require the source material (a solid or a liquid) to undergo a phase change in order to produce the final product, usually utilising a high-powered energy source such as a laser to achieve this.[2]

Though it is possible to generalise ALD as a CVD technique, there are some key divergences between ALD and what is commonly referred to as CVD. While both processes aim to produce thin films, ALD is a more restrained and controlled version of CVD, resulting in highly conformal, almost diaphanous films.[3] This is due to key experimental differences between the two techniques, which will be examined in more detail in subsequent sections.

3.1.1 History of ALD

As of 2022, atomic layer deposition has existed in some form or another for close to 50 years. Interestingly, its main use to this day is similar to that for which it was created: the optimisation of electronics. Initially developed as an answer to the amorphicity issues faced by thin film electronics manufacture in the 1970s, ALD, or Atomic Layer Epitaxy (ALE) as it was originally patented, was designed to produce a thin, well-structured, crystal film.[4]

The mastermind behind the research, Tuomo Suntola, had theorised that in order to produce a well-ordered compound, the reactants needed to form stronger bonds with one another, as opposed to with themselves. With this hypothesis, the idea that there was a necessity of sequential introduction of the reactants evolved, forming the basis of modern ALD. Tuomo Suntola did not stop there however, he continued to calculate the specific requirements for the production of zinc sulphide (ZnS), producing a low-pressure system that heated the zinc and sulphur sources separately in a vacuum environment to obtain reactive vapours.[5] This was to be the first example of an ALD reactor, which successfully produced ZnS films, albeit in an inefficient manner.

Over time this technique was researched thoroughly to gain greater understanding of the surface science at work. Modern day ALD is a honed version of the original, with decades of work dedicated to exploring the fundamentals of the subject, producing vast pieces of dedicated machinery and establishing consistent growth methods to produce many films.[6]

3.1.2 Principles of ALD

As was previously stated, the basis for the invention of ALD was that reactants will form more ordered films if they are introduced in sequence rather than all at once. Though there are many factors at play during ALD experiments, there are just a few things that could be considered to be core principals or core requirements of ALD. These are assumptions or practices that ALD experiments rely on in order to consistently produce structured thin films. In summary these are: [7–9]

- A cyclic, sequential methodology behind ALD experiments
- Reactive and isolated precursors
- Usually a low pressure/vacuum environment
- Suitable growth substrate
- Self-limiting and self-ordering behaviour

These elements integrate to form the practice of ALD as a whole, with each one playing a key role in making ALD the precise technique that it is.

3.1.3 Experimental layout

Experimental setups for ALD can vary to some degree, but the quintessential procedure remains the same. The machine, known as a reactor, has a main chamber area where the substrates for growth will be placed. External to this, the reactants, known as precursors, are kept separate from one another and the main deposition area.[10] This is typically reinforced by the use of valves, guaranteeing that the precursors aren't contaminated during the reaction and that the only reaction is the one in the main chamber following the introduction of the second precursor. Additionally, inert gases often flowed through any lines within the reactor, to further minimise contamination. Here is where the main difference between CVD and ALD arises, as the non-overlapping nature of ALD sequences produces a very different result to CVD methods.[3]

It was mentioned previously that there is a cyclic, sequential manner to all ALD experiments, and this is the next step to ensuring the uniformity of the product. A typical ALD sequence is a multistep process that involves what is known as pulses (of the reactive species) and purges (of any unwanted byproducts, including residual precursor and reaction products).[11] The sequence runs as an ABCB ABCB cyclic process of pulse-purge-pulse-purge to build the film layer by layer (Figure 7).

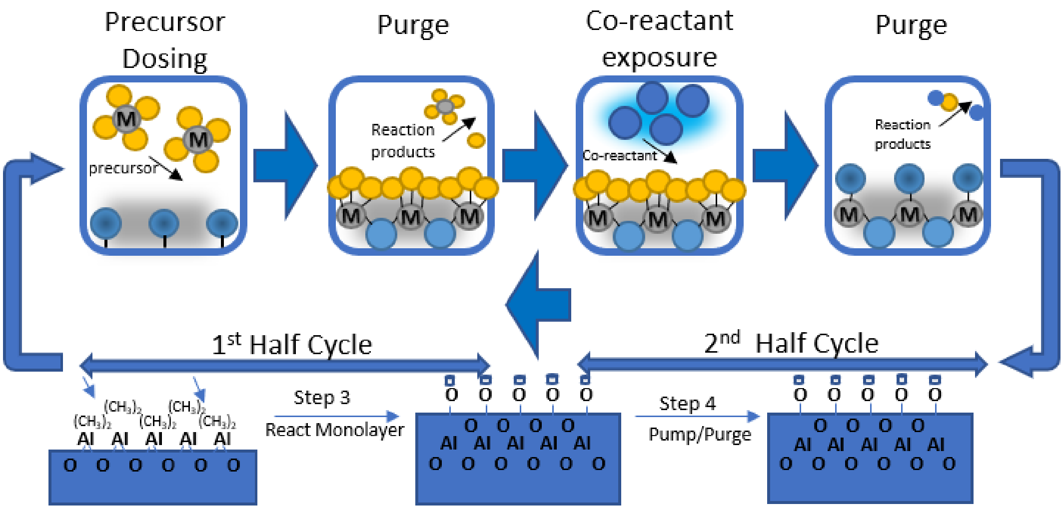

Figure 7: Schematic highlighting sequential sequences in an ALD process. Recreated from reference.[12]

Precursor A is introduced to the chamber and chemisorbs to the chosen substrate. This chemisorption helps in ensuring that the process is self-limiting. Compared to physisorption, chemisorption involves the chemical bonding of the precursor to the molecules on the substrate surface.[13] Physisorption on the other hand involves Van der Waals forces and hence lacks specificity and self-limiting capabilities. Following the dose, the excess precursor is then removed, or 'purged', from the system using an inert flow gas.[14] Upon normalisation of the base conditions the next reactive species, precursor B, is injected and the chamber purged once more - this whole process is considered to be one cycle. The purging process between pulses removes the possibility of reactions occurring in the chamber, as the only reactive species left is that which is bound to the substrate. Resultantly, the film is built on the surface atomic layer by atomic layer. For any given process a growth rate can then be determined per cycle and in using this it is possible to produce films of an intended nanometre (nm) thickness.[15]

3.1.4 Self-governing precursor behaviour

One of the main assumptions for ALD processes is that there will be a saturation point for the substrate at which, no matter the amount of precursor used, no further growth will be exhibited. As the substrate is basically a material with a limited number of active sites, there will be a point when every active site is occupied and no further molecules can adhere; hence, the process is self-limiting.[11,16] This point can be found relatively easily with a growth study that varies the precursor dose times and monitors the thickness of the resulting film. When plotted against one another, self-limiting growth is apparent if the growth flattens after a certain amount of precursor exposure (Figure 8). This is the point at which all active sites are occupied and further exposure results in no change.

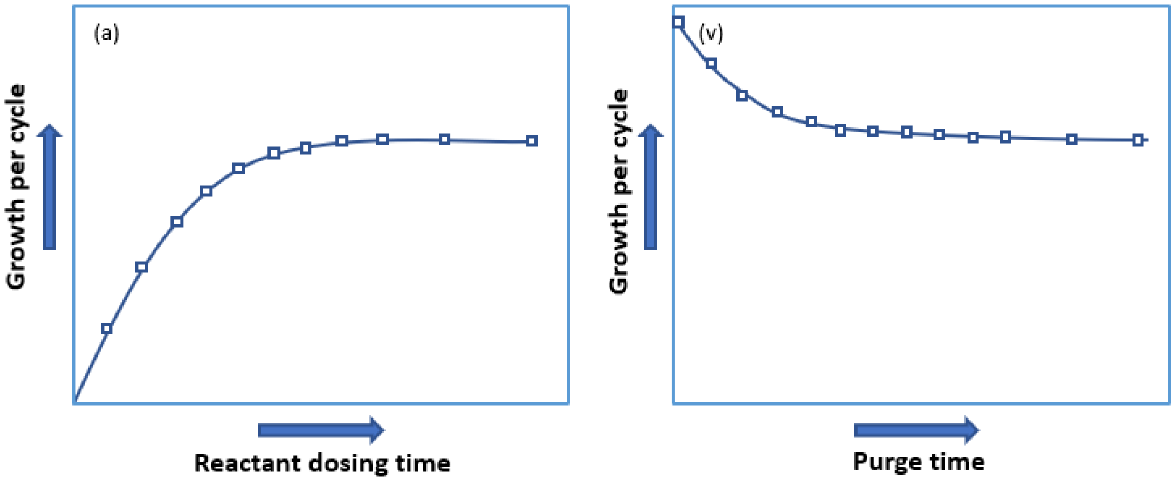

Figure 8: Schematic showing a) the relationship between grown and dose time and v) the relationship between growth and purge time. Recreated from reference.[12]

Similarly, the purge time should be sufficient as to remove any remaining, unbound precursor or by-products that may undergo CVD type reactions in the second pulse step, but excessive purging will yield limited negative consequences. Providing that the precursor is effectively adsorbed on to the surface, a longer purge time will not impact the expected ALD growth for an ideal growth process.[17] For some non-ideal processes, excessive purge times can lead to desorption, reducing the possible growth of the film.

Additionally, there is the base assumption that any given reactant will adsorb and react in an expected, thermodynamically favourable fashion. That is, it will adsorb to the surface and, providing there is adequate activation energy, the co-reactant will preferentially substitute with the previously bound chemical group.[13,18] Within this process the atoms will react and orient in a way such as to find the most favourable oxidation state, coordination state, crystal structure (etc.) for the given compound. As a consequence of the aforementioned phenomena, the resulting film is assembled by self-ordering, self-limiting behaviours.

3.1.5 ALD process variables

On top of the sequence timing itself, there are numerous parameters that vary between different ALD processes. This includes variables such as chamber temperature, bubbler (the storage vessel for the precursors) temperature and gas flow, to name a few. Each variable is individualised to maximise growth for a specified reaction, taking into account factors such as precursor volatility and reaction dynamics to determine the most appropriate values.[14,19,20] These values can be tuned, as with the dose times, to create a smooth ALD process with a predictable substrate growth rate.

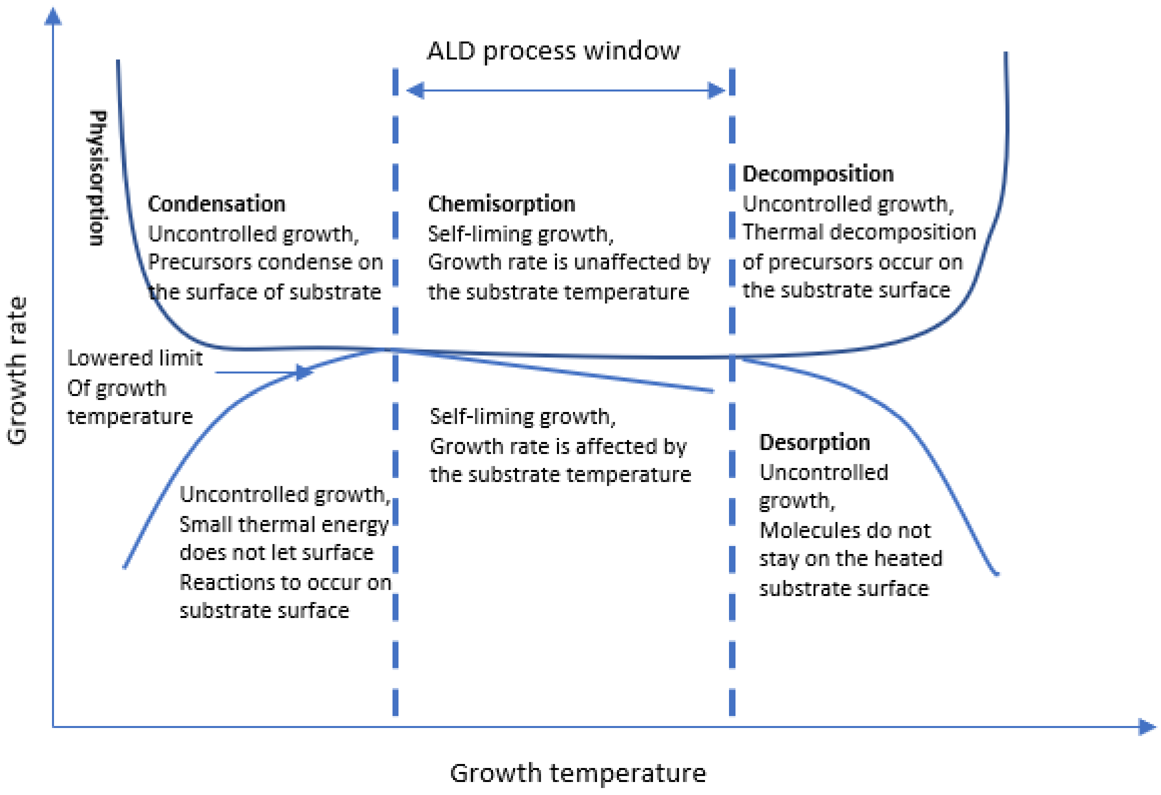

Figure 9: Diagram showing the relationship between growth rate and growth temperature. Recreated from reference.[14]

Growth temperature is especially important, with the effects of temperature extremes highlighted in Figure 9. Growth rate as a function of temperature is explored as part of the ALD process here, with an advantageous process window identified.

3.2 Plasma-Enhanced ALD

3.2.1 Precursor selection

As has been established, in your typical ALD process, precursors are added sequentially and reacted with another compound to produce the surface film. Oxygen-based coreactants such as water or O_2 gas can be reacted with metal precursors to produce metal oxides. Similarly, nitrogen-based compounds like ammonia make it viable for ALD nitrides, and so on.[21,22] This is logical as changing one of the reactive species will alter the final product. However, these reactions are not always very favourable, and a pure product with a reasonable growth rate can be tricky depending on the precursor. Volatile precursors, such as trimethylaluminium (TMA), will shed their methyl groups willingly resulting in a strong and predictable growth rate of ~1Å/cycle with water.[23,24] Other precursors are more problematic however depending on the chemical composition and their respective reactivity. In the case of more stable precursors, or in the interest of improving growth, it can be beneficial to use a co-reactant of a more unstable nature. For instance, water, a common oxygen source for ALD metal oxides, can be replaced with ozone gas (O_3).[25] This offers an alternative way of improving the reactivity in the chamber, as ozone gas is much less stable and is a more powerful oxidiser than water.[26] In making such a swap it is possible to improve the growth rate and sequence time for certain precursors.[27] However, as with any chemical reaction, a change to any component can also result in crystallinity and compositional variations, so it is important to ensure a balance.[28]

3.2.2 Plasma utilisation

Plasma Enhanced Atomic Layer Deposition, PEALD, is as its name suggests: ALD that is enhanced by using plasma technology. As has been discussed, using more reactive gases in the ALD process can improve growth for low reactivity precursors. In a similar fashion to ozone, plasma generated radicals offer a route to using more chemically inactive compounds in ALD processes.[29] Plasmas are generated by exciting gas molecules, ionising the gas and generating radicals.[30] This can be done in a number of ways including: DC-discharge, RF discharge and Microwave excitation.[31]

Plasma generators typically work by utilising an inert carrier gas and electrical currents to ionize a target gas, in this case oxygen, into a mix of radicals, anions and cations. These radicals possess more energy and are much more reactive than molecular oxygen, which can often improve the reaction dynamics to allow for better growth[32,33]

3.2.3 Limitations of Plasma Technology

Recombination was covered in chapter 1 as an issue within PEC cells, yet the similarities in the plasma generation process make recombination a threat here also. As there is a mix of species created it is plausible that these can recombine, as thermodynamics dictate would be favourable. This can occur in a free-flowing space, with (e.g.) oxygen radicals recombining to form molecular oxygen, and also at the surface.[34] High aspect ratio substrates are particularly susceptible to recombination issues due to their topography, as the chance of hitting an undesired reactive species increases with diffusion depth.[35] For this reason, PEALD may not be suitable for all processes, with rougher surfaces potentially facing more recombination issues.[36] Hence it is necessary to weigh the pros and cons for any given process to establish whether using plasma technology would be beneficial.

3.2.4 System setup

Experiments in this PhD were carried out using an Oxford Instruments OpAL ALD reactor equipped with a Meaglow hollow cathode plasma source (Meaglow stainless steel series 50) powered by a RF generator (Seren R301 RF source with an MC2 match box and AT6 Automatch controller). The hollow cathode in the Meaglow system was not cooled during operation to prevent precursor condensation. The plasma source was fed with argon (BOC research grade) and oxygen (BOC zero grade), with flow rates of each gas controlled by MFCs. The argon was also used as a carrier gas for the MO precursor and as a purge gas during ALD growth. The OpAL machine is a warm-wall reactor, in which the upper and lower chamber temperatures can be intendedly controlled, as can the sample platen. The reactor is pumped by an Adixen A103P dry pump, with the lines are heated to prevent condensation of precursors. The full setup can be seen in Figure 10.

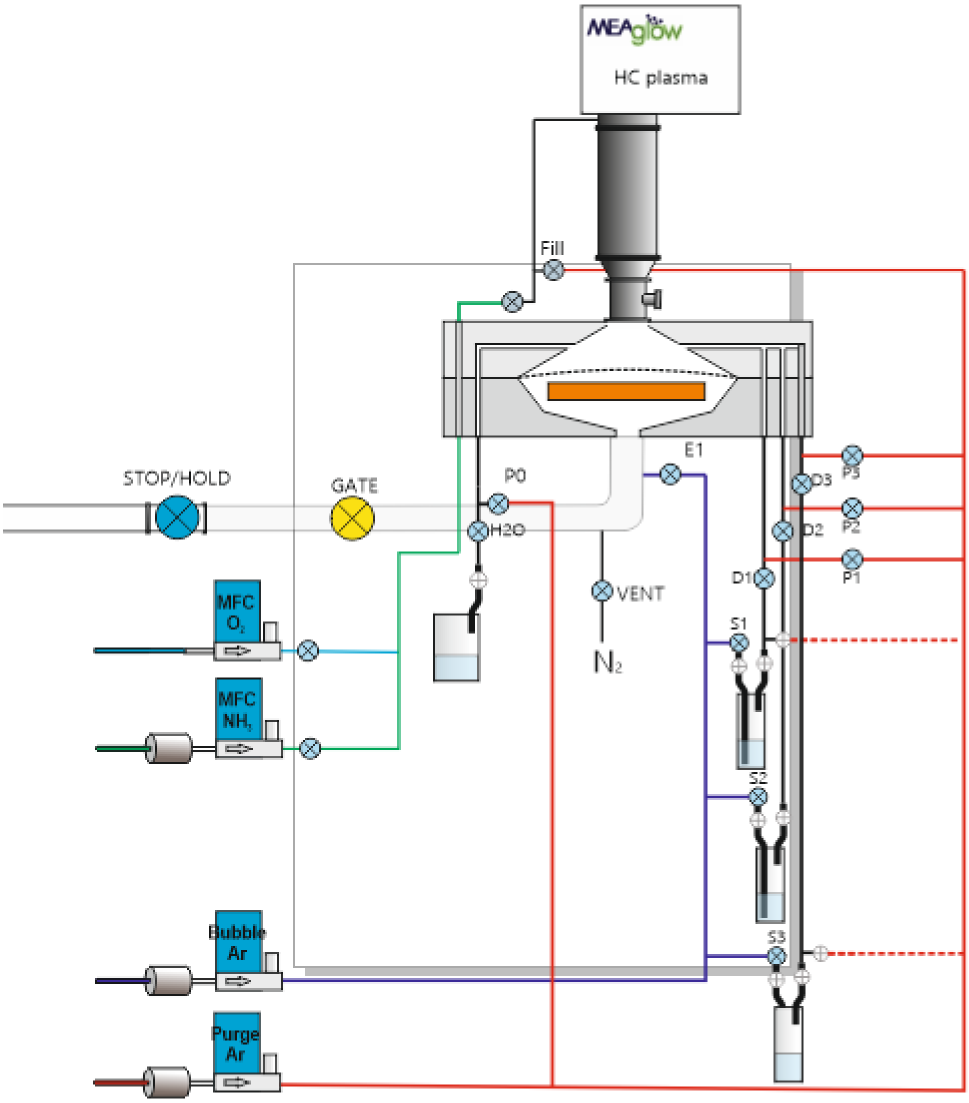

Figure 10: Schematic of the full reactor setup, including plasma source, gas lines and precursor pots.

The precursor used to produce hematite films during this project was ferrocene (Sigma Aldrich (F408-100G) 98%). This was delivered using vapour push mechanism, with dosing controlled by high-speed Swagelok ALD valves. Other precursors used in this project were TMA (SAFC-Hitech) and Titanium(IV) isopropoxide (≥97%, Sigma Aldrich), delivered via vapour draw and vapour push mechanisms respectively.

3.2.5 Custom equipment

For this project a custom bubbler to house the chosen precursor was designed, in order to overcome persistent issued caused by the precursor. This was designed with wider tubing to help prevent blockages, a lowered gas inlet to aid with the vapour push method and a glass body to make it easier to check powder levels and view any problems (Figure 11). Additionally, heating lines were added to the gas inlet pipes to reduce the possibility of cold areas and sublimation.

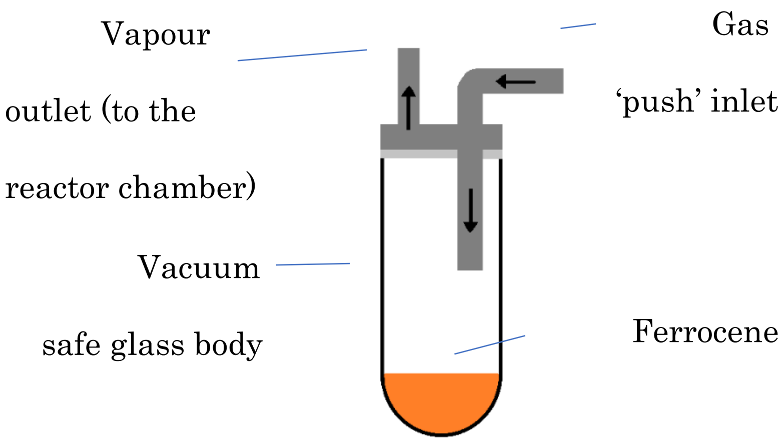

Figure 11: Custom built precursor 'bubbler' for ferrocene. 1/4" steel pipes make up the gas inlet and outlet, with glass body and rubber seal on steel cap.

3.2.6 Basic Process parameters

The key parameters to highlight for this process, that remained constant for the duration of the project are :

- Precursor temperature set to 80°C,
- Line temperatures were staggered, with the immediate line above the precursor at 90°C and the line above that at 100°C,

- Precursor vapour push gas flow was set to 50 sccm Ar (BOC research grade)
- Overall gas flow through lines was maintained at 150 sccm outside of dose stages.

3.3 Electrochemistry

There are many variations and experiments possible within the electrochemical field, though only a selection are used in this PhD. Chapter 1 introduced the concept of PEC cells and their role in sustainable hydrogen energy. This section will look more closely at the specific data acquisition methods used for testing PEC cells and their components, as relevant to this research.

3.3.1 Electrochemistry in a nutshell

Electrochemistry is an area of science concerned with the relationship between electron movement and chemical processes. In electrochemical reactions, the electrons partaking in the process do so as an electric current in a circuit, contrary to the electron exchange that occurs directly between atoms and ions in typical chemical reactions.[37] Conventionally, the reaction proceeds via a redox process, in which one species is reduced as the other oxidised. When this occurs spontaneously, as can occur in certain electrochemical cells (known as Galvanic/voltaic cells), the chemical energy is converted into electrical energy.[38] Conversely, current can be applied to a cell to convert the electrical energy to chemical; this will drive the redox reaction forward, producing the desired species. This setup is known as an electrolytic cell. Photoelectrochemical (PEC) cells have two distinct classes based on these two types; fundamentally, a PEC device that utilises light to produce electricity is known as a photovoltaic cell, whereas light driven chemical reactions are completed by photoelectrolytic cells.[39]

3.3.2 Experimental setup

For this research a custom designed transparent glass cell was used, containing a solution of 1M NaOH (Fischer, reagent grade, pH 13.6) prepared with distilled water as the electrolyte, with the working, reference and counter electrodes connected to three, separate, sealed inlet joints. In this instance the reference electrode consisted of a lab made Ag/AgCl reference electrode with a platinum wire used as counter. A 300W Xe lamp (Newport model 66902) was utilised as a light source (ca. 100mW cm^{-2}). For the subsequent techniques, a PalmSens3 or Bio-Logic SP-200 potentiostat was employed as a tool for data acquisition.

3.3.3 Electrochemical Techniques

The main electrochemical techniques used to obtain data in this research were:

- Linear Sweep Voltammetry (LSV) – Used to determine the peak current and ‘switch on’ point or onset for PEC devices, amongst other things. Involves sweeping the potential from a low voltage to a higher one in a linear fashion on the counter and reference electrodes, whilst measuring for the working one.[40] A typical sweep range here is -0.4V – 0.7V, to encompass the full OER range.[41] Illumination was carried out on the front and back side of the samples, to assess for differences (Figure 12).

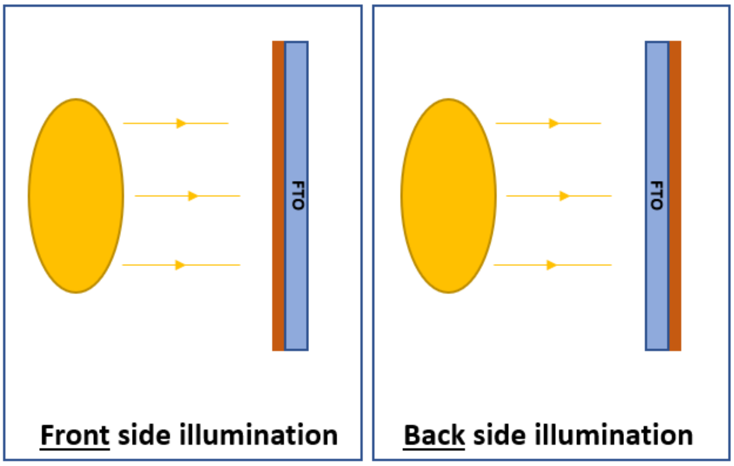

Figure 12: Experimental difference between front and back side illumination.

- Chopped LSV – Similar to the above LSV but with the light source manually ‘chopped’ repeatedly between dark and light. The resulting pattern of overshoots is hypothesized to be characteristic of the recombination behaviour of the photoanode in question.[42]
- Chronoamperometry – Electrochemical experiment wherein the potential is held at a given value (0.4V) and the current measured as a function of time. In this project that varied from 5 minutes, to over an hour. This provides information as to electron transfer events and photoanode stability in NaOH solution.[43]

3.4 Other Techniques

3.4.1 LEIS

Low Energy Ion Scattering (LEIS) is a surface sensitive analysis technique used to garner information as to the chemical and structural composition of a compound. It achieves this by directing particles at a substrate and measuring the resulting data, such as energies, velocities and positions, to accurately analyse the surface (Figure 13).[44]

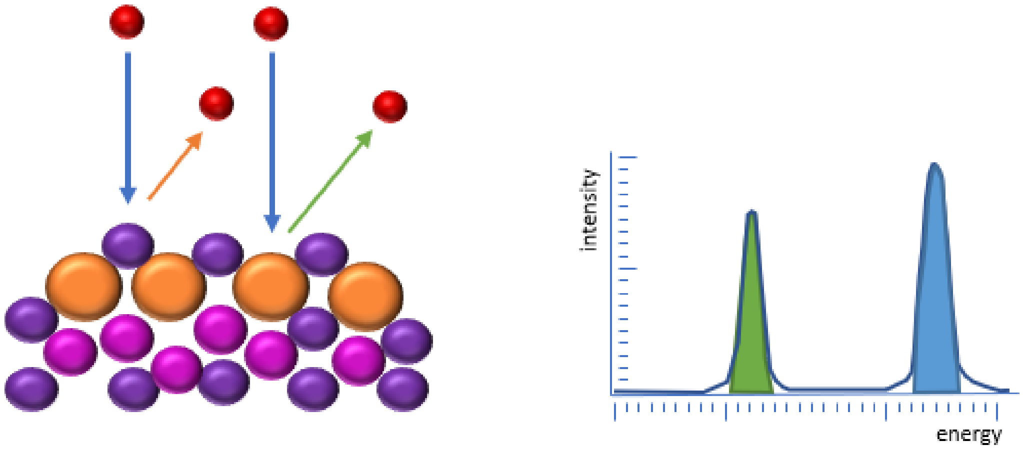

Figure 13: Surface interactions between ion beam and surface ions, with collisions at various angles. These angles and the velocities and energy of the ions allow for the formation of a LEIS spectra, which shows as peaks at different energy, with varying shapes and intensities. Adapted from reference.[44]

In this research LEIS has been deployed to find the specific elemental surface compositions of the samples both pre and post-anneal, as well as to determine the arrangement of atoms at greater depths.

An IonTOF Qtac100 LEIS machine was used for sample measurements in this project. A He/Ar beam was employed for analysis, as specified in the specific experiments. Samples were mounted onto the LEIS platform and manually transferred to the main chamber, using the gated vacuum system and push/pull levers. Samples were measured without heating. A high energy Ar beam was used to remove subsequent layers of substrate to record sub-surface measurements.

Some of the key properties of the IonTOF Qtac100 LEIS machine are highlighted in Table 1.

Table 1: Some key properties of the IonTOF LEIS machine are highlighted here. Adapted from IonTOF user manual, https://www.iontof.com.

Property	Key data	Notes
LEIS ion source	$^3He^+$, $^4He^+$, $^{20}Ne^+$, $^{40}Ar^+$	Up to 8keV. 1pA – 100nA
Charge compensation	Low energy electron source	Self-adjusting charge compensation source enables analysis of insulators
Base pressure	$<5.0\times10^{-10}$torr	
Sputter gun	0.2 – 2keV Ar^+ gun (up to 600nA @ 2keV)	Allows dual beam depth profiling

A 3 keV He^+ analysis beam was employed for surface spectra measurements, with the intensity of the scattered He^+ normalised to the ion beam current. A 1 keV Ar^+ sputter beam was employed for dynamic depth profiling. Dynamic depth profiles were taken following exposure to a sputter dose between ~5 x 10^{15} ions cm^{-1} -and _7 x 10^{14} ions cm^{-1}.

3.4.2 UV-VIS

Ultraviolet-Visible absorption spectroscopy, or UV-Vis as it is commonly named, measures the absorption of a compound over the ultraviolet and visible spectrum. This can at wavelengths ranging from 190-700nm of the electromagnetic spectrum.[45] As mentioned earlier electrons can absorb light to undergo a transition from a lower energy state to a higher one, and the gap that these electrons 'jump' from corresponds to a wavelength of light. The smaller the gap, the lower the energy requirement of the electrons, hence a longer wavelength of light absorbed; longer wavelengths correspond to a lower photon energy.[46] Briefly, this is because wavelength= speed / frequency and energy = frequency x Planck's constant, ergo higher frequencies equal smaller wavelengths and are equal to higher energy.[47] Absorption and reflectance spectroscopy utilising UV or visible light wavelengths is an inexpensive and simple method for determining some key material properties. Not only does this method inform on the % of light absorbed by a sample, which is a good indicator as to its potential use in photoelectronic devices, but spectral analysis can determine band-gap properties and transition dynamics.[48]

Measurements were recorded using a Shimadzu UV-2600 spectrophotometer, equipping reflectance or absorbance holders as needed. Reflectance measurements were recorded against an aluminium mirror (specular) and barium sulphate packed powder (diffuse). Absorbance measurements were referenced to a sample of clean FTO glass.

3.4.3 Film Growth Measurements

Film growth was ascertained using a combination of weight gain measurements and thin film ellipsometry.

Weight gain was carried out by recording the mass of the wafer pre-ALD and post-ALD using a microbalance sensitive to 0.00001g (Mettler Toledo Ltd, XS205DU analytical balance). The surface area coverage was then calculated and growth ascertained using the following formula:

$$\text{Film thickness (nm)} = \frac{1{,}000{,}000 \times \text{Mass Gained (g)}}{\text{Density (g/cm}^3\text{)} \times \text{Area (cm}^2\text{)}}$$

Spectroscopic reflectance was used to corroborate film thicknesses, with the aid of a Filmetrics F20 (380-1050nm) tabletop thin film analyser. This technique compares the wavelength of reflected light to the intensity, in order to ascertain qualities such as film thickness and refractive index.[49] As the light analysed is perpendicular to the substrate, polarization effects can be ignored, with spectroscopic reflection instruments being much cheaper and simpler to use overall.[50]

Samples were referenced to their respective substrate (e.g. Si wafer) to minimise background interference, and the FILMeasure software used to assess plotting techniques and error margins.

3.4.4 XPS

XPS is a useful tool to be able to use when looking to identify the structures present in a thin film. It is a surface sensitive technique that can indicate not only what atoms are present, but also what they are bonded to. Using the photoelectric effect, X-rays are directed at a sample, energizing electrons and resulting in their emission.[51,52] The kinetic energy of the electrons is then detected and plotted, and can be compared to other known values for structural determination.[53] The sampling depth of XPS is much deeper (5-10nm) than some other techniques used here, such as LEIS. Results obtained via XPS show a snapshot of the upper 5-10nm of the sample surface, whereas LEIS is sensitive to the outermost atomic layer.[44] In this project, the potential to identify the oxidation state of the iron atoms present, and hence exclude other iron oxide species as a result, is invaluable for film characterisation.[53,54] Unlike XRD this technique does not require the films to be in a crystalline form for analysis to occur. XPS was used in a limited capacity to confirm the presence of surface species on samples prepared on FTO glass due to the limitations of FTO with other techniques (XRD, Raman).

X-Ray Photon Spectroscopy was carried out by Dr Shamsal Haq of the Surface Science department, University of Liverpool using a Kratos Axis Supra XPS machine, with Cu k-α radiation.

3.4.5 SEM

SEM was used here to look at the surface structure of the hematite films. It operates by scanning the surface of the film, under vacuum, using an electron beam to bombard an area of the film surface.[55] As the electrons hit various atoms and scatter they get detected in the machine and the signal interpreted to produce an image of the surface under scrutiny. The machine used in these experiments was a Hitachi S3400 Variable Pressure Scanning Electron Microscope, with a 5.0kV electron acceleration voltage employed for the majority of measurements.

3.4.6 XRD

X-ray diffraction uses X-rays to determine atomic and molecular information of a crystal structure, often aiding in identification of chemical compounds. The X-rays are focused on to the crystalline sample and as the X-ray beam hits the atoms and electrons in the compound it will diffract at a given angle.[56,57] This is carried out over various angles for the sample and a diffraction pattern for the crystal can be built.[58] This diffraction pattern provides insight into the atomic arrangement of the crystal. For X-rays that interact with the sample surface, the angle of incidence, θ, will be the same as the scattering angle, θ, as defined by Bragg's law. When these waves are in phase, the wave interference is constructive and present as a high intensity peak on the spectrum.[59,60] In this project was used to help determine the chemical composition of the films, with a Smartlab Rigaku XRD (using a Cu wavelength) machine as the main XRD source.

3.4.7 Raman

Raman spectroscope differs from other spectroscopic techniques by its use of lasers to elucidate structural features of a material, including crystallinity, phase, polymorphy and chemical structure.[61] It is a light scattering technique, with each spectrum featuring peaks that result from specific molecular bond vibrations.[62] It is widely used due to its non-destructive nature. Raman spectroscopy was used to further elucidate structural information on the hematite samples and was carried using a Renishaw inVia confocal Raman microscope with a 532nm laser at 5% power. Experiments were carried out by J. Horne, as part of the Hardwick Group, SIRE, University of Liverpool.

3.4.8 Heat Treatments

The benefits of exposing samples produced on FTO substrates to heat were highlighted in Chapter 2, with the effects of heat exposure an ongoing question throughout this work. Ion migration and structural changes are common observations following exposure to heat, both of which will be assessed here.[40] Heat treatments were done in a Carbolite CTF12/65/550/301 single zone wire wound tube furnace in air. Treatments included a 2-hour anneal at 550ºC heat (Heat Treatment 1) and a shorter 20-minute heat step at 750ºC (Heat Treatment 2). Samples were removed following treatment and allowed to cool slowly to room temperature in air.

References

1 M. Leskelä and M. Ritala, *Thin Solid Films*, 2002, **409**, 138–146.

2 K. G. Upul Wijayantha, S. Saremi-Yarahmadi and L. M. Peter, *Phys. Chem. Chem. Phys.*, 2011, **13**, 5264–5270.

3 A. Devi, *Coord. Chem. Rev.*, 2013, **257**, 3332–3384.

4 G. N. Parsons, J. W. Elam, S. M. George, S. Haukka, H. Jeon, W. M. M. Kessels, M. Leskelä, P. Poodt, M. Ritala and S. M. Rossnagel, *J. Vac. Sci. Technol. A Vacuum, Surfaces, Film.*, 2013, **31**, 50818.

5 R. L. Puurunen, *Chem. Vap. Depos.*, 2014, **20**, 332–344.

6 R. L. Puurunen, in *invited tutorial at the International AVS Conference on Atomic Layer Deposition*, 2014.

7 J. A. Oke and T.-C. Jen, *J. Mater. Res. Technol.*

8 T. Kääriäinen, D. Cameron, M.-L. Kääriäinen and A. Sherman, *Atomic layer deposition: principles, characteristics, and nanotechnology applications*, John Wiley & Sons, 2013.

9 S. D. Elliott and J. C. Greer, *J. Mater. Chem.*, 2004, **14**, 3246–3250.

10 S. M. George, *Chem. Rev.*, 2009, **110**, 111–131.

11 R. G. Gordon, ed. C. S. Hwang, Springer US, Boston, MA, 2014, pp. 15–46.

12 W. M. M. K. M.F.J. Vos, A.J.M. Mackus, Atomic Layer Deposition Process Development – 10 steps to successfully develop, optimize and characterize ALD recipes., https://www.atomiclimits.com/2019/02/12/atomic-layer-deposition-

process-development-10-steps-to-successfully-develop-optimize-and-characterize-ald-recipes/.

13 M. Shahmohammadi, R. Mukherjee, C. Sukotjo, U. M. Diwekar and C. G. Takoudis, *Nanomaterials*, 2022, **12**, 831.

14 S. Tomer, J. Panigrahi, P. Pathi, G. Gupta and Vandana, *Mater. Today Proc.*, 2021, **46**, 5761–5765.

15 J. R. Schneider, J. G. Baker and S. F. Bent, *Adv. Mater. Interfaces*, 2020, **7**, 2000318.

16 J. R. Scheffe, A. Francés, D. M. King, X. Liang, B. A. Branch, A. S. Cavanagh, S. M. George and A. W. Weimer, *Thin Solid Films*, 2009, **517**, 1874–1879.

17 R. L. Puurunen, *Chem. Vap. Depos.*, 2005, **11**, 79–90.

18 M. E. Davis, *Nature*, 2002, **417**, 813–821.

19 M. Juppo, Helsingin yliopisto, 2001.

20 P. O. Oviroh, R. Akbarzadeh, D. Pan, R. A. M. Coetzee and T.-C. Jen, *Sci. Technol. Adv. Mater.*, 2019, **20**, 465–496.

21 J. Malm, T. Sajavaara and M. Karppinen, *Chem. Vap. Depos.*, 2012, **18**, 245–248.

22 J. Musschoot, Q. Xie, D. Deduytsche, S. Van den Berghe, R. L. Van Meirhaeghe and C. Detavernier, *Microelectron. Eng.*, 2009, **86**, 72–77.

23 D. Hiller, D. Tröger, M. Grube, D. König and T. Mikolajick, *J. Phys. D. Appl. Phys.*, 2021, **54**, 275304.

24 T. Weckman and K. Laasonen, *Phys. Chem. Chem. Phys.*, 2015, **17**, 17322–17334.

25 H. C. M. Knoops, J. W. Elam, J. A. Libera and W. M. M. Kessels, *Chem. Mater.*, 2011, **23**, 2381–2387.

26 K. Kukli, M. C. Dimri, A. Tamm, M. Kemell, T. Käämbre, M. Vehkamäki, M. Puttaswamy, R. Stern, I. Kuusik, A. Kikas, M. Tallarida, D. Schmeißer, M. Ritala and M. Leskelä, *ECS J. Solid State Sci. Technol.*, 2012, **2**, N45–N54.

27 M. Lie, H. Fjellvåg and A. Kjekshus, *Thin Solid Films*, 2005, **488**, 74–81.

28 A. Tamm, K. Kalam, H. Seemen, J. Kozlova, K. Kukli, J. Aarik, J. Link, R. Stern, S. Dueñas and H. Castán, *ACS omega*, 2017, **2**, 8836–8842.

29 A. Lale, E. Scheid, F. Cristiano, L. Datas, B. Reig, J. Launay and P. Temple-Boyer, *Thin Solid Films*, 2018, **666**, 20–27.

30 H. C. M. Knoops, E. Langereis, M. C. M. van de Sanden and W. M. M. Kessels, *J. Electrochem. Soc.*, 2010, **157**, G241.

31 H. Conrads and M. Schmidt, *Plasma Sources Sci. Technol.*, 2000, **9**, 441.

32 D. R. Boris, V. D. Wheeler, N. Nepal, S. B. Qadri, S. G. Walton and C. (Chip) R. Eddy, *J. Vac. Sci. Technol. A Vacuum, Surfaces, Film.*, 2020, **38**, 40801.

33 G. J. Van Rooij, V. P. Veremiyenko, W. J. Goedheer, B. De Groot, A. W. Kleyn, P. H. M. Smeets, T. W. Versloot, D. G. Whyte, R. Engeln and D. C. Schram, *Appl. Phys. Lett.*, 2007, **90**, 121501.

34 K. Arts, M. Utriainen, R. L. Puurunen, W. M. M. Kessels and H. C. M. Knoops, *J. Phys. Chem. C*, 2019, **123**, 27030–27035.

35 H. B. Profijt, S. E. Potts, M. C. M. Van de Sanden and W. M. M. Kessels, *J. Vac. Sci. Technol. A Vacuum, Surfaces, Film.*, 2011, **29**, 50801.

36 K. Arts, S. Deijkers, R. L. Puurunen, W. M. M. Kessels and H. C. M. Knoops, *J. Phys. Chem. C*, 2021, **125**, 8244–8252.

37 *Russ. J. Electrochem.*, 2002, **38**, 1364–1365.

38 X. Li, L. Zhao, J. Yu, X. Liu, X. Zhang, H. Liu and W. Zhou, *Nano-Micro Lett.*, , DOI:10.1007/s40820-020-00469-3.

39 P. Alulema-Pullupaxi, P. J. Espinoza-Montero, C. Sigcha-Pallo, R. Vargas, L. Fernandez, J. M. Peralta-Hernandez and J. L. Paz, *Chemosphere*, 2021, **281**, 130821.

40 D. A. Bellido-Aguilar, A. Tofanello, F. L. Souza, L. N. Furini and C. J. L. Constantino, *Thin Solid Films*, 2016, **604**, 28–39.

41 P. Qiu, H. Yang, L. Yang, Q. Wang and L. Ge, *Electrochim. Acta*, 2018, **266**, 431–440.

42 A. Hankin, F. E. Bedoya-Lora, J. C. Alexander, A. Regoutz and G. H. Kelsall, *J. Mater. Chem. A*, 2019, **7**, 26162–26176.

43 F. Bouhjar, L. Derbali, B. Marí and B. Bessaïs, *Sol. Energy Mater. Sol. Cells*, 2019, **195**, 241–249.

44 C. V Cushman, P. Brüner, J. Zakel, G. H. Major, B. M. Lunt, N. J. Smith, T. Grehl and M. R. Linford, *Anal. Methods*, 2016, **8**, 3419–3439.

45 H.-H. Perkampus, *UV-VIS Spectroscopy and its Applications*, Springer Science & Business Media, 2013.

46 K. M. Reddy, S. V Manorama and A. R. Reddy, *Mater. Chem. Phys.*, 2003, **78**, 239–245.

47 B. J. Berne and R. Pecora, *Dynamic light scattering: with applications to chemistry, biology, and physics*, Courier Corporation, 2000.

48 Y. Shimodaira, H. Kato, H. Kobayashi and A. Kudo, *Bull. Chem. Soc. Jpn.*, 2007, **80**, 885–893.

49 D. Nečas, I. Ohlídal, D. Franta, V. Čudek, M. Ohlídal, J. Vodák, L. Sládková, L. Zajíčková, M. Eliáš and F. Vižďa, *Thin Solid Films*, 2014, **571**, 573–578.

50 I. Ohlídal, *J. Mod. Opt.*, 1988, **35**, 1373–1381.

51 E. Paparazzo, *Surf. Interface Anal.*, 1988, **12**, 115–118.

52 J. D. Andrade, *Surf. Interfacial Asp. Biomed. Polym. Vol. 1 Surf. Chem. Phys.*, 1985, 105–195.

53 T. Radu, C. Iacovita, D. Benea and R. Turcu, *Appl. Surf. Sci.*, 2017, **405**, 337–343.

54 M. Liu, Y. Du, L. Ma, D. Jing and L. Guo, *Int. J. Hydrogen Energy*, 2012, **37**, 730–736.

55 J. I. Goldstein, D. E. Newbury, J. R. Michael, N. W. M. Ritchie, J. H. J. Scott and D. C. Joy, *Scanning electron microscopy and X-ray microanalysis*, Springer, 2017.

56 J. T. Jang, H. Ryu and W. J. Lee, *J. Alloys Compd.*, 2015, **638**, 387–392.

57 S. Krehula, G. Štefanić, K. Zadro, L. Kratofil Krehula, M. Marciuš and S. Musić, *J. Alloys Compd.*, 2012, **545**, 200–209.

58 C. Suryanarayana and M. G. Norton, *X-ray diffraction: a practical approach*, Springer Science & Business Media, 2013.

59 J. Epp, in *Materials characterization using nondestructive evaluation (NDE) methods*, Elsevier, 2016, pp. 81–124.

60 S. A. Speakman, *MIT Cent. Mater. Sci. Eng.*, 2014, **2**, 14.

61 A. Zwick and R. Carles, *Phys. Rev. B*, 1993, **48**, 6024.

62 O. N. Shebanova and P. Lazor, *J. Raman Spectrosc.*, 2003, **34**, 845–852.

Chapter 4: Plasma Enhanced Atomic Layer Deposition Of α-Fe_2O_3

4.1 Introduction

One of the key objectives for this PhD was to use atomic layer deposition (ALD) to produce hematite for use as a photoanode. This chapter looks at the methodology behind designing an ALD process, the outcome of this experimental work and the properties of the films that were produced.

4.2 Hematite: a problematic ALD candidate

As introduced in the literature section of Chapter 2, producing hematite by ALD is not a new concept, but can be a complicated one. A few of the common issues are:

- Low growth rates < 1Å,[1]
- Poor growth properties, such as low crystallinity or non-uniform growth,[2]
- Slow, inefficient ALD sequences, with dose times in excess of 30 seconds,[3]
- Use of expensive or volatile precursors; reducing commercial viability,[4]
- Excessive growth temperatures (>300ºC), that limit the use of photoactive substrates.[5]

In preparing for the ALD study the existing literature was relied upon to exclude some of the unsuccessful approaches and to guide the research direction, which will be seen in the upcoming sections.

4.2.1 Precursor Selection

Many existing Fe_2O_3 processes use precursors that are specifically produced to promote vapour pressure and achieve improved ALD growth.[6] If vapour pressure is low, surface saturation will not occur quickly or at all, hampering the growth of films. For many processes this means using transition metal alkyl complexes, with high volatility and weak metal-carbon bonds.[7,8] The ideal precursor should be thermally stable, as surface decomposition reduces self-limiting behaviour and increases impurities.[9] Conversely, it should not be so stable/non-volatile that it is unreactive to the co-reactant under ALD conditions.[10] It is a secondary benefit if the precursor is also: cheap, non-toxic, non-explosive, stable and easily stored.[8]

As science usually dictates, high reactivity usually coincides with a plethora of negative qualities, and thus it is a difficult balance to strike. Therefore, the best outcome is to use scientific techniques to boost the reactivity of 'poor' precursors to form a good ALD process. This PhD uses plasma technology to do just that. As covered in the 'Experimental Techniques' chapter, plasma enhanced ALD (PEALD) makes it possible to use less reactive precursors, as the radicals produced are very reactive. With PEALD it was possible to choose a cheap, stable precursor, ferrocene ($Fe(Cp)_2$), that exhibits low growth rates and requires temperature windows >350°C, to create a process with a reliable growth rate and reduced pulse-purge sequence than previously observed.[11]

4.2.2 Physical Precursor Adaptions

The initial issue with using $Fe(Cp)_2$ as a precursor was its inherently low vapour pressure (P_{vap}) at ambient temperature. With a vapour pressure of $P_{vap} = <0.98Pa$ at 298K,[12] ferrocene transport is virtually non-existent. In comparison trimethylaluminium, TMA, which requires no additional setup when added to an ALD reactor, has a vapour pressure of 1.2kPa at 293K.[13]

To overcome this problem, a vapour push bubbler was used to increase transport. This pushes a pre-specified amount of inert gas through the precursor pot and into the chamber, with the idea that the gas will carry precursor vapour into the ALD reactor chamber. With powder precursors, like ferrocene, this can be difficult as the powder itself can transport, ergo setting up the process requires some finesse. To increase the vapour pressure a heat jacket was added to heat the precursor powder to 80°C (353K). At this temperature, vapour increases to ~0.094kPa – almost a 100-fold improvement compared to room temperature.[14]

One factor that had to be taken into consideration was the sublimation of ferrocene. Under vacuum, with added heat, ferrocene is known to sublime readily.[15] As the original vessel was small, made of steel and with narrow inlet and outlet pipes, it was possible for this to occur in colder spots. To overcome this a custom bubbler was designed and fitted, with wider tubing to help prevent blockages, a lowered gas inlet to aid with the vapour push method and a glass body to make it easier to check powder levels and view any problems (Figure 14). Additionally, heating lines were added to the gas inlet pipes to reduce the possibility of cold areas and sublimation. This new setup removed early issues with the growth process and allowed the study to move forward unhindered.

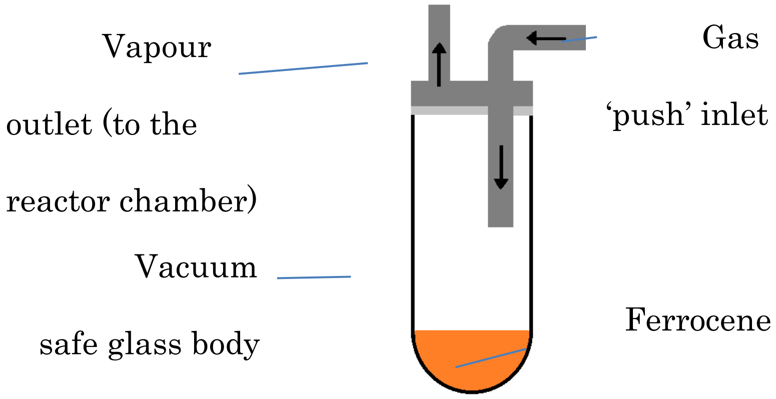

Figure 14: Custom built precursor 'bubbler' for ferrocene. 1/4" steel pipes make up the gas inlet and outlet, with glass body and rubber seal on steel cap.

4.3 PEALD Fe_2O_3 Growth Study

This section focuses on the specific parameters that required optimising to produce a smooth, effective, and reliable growth process.

4.3.1 Precursor Pulse Time

Logically, the first parameter that it is beneficial to establish in an ALD process are the sequence timings. Fortunately, a good starting point for the coreactant pulse-purge timings had been established based on multiple other processes ran on that specific reactor. As a result of this, a reasonable estimate for the O_2 plasma sequence could be used straight away – a 5 second pulse and 4 seconds purge sequence that was found to be sufficient for most processes.

Therefore, the earliest focus initially was to find the optimal pulse times for the ferrocene precursor. As this was the first parameter to be determined the general growth conditions were improvised for this set of experiments. An initial growth temperature of 200°C was chosen as it was on the low temperature end of similar growth processes.[5,16,17] Additional variables such as plasma power and plasma O_2 concentration were chosen based on generally good values for other processes used on the reactor, with the aim to test these at a later stage. The experiments were all done for 300 ALD cycles on (100) Si wafer as a constant. The first experiments used a 5s ferrocene pulse, which is typically rather long for an ALD pulse, to first confirm that growth occurred. Experiments were then carried out at decreasing intervals to determine if a trend was present, using an average calculated from the results. Further repeat experiments were then performed around a couple of values to check for anomalies in the growth pattern.

As covered in the Experimental Techniques chapter, there should be self-limiting behaviour to ALD processes. Figure 15 illustrates the self-limiting principle in this growth process, along with the results of the pulse time study.

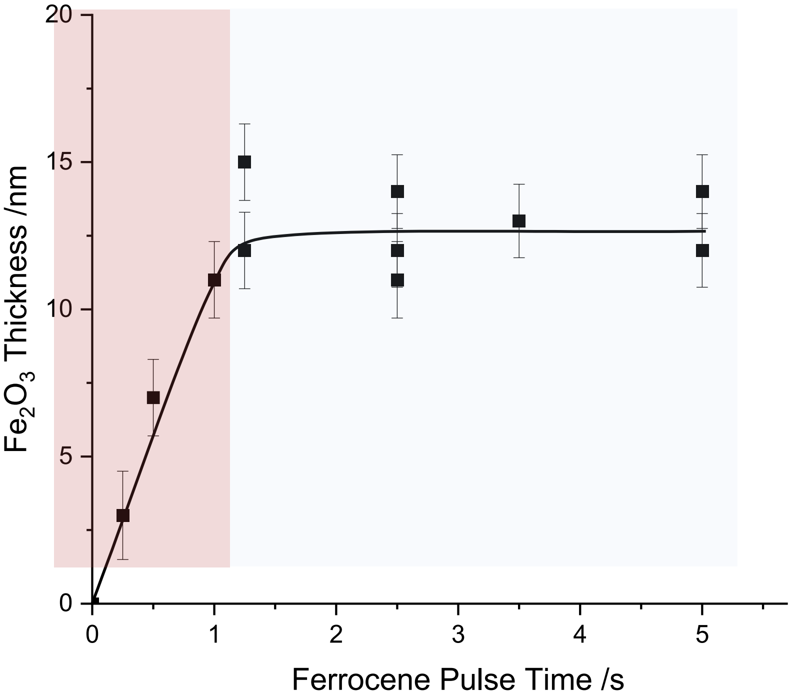

Figure 15: The relationship between the ferrocene precursor pulse time, the resulting thickness and self-limiting principle can all be seen within this graph. All experiments were carried out for 300 ALD cycles on Si wafers, using the weight gain method for thickness determination, and later checked with ellipsometry. The average of each of these experiments was plotted for this figure. Exponential growth followed by a plateau is the distinct pattern for self-limiting behaviour and acts as confirmation for the occurrence of a true ALD process.

The exponential growth stage, where the pulse time is not adequate to create a saturated surface, can be seen with pulse times below 1.5s (red section). Upon reaching this saturated level the growth evens out and at this point growth is said to be self-limiting (blue portion). This is demonstrated with the lack of additional growth with increasing pulse times; the extra precursor does not chemisorb to the surface and is instead purged away following the initial pulse.

Purge times were initially set at 8 seconds for these experiments, with an excessively high time better than too short of one. This was later cut down to 5s in a later experiment, as growth remained stable and did not increase (which would indicate insufficient purging). The final timings for this sequence were:

2-5-5-4 seconds

{$Fe(Cp)_2$ – Ar purge – O_2 plasma – Ar purge}

4.3.2 The role of temperature on Fe_2O_3 growth

As alluded to in the literature section, previous work in growing ALD hematite has seen mixed success over a range of temperatures. Using some of this work, an estimated range to test growth over was created, with 150-350°C balancing the limitations of the ALD reactor with the previous best temperatures found in other work. Having already discovered the optimal pulse sequence, this could be kept constant. Additionally, the number of cycles was held at 500 for each experiment, increasing from 300 in the previous study to help with accuracy in the thickness measurements. 500 cycles became the standard testing value for every subsequent experiment. The results were as follows:

Platform temperature /°C	**Total number of $Fe(cp)_2$ cycles**	**S1 Thickness /nm**	**S2 Thickness /nm**	**S3 Thickness /nm**	**Average thickness /nm**
150	500	21.9	21.8	21.9	21.9
200	500	24.5	24.6	24.5	24.6
250	500	25.2	25.2	25.1	25.2
300	500	25.1	25.2	25.1	25.1
350	500	25.2	25.1	25.2	25.2

Table 2: Data values for the temperature study. Three samples were made (S1, S2 and S3) and measured for each temperature and an average thickness calculated. All experiments were carried out on Si wafers, using the weight gain method for thickness determination, and later checked with ellipsometry.

The tabulated data indicates that a clear trend is present for the results, this is shown clearly in a chart (Figure 16).

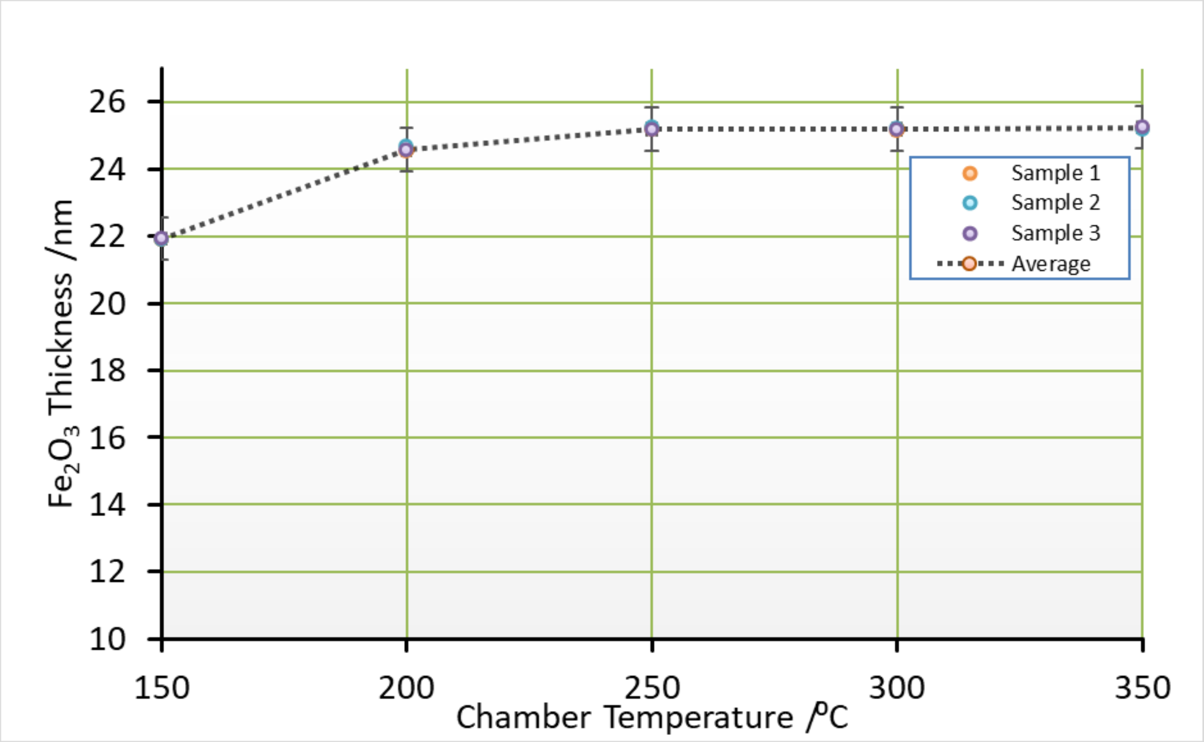

Figure 16: The trend between chamber temperature and resulting film thickness is easy to spot when plotted. There is a clear ideal growth temperature range (250-350ºC provide the highest level of growth), from which a set temperature for future experiments can be chosen.

In analysing the data, a possible range of ideal growth temperatures were found. The lowest value here was 250ºC, with additional temperature offering little improvement. Lower than this resulted in suboptimum growth, with 150ºC exhibiting a notable drop off. A lower growth temperature opens the door for a larger range of growth substrates for this process, as some common PEC substrates are temperature sensitive, therefore the lower value was chosen as default.

4.3.3 Varying plasmonic O_2 Concentration

Having set growth temperature at 250ºC, which was a little higher than the initial choice of 200ºC for {4.3.1}, going back and checking the plasma properties seemed necessary. A couple of experiments increasing the plasma time, to ensure it was sufficient, and increasing the O_2 plasma concentration were completed, and the results shown in Table 3.

Total number of $Fe(cp)_2$ cycles	O_2/Ar flow /sccm	O_2 Plasma Time /s	Average Fe_2O_3 Thickness /nm
500	20	5	25.2
500	40	5	25.3
500	20	10	24.4

Table 3: This data shows the relationship between plasma properties and resulting film thickness. Doubling the O_2 concentration yielded no real change for the films in question, nor did doubling the plasma duration. Plasma power was set at 200W.

It was found that increasing the concentration of the O_2 flowing through the lines of the plasma generator yielded no benefit for film growth, nor did doubling the plasma time. While it would have been possible to do a complete study as was done for the ferrocene, lowering the plasma time by a second or two was not deemed important enough to justify the heavy time commitment. As the film was growing consistently and a longer O_2 time did not show improvement in growth (5s was sufficient), further tweaks to plasma dose time did not offer substantial benefit and 5 seconds was chosen for all further sequences.

4.3.4 The effect of plasma power on Fe_2O_3 growth

An unexpected variable to check in this project was the power of the plasma generator. Shortly after completing the aforementioned experiments, it became known that the higher watt values on the plasma generator were associated with a chance of small specks of contaminants reaching the films. It was hypothesised that the high power of the plasma generator was sputtering material from the plasma walls onto the films during ALD processes. Plasma generators often carry this risk, though the literature suggests that hollow cathode generators produce species of >20eV energy, reducing the chance of etching on the cathode walls.[18] Though this phenomenon hadn't been witnessed for the samples in question, a further study was needed to ensure the films would grow sufficiently on a lower power plasma setting to reduce this possibility in the future. All previous experiments up until this point had been carried out with the default 200W plasma power value that was used for the reactor. The results are as shown in Table 4 and Figure 17.

Plasma Power /W	**Total number of $Fe(cp)_2$ cycles**	**S1 Thickness /nm**	**S2 Thickness /nm**	**S3 Thickness /nm**	**Average thickness /nm**
25	500	23.9	24.0	24.1	24.0
50	500	25.2	25.2	25.1	25.2
100	500	24.9	25.2	25.3	25.1
200	500	26.1	25.8	25.6	25.8

Table 4: The relationship between film thickness and plasma generator power. As can be seen there appears to be a limited relationship between the two variables.

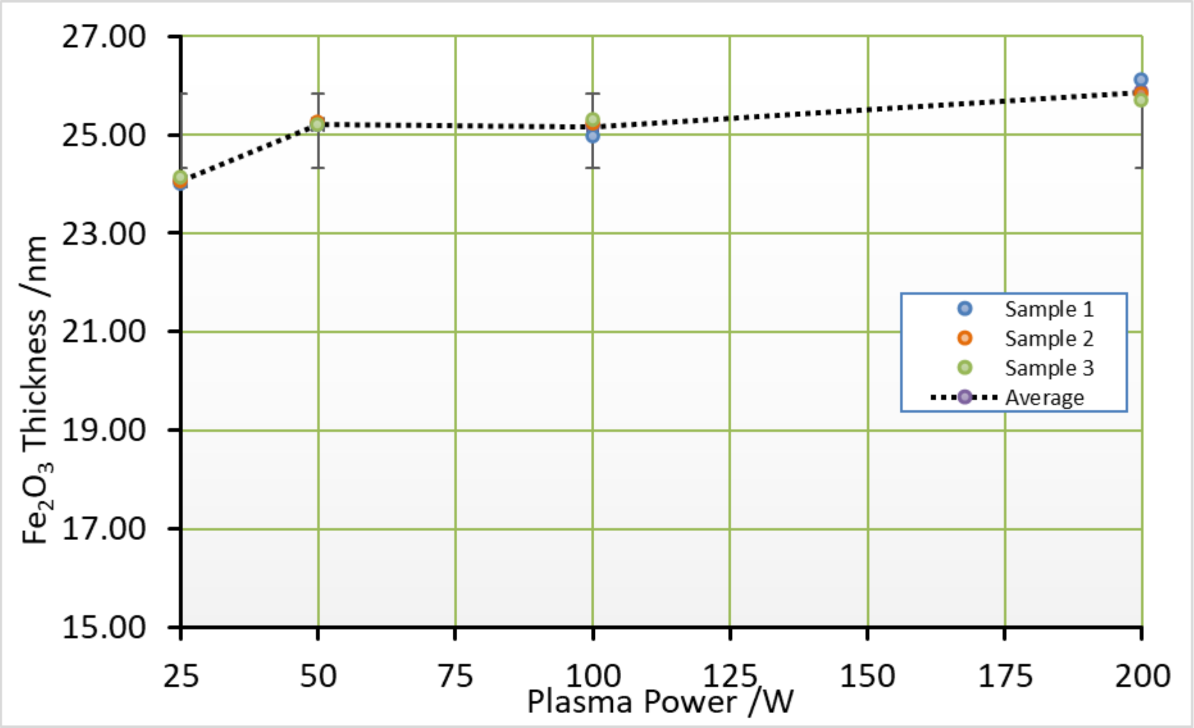

Figure 17: The relationship between the power setting of the plasma generator versus the resulting film thickness. Though it is clear there is a relationship between the two, it should be noted that the difference in values is not astoundingly high, therefore an elemental of judgement must be used when choosing the future power value.

There is a correlation between the power setting of the oxygen plasma and the resulting hematite film thickness. However, even with the large changes in wattage from 25W – 200W, the resulting film thickness change is confined to ~2nm at each extreme. Between 25W and 50W there is a slight increase, perhaps indicating that saturation had not yet occurred. Though there is an argument for using a 200W plasma setting based solely on growth, there is also a cost to benefit argument at play. For this reason, a 50W plasma power was chosen going forward. This had essentially the same growth as for 100W, with a thickness of ~25.2nm, and an improved growth than for 25W. Though there was a marked decrease of ~0.7nm from 200W to 50W, the reduced chance of impurities was weighted as more important, with film quality valued higher versus quantity in this case.

4.4 Linear ALD growth; expectation and results

In a standard ALD process, it possible to calculate a growth rate (GR) based on observed growth patterns. In determining the growth rate, experiments can be designed to create films of a specific thickness, down to the nanometre. This is done using the following simple calculations:

$$Growth\ rate_{\ (nm\ per\ cycle)} = \frac{Observed\ growth_{\ (nm)}}{Number\ of\ cycles}$$

$$Expected\ growth_{\ (nm)} = Growth\ rate_{\ (nm\ per\ cycle)} \times Number\ of\ cycles$$

Hence, creating a targeted film thickness is achievable if the rate at which the compound is growing is known. Using the data collected over numerous experiments, an average growth rate of **~0.05nm/cycle** was found for the ferrocene/O_2 plasma process.

For the electrochemistry side of the research it was required that films of a given thickness were produced, with a target film thickness of 118nm – the maximum light penetration depth of hematite.[19] To achieve this a total number of approximately 2400 cycles were needed, assuming a linear growth pattern and a GR of 0.05nm/cycle. The results obtained were not consistent with these assumptions (Figure 18).

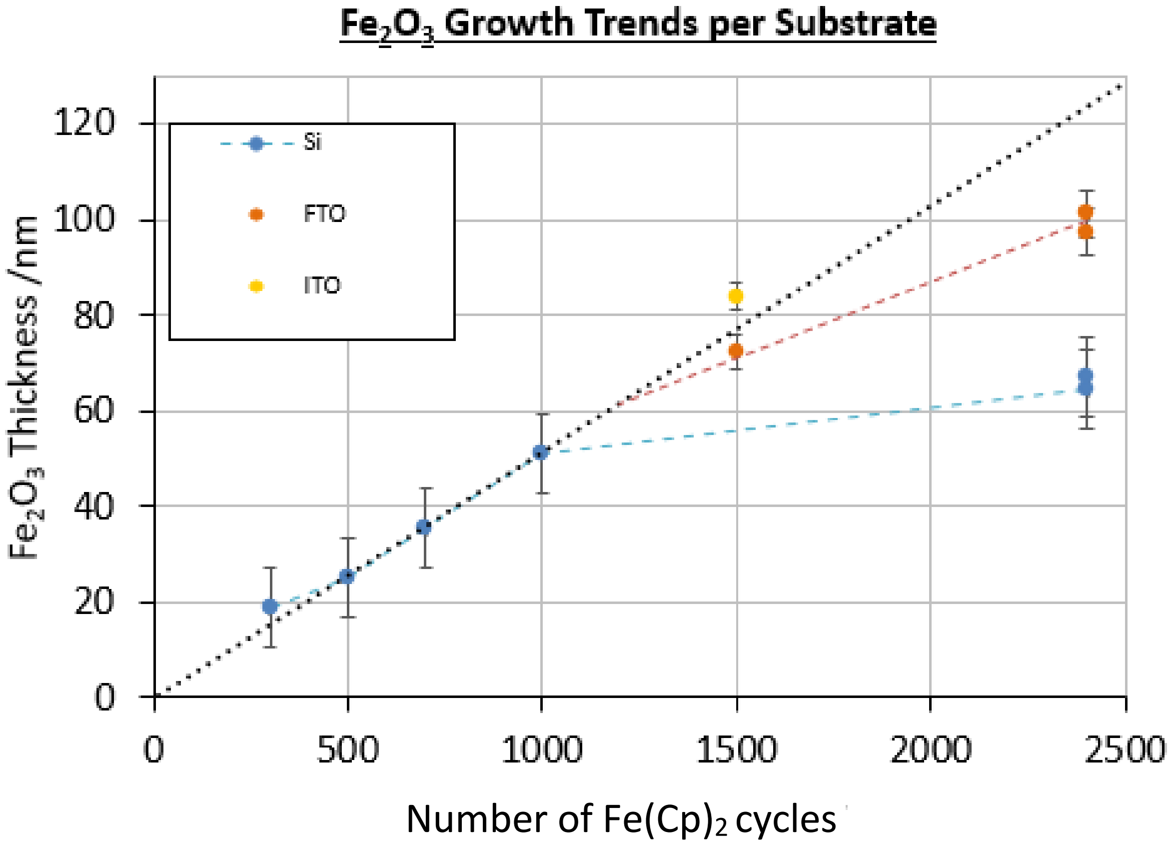

Figure 18: The results for actual growth achieved deviate from the expected (black dotted line) significantly. Changes in growth per substrate are also notable, with Si wafer showing increasingly hampered growth.

For any given ALD process, linear growth is the ideal to be aimed for. This standard implies that nucleation and growth are consistent in subsequent layers of compound and there are no drastic chemical changes occurring during longer processes.[20] Hence, the behaviour of growth does not change, and the growth rate is consistent throughout the process. Deviations from this can occur, with various types and causes of non-linear growth. In this instance, the plateauing of film thickness with increasing cycles is consistent with what is known as 'substrate-inhibited growth'.[21] This term refers to the change in properties with increasing substrate thickness. Here, layers of already deposited substrate act as an unfavourable surface for the precursor to chemisorb, to the extent that it inhibits continuous linear growth.[22] In this instance, this would mean that the hematite layer formed is less favourable for growth than the initial silicon/FTO surface. While this is not exceptionally common, this does occur with certain transition metal precursors. Particularly, this phenomenon has been noted with Fe precursors previously, in which Fe and C impurities stimulate the decomposition of the $Fe(Cp)_2$ itself, which is problematic for a compound rich in both iron and carbon.[16,23] This was hypothesised to be the likely cause of the limiting behaviour at higher deposition cycles.

An additional observation during this work was the notable growth preferences for certain substrates, with the iron oxide nucleation on glass-based enhanced compared to silicon. This can be seen with the thickness obtained following 2400 cycles, which was ~100nm for FTO or closer to 70nm on Si. Similar phenomena have been reported previously for iron oxide species grown on FTO and Si, with a few proposed reasons for the variation.[6,24] Taking into account the substrate differences, most notably the high aspect ratio of the FTO surface and terminal groups, the underlying growth mechanics would vary comparatively.[25] For instance, it has previously been noted that ferrocene show preference for high aspect ratio substrates, resulting in the desired conformal Fe_2O_3 growth.[26] It has been hypothesised that this was due to a preference for increased pore diameter, with the larger number of surface groups and reactive sites being favourable for the adherence of bulky ferrocene molecules.[27] Notably, this observation may raise concerns in a plasma driven process, due to the existence of recombination-limited growth (RLG). RLG can be a limiting factor for plasma processes, particularly with high-aspect ratio substrates, as the radicals need to exist for longer to travel into trenches and other formations, ensuring a conformal coating.[28,29] However, it is debatable whether FTO glass can be considered a substrate with a high enough aspect ratio to cause RLG. Yet it is sufficiently different to Si wafers, enough so to boost hematite growth in this work. Aside from the observations relating to substrate preference, the ALD process seemed to run smoothly and produce predictable growth patterns for use in this project.

4.5 Characterisation

4.5.1 X-Ray Diffraction (XRD)

4.5.1.1 Si Wafer Substrate

XRD experiments were carried out on both a high resolution 9kW Cu Smartlab Rigaku XRD and a Benchtop Cu Smartlab Rigaku XRD, with both short, quick experiments and longer, more focused runs. [Figure 19A, 19B].

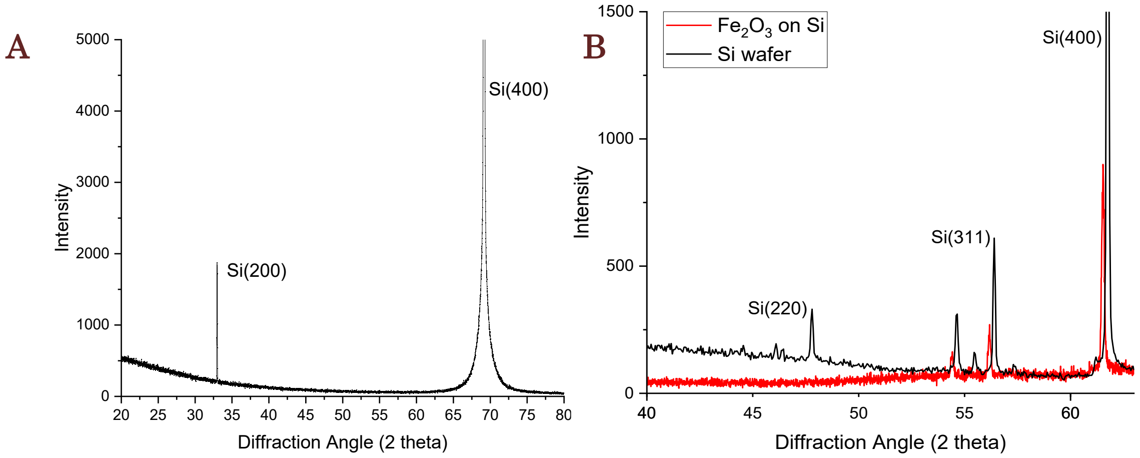

Figure 19A and 19B: XRD spectra for the samples in question. Both samples were heated to 750°C. **A** *- Approximately 64nm Fe_2O_3 on Si wafer, taken on a Smartlab Rigaku XRD using a Cu wavelength at*

298K. Present is the forbidden Si(200) peak and the large Si(400). B *– Bare Si(100) wafer vs 30nm Fe_2O_3 on Si(100) using a Smartlab Rigaku XRD. Multiple Si(100) peaks observable but no Fe peaks apparent (red).*

No peaks were detectable outside of those for Si(100) wafer on both instruments. The most common features found during these experiments were the Si(400), the forbidden Si(200) double diffraction peak at 33°, and occasionally some other minor Si peaks. [30,31] Annealing temperature had no effect on the diffraction pattern; the as-deposited samples showed the same Si peaks as those heated to 550°C and 750°C. Hence, it could be concluded that, at least for the Si substrate, the samples were amorphous.

Due to the extremely thin nature of the films under scrutiny, characterisation was a difficult task for the most part. The lack of peaks for these samples raised the question of whether the films are amorphous in nature, and require heat to crystallise, or whether this was a substrate specific issue (Si versus FTO).

The research on this subject indicated a few possibilities for these observations. One scenario is that of a Volmer-Weber, or 'island' type substrate growth, in which defects in the initial deposition layers create a mode for islands to form. With furthering deposition cycles these can grow and coalesce, creating amorphous or polycrystalline films.[32] This method of growth has been observed frequently for semi-conductors, particularly those with poorer growth rates at an intermediate temperature.[33]

4.5.1.2 FTO substrate

Following the results highlighted with XRD of the Si substrate, XRD of the FTO films was carried out. The films grew more readily on glass-based substrates, so it was hopeful that a 100nm film would show well defined peaks. However, the initial runs indicated that the baseline for FTO glass was incredibly noisy, and for a ~100nm film layer it was hard to discern clear hematite peaks [Figure 20].

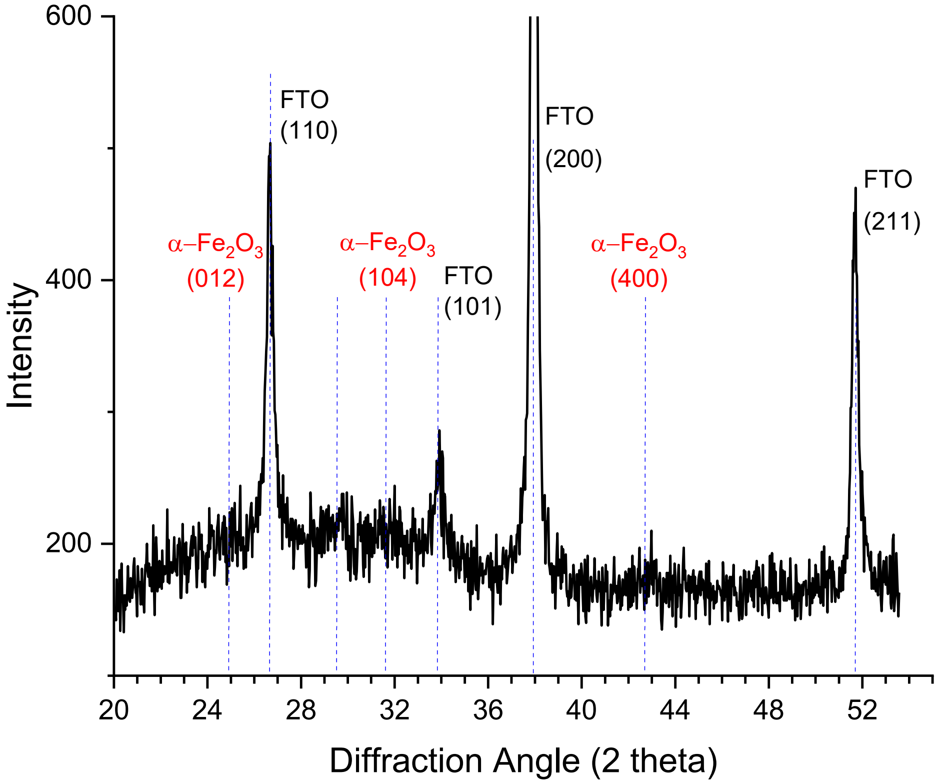

Figure 20: XRD spectra of Fe_2O_3 film on FTO glass shows an incredibly noisy baseline with broad FTO peaks. Baseline extrapolation tool (red line) indicates the possibility of hematite peaks within the noise, but this is arguable.

XRD for this sample is already problematic, as the main FTO peaks are broad and arise at the similar angles to some of the hematite peaks.[34] Additionally, as the glass deforms slightly at 750°, XRD here was unsuitable for these samples. However, in using a data baseline extrapolation tool on Origin software, potential peaks could be identified that may otherwise be hidden in the noisy baseline. Whilst this technique potentially alludes to the presence of some crystallinity within the samples, overall XRD was not useful for characterising the samples.

4.5.2 Raman Spectroscopy

One tool that could potentially shed further insight on the structure of the samples was Raman spectroscopy. Through collaboration with the Hardwick group at UOL, the opportunity presented itself to have a sample of the hematite heated and compared to an electrodeposited sample of hematite (>1 micron thick) using a Renishaw inVia confocal Raman microscope. This allowed a non-destructive way to view a sample pre and post heating. The heating was limited to 600°C at 30 minutes in air. Through Raman spectroscopy the clear difference between the as deposited and the post-anneal ALD samples could be seen [Figure 21A, 21B].

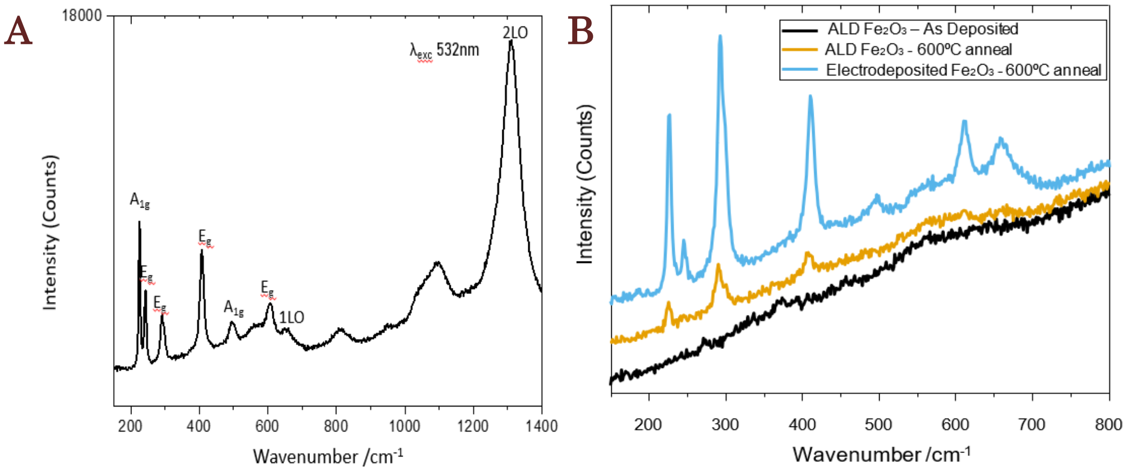

Figure 21A and 21B: Raman spectra for ~50nm Fe_2O_3 on FTO glass, taken using a 532nm laser at 5% power on a Renishaw inVia confocal Raman microscope. ***A*** *– Wide spectra view of annealed sample at 600°C for 30 minutes.* ***B*** *– Stacked view of an as deposited ALD sample (black), 600°C annealed ALD sample (yellow) and 600°C annealed electrodeposited hematite sample (blue) for comparison. Data collected by J. Horne, as part of the Hardwick Group, SIRE, University of Liverpool.*

Upon closer inspection, the various modes for hematite can be identified [Figure 21A]. This includes well known hematite modes such as the four oxygen vibrations at approximately 225, 245, 298 and 300cm^{-1}, as well as the three iron-based vibrations at 412, 496 and 610cm^{-1}.[35,36] The forbidden 1LO mode at 660cm^{-1} is also present, yet weak. Additionally, the intense 2LO at 1319cm^{-1} can be seen.[37] Furthermore, this technique fully confirms the identity of the iron oxide species as α-Fe_2O_3, as γ-Fe_2O_3 (maghemite) presents a large, broad A_{1g} Raman shift across 600-750cm^{-1} that hematite lacks and which is not present in these spectra.[38] The two-magnon scattering peak at 1320cm^{-1} is further confirmation of α-Fe_2O_3 as the sole iron oxide species here.[39]

Most notable for these samples is the difference following heating, with peaks that were previously broad and lost to the noise sharper and noticeable following the 600°C heat exposure. Contrary to the XRD, the noticeable difference in the Raman spectra pre- and post-heating indicates that the sample likely undergoes some structural changes with temperature, yet is amorphous when deposited. Thermally induced changes are not an uncommon occurrence for iron oxide specimens; oxidation and structural changes readily occur at elevated temperatures (usually to the more thermally stable hematite).[40,41] It is quite possible that in the deposited films Fe_2O_3 are amorphous in nature, but heat exposure induces structural change towards a more crystalline structure. This can be partially confirmed with appearance (Figure 22).

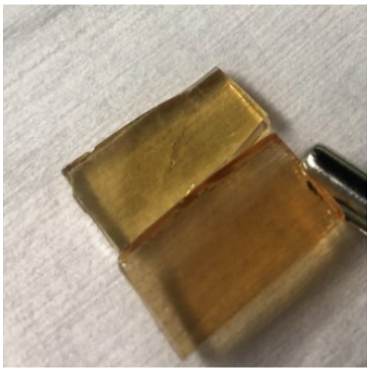

Figure 22: Picture of sample pre-anneal (left) and post-anneal (right). Colour changes from paler orange/yellow to deep orange can be observed following heat exposure of 550°C in air for 2 hours under normal atmospheric conditions.

Amorphous films exhibit slightly altered colours to their more crystalline counterparts, due to the different light scattering properties.[42] In particular, amorphous solids incoherently scatter light resulting in pale colour across the visible region. This may explain the paler colouration of the films pre-annealing and the deeper colour exhibited following temperature treatment.[43,44] An alternate explanation for this is that for temperature treatments over 400°C α-Fe_2O_3 (orange) is the preferential form of iron oxide, readily oxidising other iron species such as FeOOH, FeO, Fe_3O_4 and γ-Fe_2O_3. γ-Fe_2O_3 and FeOOH in particular are yellow in colour and commonly form while making hematite at lower temperatures. [45] This observation, along with the Raman data indicates that some degree of change occurs following heating, but does not indicate mechanism alone.

4.5.3 X-Ray Photoelectron Spectroscopy (XPS)

XPS was used to further confirm that the Fe species present was that of Fe(III), as expected in hematite for unheated films [Figure 23A, 23B].

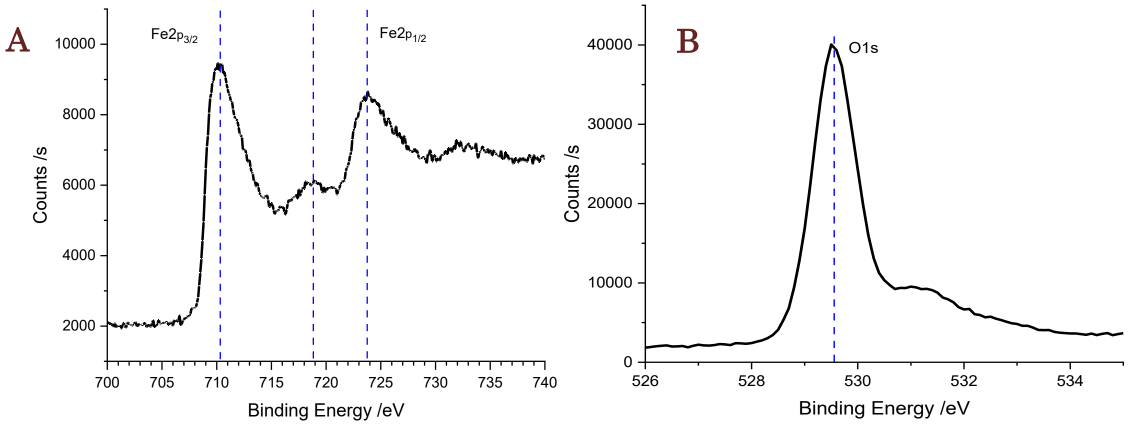

Figure 23A and 23B: XPS spectra for ~100nm unheated Fe_2O_3 film on FTO glass. Spectra obtained using a Kratos Axis Supra XPS machine. ***A*** *– Fe spectra shows $Fe2p_{3/2}$ peak at ~710eV, with secondary $Fe2p_{1/2}$ at ~723.8ev.* ***B*** *– Binding energy for O1s peak is ~529.6eV, with small shoulder peak present beyond 531eV.*

The Fe binding energies present are typical for that of hematite. Slightly higher $Fe2p_{3/2}$ and $Fe2p_{1/2}$ values of 710.2eV and 723.8eV (respectively) are characteristic of Fe_2O_3 and indicative of Fe(III) as the main species.[46] There is a distinct lack of a 715eV satellite peak, which would allude to the presence of an Fe(II) species.[47] Furthermore, the satellite peak at ~719.0 eV is not present for magnetite species (Fe_3O_4), but is a definitive feature of Fe_2O_3 films.[48] Similarly, the O_1s band occurs at 529.6eV here, in accordance with that of bare α-hematite.[49] The small shoulder peak present beyond the main O1s is a common feature of surface -OH species often present in metal oxide films.[50]

Overall, the XPS experiments show that the composition of the unheated iron oxide films is Fe_2O_3. This further analysis indicates that the colour changes observed are likely due to structural changes compared to changes in iron oxide species.

4.5.4 Scanning Electron Microscopy (SEM)

SEM was used here to observe if there were observable changes in the hematite appearance following heat exposure (Figure 24).

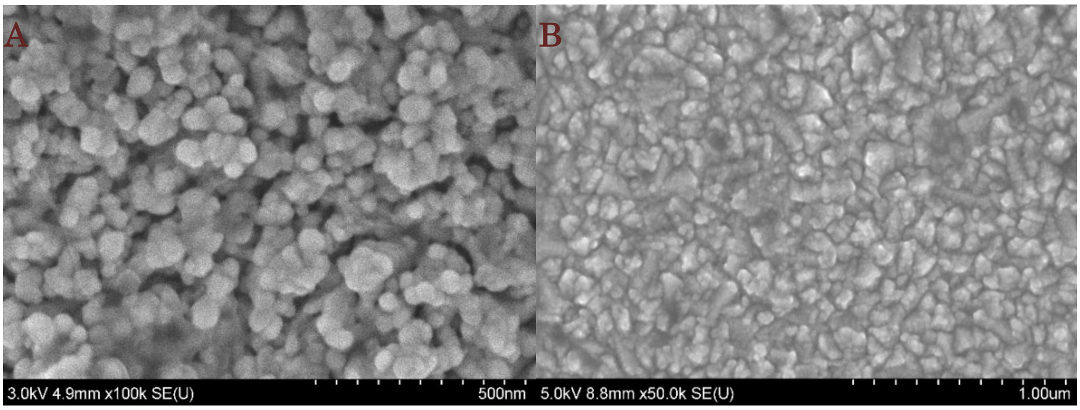

Figure 24: SEM of ALD Fe_2O_3 for A) As-deposited film at 100,000x and B) Heat treated film at 50,000x magnification on a Hitachi S3400., taken using a 5.0kV electron acceleration voltage.

Overall, structural changes are observable for the two films. The as-deposited films have large (500nm) clusters of hematite spheres, with a cauliflower-like structure observable. Following heat treatment these structures partially agglomerate, resulting in a lower degree of definition, with clearer boundaries between the clusters. This supports the observations made for Raman spectroscopy, where changes in the spectra could be seen following heat exposure. As XPS indicates that the as-deposited films are in fact hematite, then these observable changes must be due to an improvement in crystallinity.

4.6 Conclusion

To summarise, an ALD process that utilised a ferrocene precursor and oxygen plasma was created to produce thin hematite films for photoelectrochemistry. The process was revised and adapted in multiple steps to produce a reasonable 2-5-5-4s pulse purge sequence and 0.05nm/cycle growth rate. Some growth issues were encountered in relation to silicon substrates, though this should not affect the useability of the films, which require an FTO substrate for electrochemistry. Multiple techniques were employed to analyse the films, that were found to be amorphous upon deposition, but underwent changes with temperature. With the use of XPS and Raman the films were identified as the desired hematite, α-Fe_2O_3.

The upcoming chapters will now look at how the films performed for their intended purpose, as well as incorporating LEIS to further dive into the structure.

References

1 C. Du, M. Zhang, J.-W. Jang, Y. Liu, G.-Y. Liu and D. Wang, *J. Phys. Chem. C*, 2014, **118**, 17054–17059.

2 X. Meng, M. Ionescu, M. N. Banis, Y. Zhong, H. Liu, Y. Zhang, S. Sun, R. Li and X. Sun, *J. Nanoparticle Res.*, 2011, **13**, 1207–1218.

3 D. S. Jordan, C. J. Hull, J. M. Troiano, S. C. Riha, A. B. F. Martinson, K. M. Rosso and F. M. Geiger, *J. Phys. Chem. C*, 2013, **117**, 4040–4047.

4 Y. Lin, Y. Xu, M. T. Mayer, Z. I. Simpson, G. McMahon, S. Zhou and D. Wang, *J. Am. Chem. Soc.*, 2012, **134**, 5508–5511.

5 L. Steier, J. Luo, M. Schreier, M. T. Mayer, T. Sajavaara and M. Grätzel, *ACS Nano*, 2015, **9**, 11775–11783.

6 D. Peeters, A. Sadlo, K. Lowjaga, O. Mendoza Reyes, L. Wang, L. Mai, M. Gebhard, D. Rogalla, H.-W. Becker, I. Giner, G. Grundmeier, D. Mitoraj, M. Grafen, A. Ostendorf, R. Beranek and A. Devi, *Adv. Mater. Interfaces*, 2017, **4**, 1700155.

7 R. G. Gordon, ed. C. S. Hwang, Springer US, Boston, MA, 2014, pp. 15–46.

8 A. Devi, *Coord. Chem. Rev.*, 2013, **257**, 3332–3384.

9 M. A. Malik and P. O'brien, in *Chemical Vapour Deposition*, 2008, pp. 207–271.

10 M. Putkonen and L. Niinistö, *Precursor Chem. Adv. Mater.*, 2005, 125–145.

11 M. Rooth, A. Johansson, K. Kukli, J. Aarik, M. Boman and A. Hårsta,

Chem. Vap. Depos., 2008, **14**, 67–70.

12 Sigma Aldrich, Ferrocene Datasheet, https://www.sigmaaldrich.com/GB/en/sds/aldrich/f408, (accessed 20 May 2022).

13 Sigma Aldrich, TMA Datasheet, https://www.sigmaaldrich.com/GB/en/sds/aldrich/597775, (accessed 20 May 2022).

14 M. Fulem, K. Růžička, C. Červinka, M. A. A. Rocha, L. M. N. B. F. Santos and R. F. Berg, *J. Chem. Thermodyn.*, 2013, **57**, 530–540.

15 K. V Zherikova and S. P. Verevkin, *Fluid Phase Equilib.*, 2018, **472**, 196–203.

16 A. B. F. Martinson, M. J. DeVries, J. A. Libera, S. T. Christensen, J. T. Hupp, M. J. Pellin and J. W. Elam, *J. Phys. Chem. C*, 2011, **115**, 4333–4339.

17 M. Li and H. He, *Vacuum*, 2017, **143**, 371–379.

18 D. M. Goebel and I. Katz, *Fundamentals of electric propulsion: ion and Hall thrusters*, John Wiley & Sons, 2008.

19 J. Li and D. Chu, in *Woodhead Publishing in Materials*, eds. Z. Lin, M. Ye and M. B. T.-M. P. M. for E. Wang, Woodhead Publishing, 2018, pp. 49–78.

20 R. L. Puurunen, *Chem. Vap. Depos.*, 2004, **10**, 159–170.

21 O. Nilsen, C. E. Mohn, A. Kjekshus and H. Fjellvåg, *J. Appl. Phys.*, 2007, **102**, 24906.

22 R. L. Puurunen and W. Vandervorst, *J. Appl. Phys.*, 2004, **96**, 7686–7695.

23 C. A. Jones and D. P. Kelly, *J. Chem. Technol. Biotechnol. Biotechnol.*, 1983, **33**, 241–261.

24 M. Juppo, Helsingin yliopisto, 2001.

25 T. Arroval, L. Aarik, R. Rammula, V. Kruusla and J. Aarik, *Thin Solid Films*, 2016, **600**, 119–125.

26 S. Vahdatifar, Y. Mortazavi and A. A. Khodadadi, *J. Mater. Sci.*, 2020, **55**, 13634–13657.

27 P. P. Mameli, J. Schulpen, W. Roozeboom and F. Roozeboom, *J. Vacu Acuum Sci Technol A*, 2017, **10**, 4973350.

28 K. Arts, M. Utriainen, R. L. Puurunen, W. M. M. Kessels and H. C. M. Knoops, *J. Phys. Chem. C*, 2019, **123**, 27030–27035.

29 H. C. M. Knoops, E. Langereis, M. C. M. van de Sanden and W. M. M. Kessels, *J. Electrochem. Soc.*, 2010, **157**, G241.

30 A. Guiller, A.-G. Moussavou, M. Guilloux-Viry, A. Perrin, J. Fompeyrine, R. Sauleau and K. Mahdjoubi, *Ferroelectrics*, 2008, **362**, 95–104.

31 H.-Y. Chu, M.-H. Weng and C. Lin, *Int. J. Photoenergy*, 2013, **2013**, 245195.

32 M. Ritala, J. Niinisto, S. Krumdieck, P. Chalker, H. Aspinall, M. E. Pemble, W. L. Gladfelter, B. Leese, R. A. Fischer, H. Parala, R. Kanjolia, R. D. Dupuis, S. E. Alexandrov, S. J. C. Irvine, R. Palgrave, I. P. Parkin, A. C. Jones and M. L. Hitchman, *Chemical Vapour Deposition*, The Royal

Society of Chemistry, 2009.

33 M. L. Hitchman and K. F. Jensen, 1993.

34 Z. Landolsi, I. Ben Assaker, R. Chtourou and S. Ammar, *J. Mater. Sci. Mater. Electron.*, 2018, **29**, 8176–8187.

35 Y. Liu and R. D. L. Smith, *ACS Appl. Mater. Interfaces*, 2022, **14**, 6615–6624.

36 C. P. Marshall, W. J. B. Dufresne and C. J. Rufledt, *J. Raman Spectrosc.*, 2020, **51**, 1522–1529.

37 D. L. A. de Faria and F. N. Lopes, *Vib. Spectrosc.*, 2007, **45**, 117–121.

38 S. P. Schwaminger, P. Fraga‑García, F. Selbach, F. G. Hein, E. C. Fuß, R. Surya, H.‑C. Roth, S. A. Blank‑Shim, F. E. Wagner, S. Heissler and S. Berensmeier, *Adsorption*, 2017, **23**, 281–292.

39 J. H. Bang and K. S. Suslick, *J. Am. Chem. Soc.*, 2007, **129**, 2242–2243.

40 L. Machala, R. Zboril and A. Gedanken, *J. Phys. Chem. B*, 2007, **111**, 4003–4018.

41 O. N. Shebanova and P. Lazor, *J. Raman Spectrosc.*, 2003, **34**, 845–852.

42 A. Zwick and R. Carles, *Phys. Rev. B*, 1993, **48**, 6024.

43 F. J. Owens and J. Orosz, *Solid State Commun.*, 2006, **138**, 95–98.

44 K. Katagiri, Y. Tanaka, K. Uemura, K. Inumaru, T. Seki and Y. Takeoka, *NPG Asia Mater.*, 2017, **9**, e355–e355.

45 B. Pal and M. Sharon, *Thin Solid Films*, 2000, **379**, 83–88.

46 M. C. Biesinger, B. P. Payne, A. P. Grosvenor, L. W. M. Lau, A. R. Gerson and R. S. C. Smart, *Appl. Surf. Sci.*, 2011, **257**, 2717–2730.

47 A. Annamalai, A. Subramanian, U. Kang, H. Park, S. H. Choi and J. S. Jang, *J. Phys. Chem. C*, 2015, **119**, 3810–3817.

48 T. Radu, C. Iacovita, D. Benea and R. Turcu, *Appl. Surf. Sci.*, 2017, **405**, 337–343.

49 A. Bak, S. K. Choi and H. Park, *Bull. Korean Chem. Soc.*, 2015, **36**, 1487–1494.

50 T.-C. Lin, G. Seshadri and J. A. Kelber, *Appl. Surf. Sci.*, 1997, **119**, 83–92.

Chapter 5:
The Role of Underlayers

5.1 Introduction

The benefits of using ALD as a method of film production were highlighted in previous chapters. Specifically, the potential to build features into films with precise control over composition. This chapter will explore the results of adding an aluminium oxide underlayer to the films. An underlayer is a sheet of material placed on the electrode surface prior to adding the bulk material.[1] Aluminium oxide has previously shown promise as an overlayer, though is susceptible to degradation from the alkaline electrolyte.[2] There is some investigation of Al_2O_3 paired with other films (such as Si-Fe_2O_3 microwires) as a hematite underlayer, though no thorough exploration of this Al_2O_3/Fe_2O_3 pairing was found.[3] Hence there is room for exploration in this area, with a full study possible on the properties and effects of Al_2O_3 in this role. This work explores how Al_2O_3 underlayers impact the photoelectrochemical performance of α-Fe_2O_3 photoanodes. This study also explores how, in varying the film thickness, it is possible to tune the properties of the hematite thin films, with implications for both photocurrent and onset potential. Finally, the role of temperature exposure on these films is investigated, temperature treatments altering the performance of the films.

This chapter includes photo electrochemical results for the ALD produced hematite with and without underlayers. There is a dedicated analysis section for low energy ion scattering (LEIS), a brilliant technique for detailed structural analysis.

5.2 Electrochemical Performance of Films

5.2.1 PEC Cell Experimental

The core electrochemical setup for this work remained consistent throughout, as detailed in the ‘Experimental Techniques’ chapter. As a brief overview, a 1M NaOH (pH 13.6) electrolyte was used, with an Ag/AgCl reference and platinum counter electrodes. A 150 W Xe lamp (Newport 66902 Arc lamp) was used as a light source, with samples placed to achieve ca.100 mW.cm^{-2}, with dark currents taken in the absence of light. A PalmSens3 potentiostat was used for the readings, with 1cm^2 of the sample submerged in the electrolyte. In most instances, a linear sweep technique was employed from -0.4 V to 0.7 $V_{Ag/AgCl}$ with a 10 mV/s scan rate, starting just negative of the theoretical flat band potential for Fe_2O_3 and just beyond the dark current potential for water oxidation.[4,5] Repeat measurements were carried out for each experiment to ensure the results and setup were consistent with previous sessions, with the final measurement shown here. Dark currents were taken and monitored for changes, however these remained close to zero with little variation across samples (Figure 25B).

5.2.2 ALD Hematite Analysis and Discussion

5.2.2.1 Linear Sweep Voltammetry (LSV)

Early on it was important to establish a baseline for ALD hematite from which to compare any modified samples, this included samples modified by heat treatment. Additionally, discovering any novel properties of the sample was a priority. The experiment was done for both sides of the sample (front and back) to assess for a difference with illumination (Figure 26). The onset potential here was determined by extrapolating from the point of exponential photocurrent increase to the x-axis. An example of this is included in Figure 25A (dashed orange line). Different methods exist for determining onset potential; this method was chosen to account for the activity of all samples, with both steady and exponential gradient increases. The line was fitted to cover the majority of data points to ensure consistency among samples.

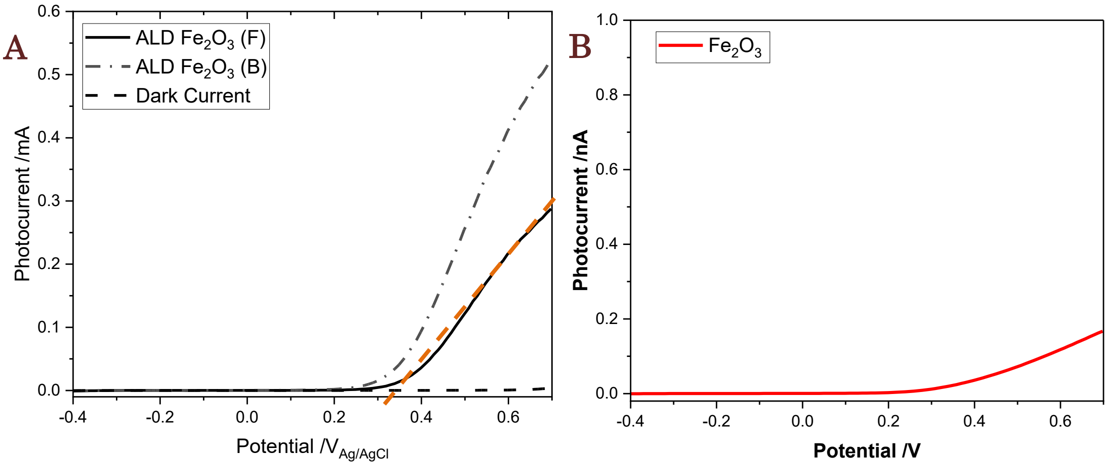

Figure 25: A) Photocurrent for ALD α-Fe2O3 with an estimated thickness of ~100nm. (F) Denotes illumination on the front side of the sample, (B) is illumination for the back (FTO) side of the sample. Dark current is shown with the dashed line. B) Zoomed in LSV of the dark current in nanoAmps.

The onset current for plain, as-deposited hematite on the front (hematite facing) side was ca. 0.34 $V_{Ag/AgCl}$, with a peak photocurrent at 0.7 V of 0.28 mA.cm^{-1} (Figure 25A). When illuminated from the back (FTO) side of the sample, there is a slight cathodic shift in onset (ca. 0.30 $V_{Ag/AgCl}$) and a much-improved photocurrent of 0.53mA.cm^{-2}. LSV in dark conditions showed a dark current onset similar to that of light, but peaking at 0.17 mA cm^{-2} at 0.7 $V_{Ag/AgCl}$ (Figure 25B). Placement of the samples was consistent for both illumination sides, with light intensity remaining constant (Ca 100mW cm^{-2}) as a result. This difference in orientation indicates that for this ALD sample there are altered effects between the semi-conductor/electrolyte and semi-conductor/electrode boundaries. For thin films grown on a transparent electrode such as these, a portion of the light can penetrate through the sample when illuminated from the rear side (Figure 26).

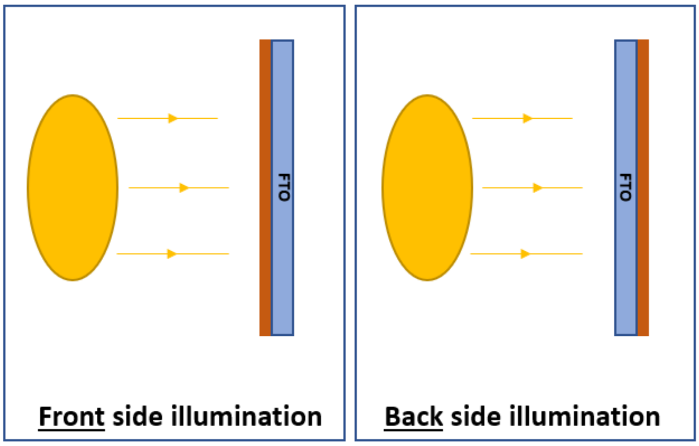

Figure 26: Experimental difference between front and back side illumination.

However, it is unlikely that similar levels of light reach the semiconductor liquid junction under back side illumination. As the reaction occurs at the semiconductor/electrolyte boundary, the front side (with highest illumination) should be the preferred orientation. Yet, there is a clear electrochemical improvement when illuminated from the electrode side. Lin et al. examined this pattern for $BiVO_4$ on FTO and found that this phenomenon occurs only for porous films, with standard films having no improvement with back illumination.[6] As porous films have cracks and holes between grains, it was hypothesised that the solution can enter and the reaction occur much closer to the electrode. As electron transport through the bulk structure is a known issue for hematite, this proximity to the electrode surface facilitates charge transfer compared to surface illumination.[7,8] In this case, the electrons are being produced closer to the electrode and can be swept into the circuit without needing to transfer through the bulk of the hematite.

This explanation is plausible for ALD hematite, as hematite can be difficult to grow via ALD. The existence of these holes in ALD iron oxide substrates has also previously been highlighted as an issue.[9] Scanning Electron Microscopy (SEM) of the samples confirm that the samples are highly textured, which adds credibility to this theory (Figure 27).

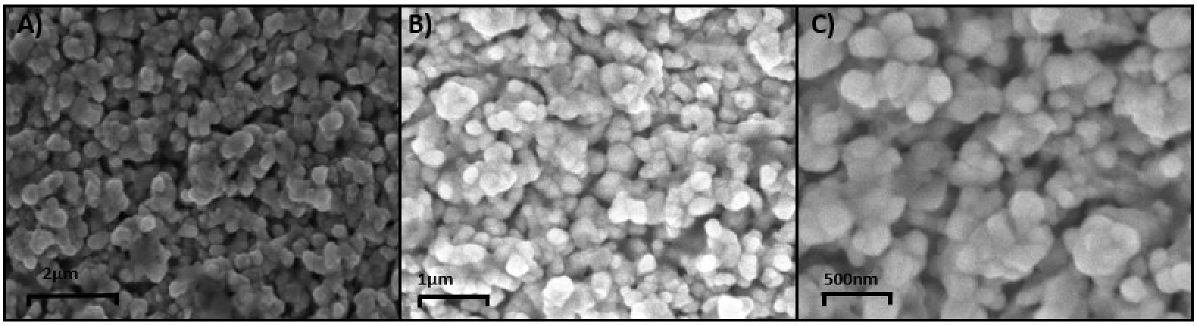

Figure 27: SEM of ALD Fe_2O_3 at A) 25,000x, B) 50,000x and C) 100,000x magnification on a Hitachi S3400. A taken using a 5.0kV electron acceleration voltage, B and C taken with 3.0kV acceleration voltage. Images show the presence of crevices in the hematite, with a spherical cluster like structure.

Under high magnification, the uneven surface is highlighted, with peaks and troughs visible across the sample. This corroborates the theory that the samples have areas where reaction can occur close to the electrode, improving the samples under rear illumination.

When looking to photoelectrochemical performance, the samples perform adequately, but not impressively compared to other hematite samples. Photocurrent densities in excess of 4 $mA.cm^{-2}$ have been reported for Ti-modified hematite, with an onset potential of 0.8 V_{RHE} for the same sample.[10] The following equation allows for the potential ($V_{Ag/AgCl}$) to be compared against the reversible hydrogen electrode (V_{RHE}):

$$E_{(RHE)} = E_{Ag/AgCl} + 0.059\ pH + E^0_{Ag/AgCl}$$

At pH 14, where $E^0_{Ag/AgCl} = 0.1976$, an onset of 0.34 $V_{Ag/AgCl}$ for this sample would equate to 1.36 V_{RHE}, above the desired 1.23 V_{RHE} for water-splitting. This is consistent with standard undoped, un-modified hematite, which has a poor onset potential exceeding the 1.23 V_{RHE} goal.[11] Though, the photocurrent for this sample of 0.53$mA.cm^{-2}$ is somewhat improved from similar thin films, where photocurrents are commonly below 0.5$mA.cm^{-2}$.[12] Nevertheless, there is lots of room for improvement with this sample, which is explored section 5.3.

5.2.2.2 Short-term Stability

Chronoamperometry was used to test the short-term stability of the samples in solution (Figure 28).

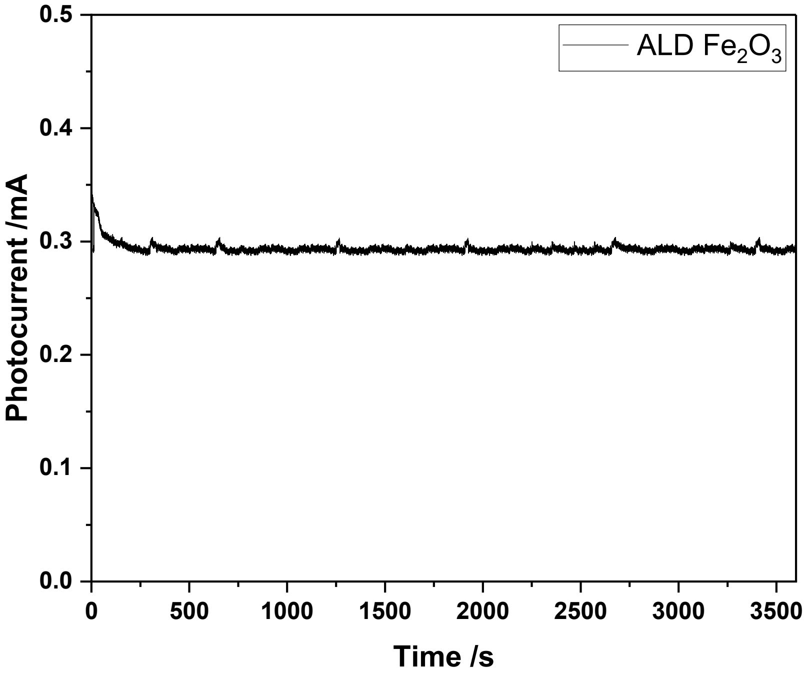

Figure 28: Chronoamperometry of α-Fe_2O_3 over a one-hour period held at 0.4V. Standard electrochemical setup was used, with the sample submerged in 1M NaOH and illuminated from the front side.

Over a one-hour period, no decrease in photocurrent was detected, indicating that the samples possess at least short-term stability in alkaline media. This is as expected, as hematite is incredibly stable under these conditions. Similar experiments on other thin-film hematite samples have shown over 1000 hours of constant photocurrent,[13] though no extended experiments were carried out in this project.

5.2.3 Effects of Heat Exposure

Hematite samples are often heat treated, as they show improved electrochemical properties following such treatment. The mechanism behind this improvement is often complicated or multi-faceted; heat treatments result in a range of improved qualities that positively impact performance. This can range from improved crystallinity, heat-driven doping from the electrode, changes in structure, the addition of oxygen vacancies, blending of grain boundaries – the list is long and reflects the specific samples at hand.[14,15]

As this project set out to explore the benefits of ALD grown α-Fe_2O_3, the standard heating parameters for the hydrothermal growth method were mimicked for this project. These heat treatments have been shown to be effective in boosting the performance of electrodeposited films, CVD and ALD films alike on FTO electrodes.[16,17] In doing so, it was possible to explore the benefits highlighted for other synthesis methods with these samples. As part of the synthesis, hydrothermal hematite samples require a 2-hour heat treatment at 550°C to ensure full oxidation of the iron species to Fe_2O_3.[18] This is often followed by a short, high-temperature heat treatment step to elucidate further improvement. The improvement following the high-temperature exposure has been attributed to Sn-doping of the hematite caused by diffusions of tin from the FTO electrode.[19] These steps offer similar benefits for ALD Fe_2O_3 in terms of oxidation.[20] In order to investigate how the two-step heat treatment affects the ALD grown hematite, samples were tested before any treatment, after a 550°C anneal in air for 2 hours ('Heat Treatment 1') and after a further heat treatment at 750°C for 20minutes ('Heat Treatment 2').

The results for unmodified ALD Fe_2O_3 are shown below (Figure 29, Table 5).

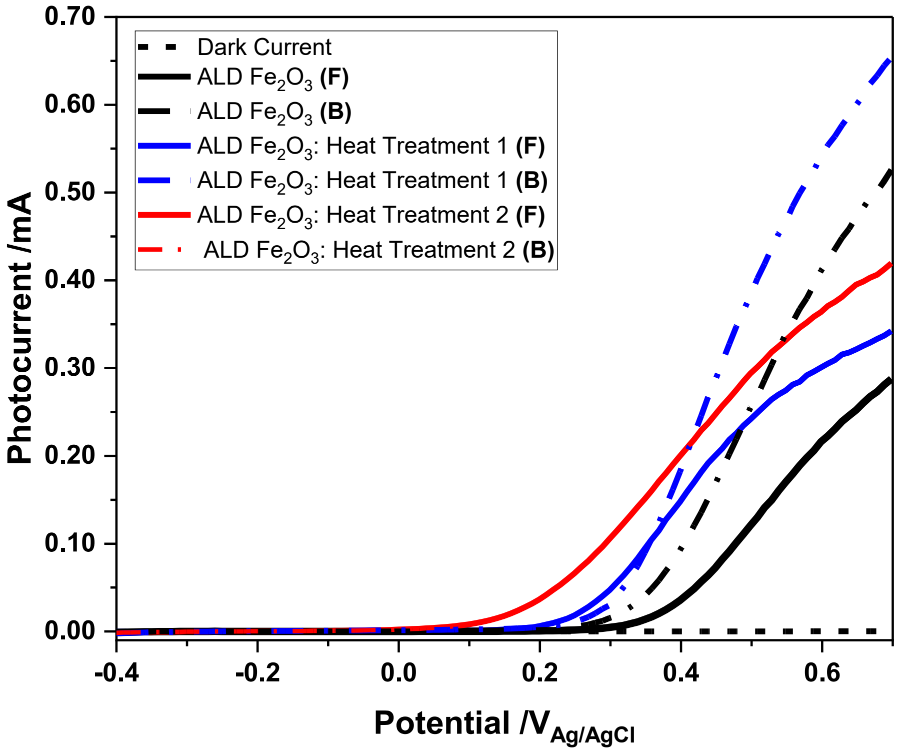

Figure 29: Comparison between ALD Fe_2O_3 as deposited, with additional heat treatment steps.

A two-pronged effect can be observed for these samples. Firstly, a cathodic shift in onset occurred with each heat treatment step, as well as an improved maximum photocurrent. Secondly, the favouring of back illumination ceased for Heat Treatment 2, with front side and back illumination showing the same response.

Sample	Onset /$V_{Ag/AgCl}$	Photocurrent at 0.7V /$mAcm^{-2}$
ALD Fe_2O_3	0.34 (F) 0.30 (B)	0.28 (F) 0.53 (B)
ALD Fe_2O_3: Heat Treatment 1	0.24 (F) 0.26 (B)	0.34 (F) 0.65 (B)
ALD Fe_2O_3: Heat Treatment 2	0.13 (F) 0.13 (B)	0.40(F) 0.40 (B)

Table 5: Summary of results for heat treatment on standard ALD hematite samples

Explanations for these trends are comparable to that expected for hydrothermal hematite on FTO glass. Heating at 550°C elucidates changes in the iron oxide species, oxidising any remaining Fe_xO_y species to the more photoactive α-Fe_2O_3, whilst also removing any remaining organic components.[21–23] The second heat step at 750°C is thought to move species from the FTO glass to the film, increasing charge carrier numbers, thus improving charge transport, in this case improving onset potential.[24]

The cessation of a favoured illumination side at 750°C is likely due to heat-induced changes in structure, creating a degree of agglomeration and reducing the number of troughs from previous levels. Heat Treatment 1, at 550°C, is not yet hot enough to cause serious deformation of the samples, as compared to the 750°C of Heat Treatment 2. As a result of this, a favouring of back side illumination can be seen up until the very high temperature anneal, when there is no difference between back or front illumination. Similar effects have been seen with other thin hematite films following high heat exposure, with temperature treatments decreasing porosity.[25,26] Hematite particle size also increases following high temperature treatments, further reducing the potential for reactions within the textured structure.[27–30]

These changes can be observed with SEM spectroscopy (Figure 30). As mentioned, the films have a degree of porosity wherein reactions can take place closer to the electrode surface. In annealing, agglomeration of the smaller particles occurs, in detriment to photocurrent and illumination effects.[31]

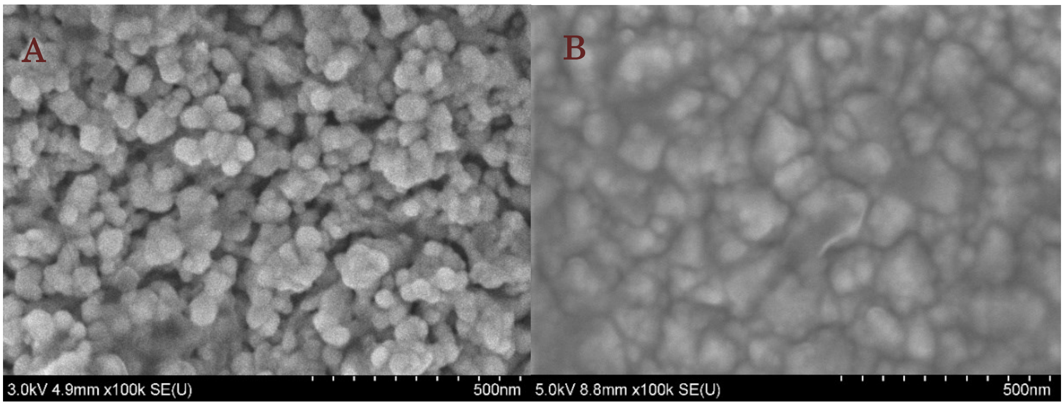

Figure 30: SEM of ALD Fe_2O_3 A) as-deposited and B) following Heat Treatment 2 – at 100,000x magnification on a Hitachi S3400 SEM.

The individual hematite particles are no longer obvious, with larger masses visible. Some deeper crevices can be seen, though these are from the FTO glass, with the ALD Fe_2O_3 forming a blanket surface layer across the topography.[27,28,32] Notably, particle size plays an important role in photoelectrolysis reactions, making these morphological changes important in the context of photoactivity. Specifically, larger particles offer greater charge separation, which is favourable for the OER. This separation facilitates the sweeping of electrons from the surface into the bulk, reducing recombination rates.[33–35] Conversely, it is also true that smaller particles allow for a greater degree of charge transport, which results in higher overall PEC photocurrents.[36,37] However, as hematite is defined by its poor charge transport abilities, smaller particles are considered more favourable in many cases, though recombination is also a factor to consider.[38,39] This duality highlights the balance that must be reached during the design of photoactive hematite films. This two-pronged effect can be observed in the films activity, with the smaller particles (prior to high temperature heating) yielding higher photocurrents overall and the larger masses following Heat Treatment 2 achieving improved onset potentials. The diminished recombination and increased charge separation for the larger particles reduces the potential required to generate a photoresponse in the film. Incidentally, it is also likely that the as-deposited films would suffer from increased trap states due to imperfections in the crystal structure.[40] These would differ from the heated films due to thermally-induced changes in the iron oxide film.[41] This explains the variation in photoresponse from the as-deposited samples to Heat Treatment 1 and 2.

UV-Vis Spectroscopy further highlights the alteration in samples, with an increased absorbance for the treated samples as compared to the unmodified hematite (Figure 31).

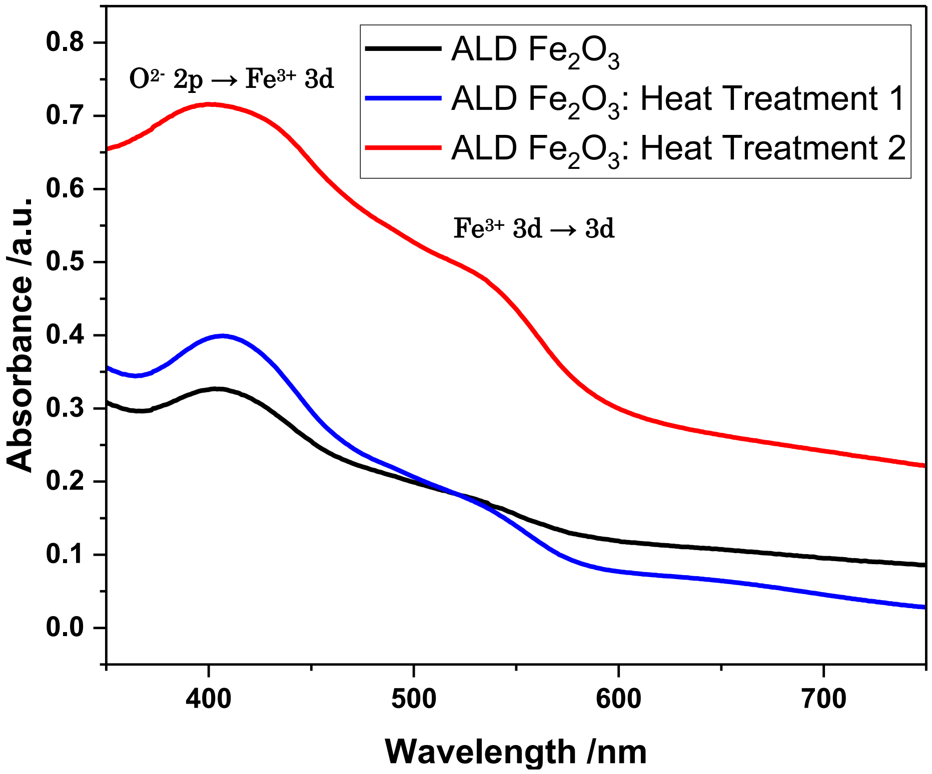

Figure 31: UV-Vis transmission spectra for ~120nm hematite samples taken using a Shimadzu UV-2600 spectrophotometer. Baseline was taken against cleaned FTO glass.

All samples show the typical hematite double shoulder shape, with the O^{2-} p to Fe^{3+} d transition hump at around 400nm and the Fe^{3+} d-d at 540nm.[42] No obvious red or blue shifts are observed for the samples. This stepped pattern with annealing temperature has been observed for hematite previously and is likely caused by changes to particle size. Rayleigh scattering occurs for particles that are smaller than the wavelength of the radiation; SEM indicates that individual particle size is below 500nm for these samples, with larger agglomerations visible.[43] Any changes to size here will affect the amount of scattering, with increased scattering lowering the amount of light reaching the detector, i.e.. showing an apparent increase in absorbance. Scattering increases for porous materials, due to the contrasts in refractive index of the pores to that of the film, while large particles also scatter more light than smaller ones.[44] While the data indicates that the as-deposited films are porous, the increase in particle size for the heat treated films accounts for the increased absorbance seen here. Additionally, the slightly broader peak seen following Heat Treatment 2 could indicate a larger range of particles sizes for these samples, increasing the wavelengths absorbed.[45]

5.3 Aluminium Oxide Underlayers

5.3.1 Aluminium Oxide

Aluminium oxide is an insulating metal oxide, with a bandgap of ~7 eV.[46] As an overlayer, Al_2O_3 has shown promise for reducing onset potentials and improving photocurrent through surface passivation effects.[47] Research to assess its role as an underlayer has been lighter, though highlighted some benefits, including lowered onsets for silicon/hematite microwires and improved photocurrents for iron titanate nanotubes.[3,48] The method of action behind these improvements varies across the research, though typically, Al_2O_3 is believed to improve charge transfer at the electrode interface via tunnelling and increased charge carriers.[49,50]

5.3.2 Experimental Method

Aluminium underlayers were added via PEALD prior to adding the hematite layers.* This was done within the ALD reactor in one continuous process, avoiding unnecessary contamination. A 25 ms pulse of trimethyl aluminium (TMA) precursor was followed by a 5 s oxygen plasma, with 5s argon purge in between each step, resulting in a 2.5ms-5s-5s-5s sequence. With a growth rate of ~1 Å per cycle, this sequence was repeated a set number of times to achieve the desired Al_2O_3 thickness. All other growing parameters (such as temperature) were held constant to facilitate hematite growth.

---

* Labelling Forenote

In the interest of reducing text clutter in legends, underlayers will be denoted with a (U) in figures. An example of this is:

ALD Fe_2O_3 + 0.3 nm Al_2O_3(U)

This indicates that the ALD hematite sample includes a 0.3 nm thick underlayer of aluminium oxide.

5.3.3 Electrochemical Results

The results of modifying the thickness of the Al_2O_3 underlayer with a consistent thickness of hematite were interesting. Without heat treatment, the samples with a thin underlayer mostly showed some improvement in both onset potential and photocurrent (Figure 32).

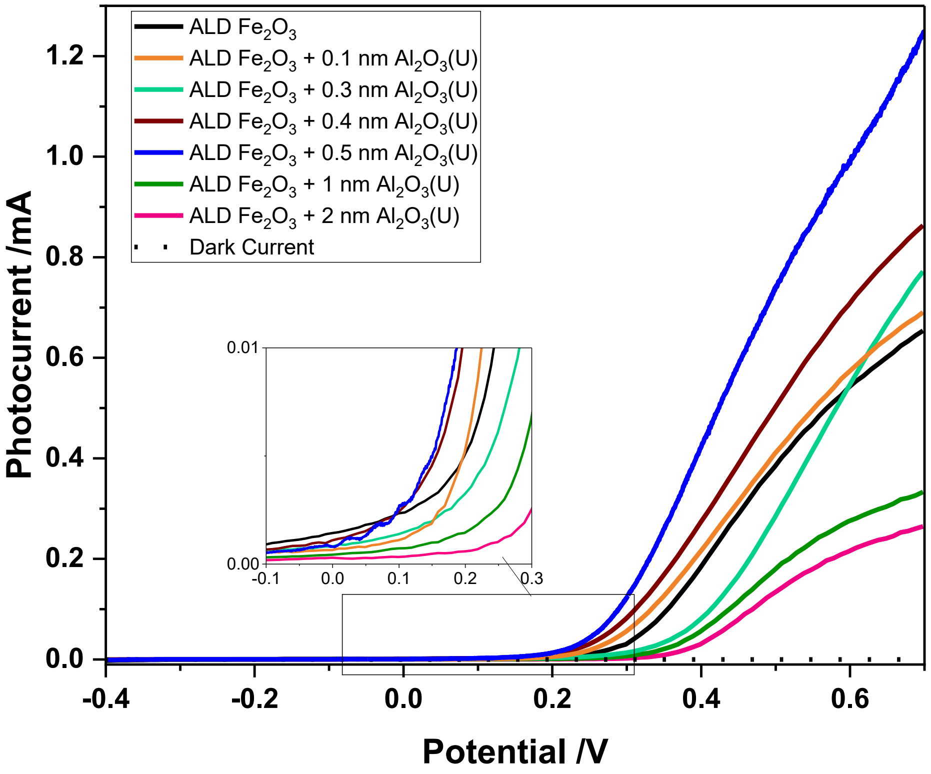

Figure 32: Comparison of ALD Fe_2O_3 sample (black), with additional underlayers ranging from 0.1 - 2nm in thickness, for unheated, as-deposited samples. All data is for backside illumination.

There was a generalised onset improvement with thin underlayers of Al_2O_3, which trailed off with thicker underlayers. The anomaly here was for the 0.3 nm underlayer, which presented with a slightly poorer onset than plain Fe_2O_3. However, in all instances below 0.5 nm, the thin Al_2O_3 underlayer improved photocurrent response at 0.7 V.

Exceeding 0.5 nm elicited the opposite effect, with dampened photocurrents compared to pristine ALD α-Fe_2O_3. Onset potential was also slightly anodically shifted, with a lowered photocurrent response overall. The trend for favouring backside illumination continued for all samples, indicating that the porosity of the films was not affected by the aluminium oxide underlayers.

5.3.4 Role of heat

As for pristine Fe_2O_3, heat played a significant role in improving the electrochemical properties of the films.

5.3.4.1 Heat treatment 1

Heat Treatment 1 improved all samples with an aluminium oxide underlayer (Figure 33). In contrast to the as-deposited samples, there was a step-wise improvement in onset potentials with increasing underlayer thickness up to 0.5nm. Similar to the previous samples, there was a favouring of the backside illumination. The thicker underlayers of 1nm and 2nm had comparable onsets and photocurrents, indicating that increasing thickness offers a capped benefit.

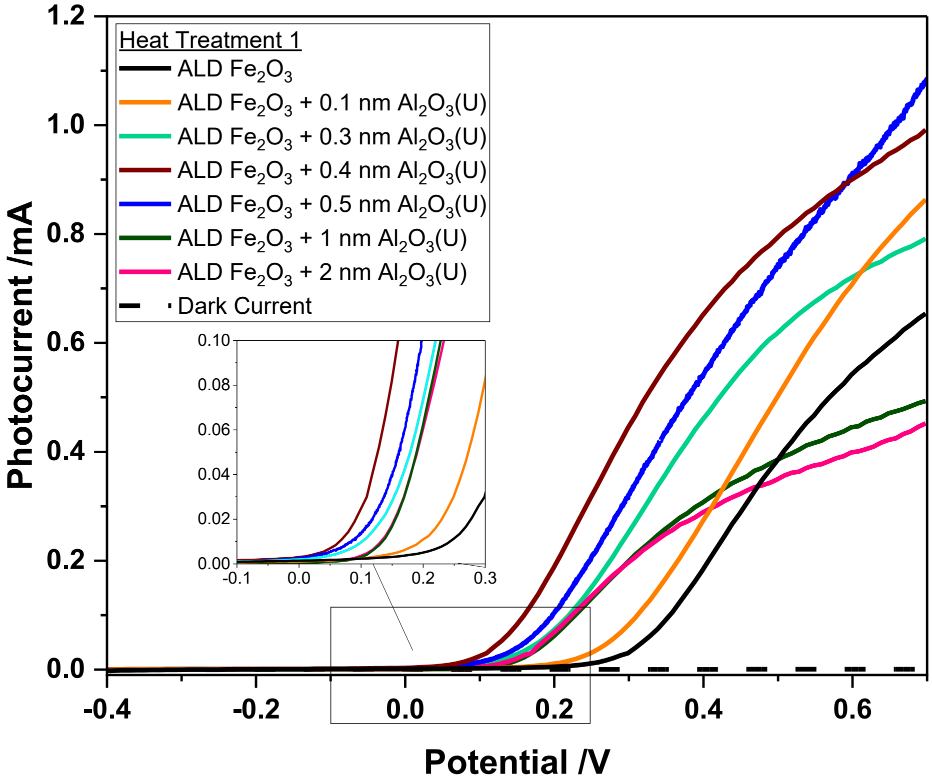

Figure 33: Comparison of ALD Fe_2O_3 sample (black), with additional underlayers ranging from 0.1 - 2nm in thickness, for samples undergoing Heat Treatment 1 (550°C for 2 hours in air). All data are for backside illumination.

A 550°C anneal step is not expected to be high enough for possible temperature-induced Sn doping. Yet this step has yielded an average cathodic shift in the onset of ~0.1 V across the samples with underlayers. Notably, there is little improvement in onset for pristine hematite, though photocurrent has increased by 0.12 mA.cm^{-2}. This indicates that though the 550°C temperature anneal benefits all samples to some degree, there is a distinct advantage for the hematite with an Al_2O_3 underlayer. Comparatively, following a 550°C temperature treatment, ALD Fe_2O_3 exhibits an onset potential of 0.26 $V_{Ag/AgCl}$ versus ~0.5 $V_{Ag/AgCl}$ for hydrothermal-Fe_2O_3, with photocurrents of 0.65 mA.cm^{-2}, to 0.075 mA.cm^{-2} respectively.[51] Charge transfer properties for undoped hematite annealed at 550ºC are notoriously poor, highlighting the improved carrier dynamics for the nanostructured ALD Fe_2O_3.

5.3.4.2 Heat Treatment 2

The final heat treatment step at 750ºC had antagonistic effects on the electrochemical performance of the samples. Each sample presented cathodically shifted onset potentials, indicating that the samples were active at a lower applied bias (Figure 34). Conversely, each sample also had reduced maximum photocurrent at 0.7 $V_{Ag/AgCl}$ when compared to Heat Treatment 1, with photocurrents returning to similar levels as the as-deposited samples. The exception here was the 0.5 nm underlayer sample, which experienced no drop off; the photocurrent at 0.7 $V_{Ag/AgCl}$ was 1.29 $mA.cm^{-2}$, compared to 1.09 $mA.cm^{-2}$ (Heat Treatment 1) and 1.25 $mA.cm^{-2}$ (as-deposited).

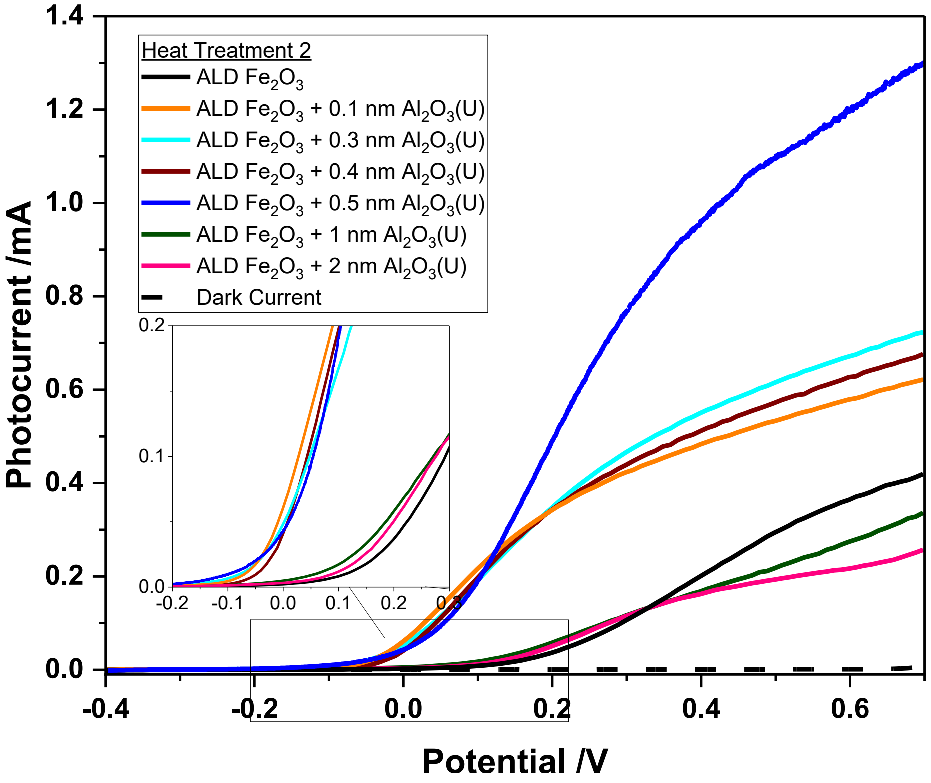

Figure 34: ALD Fe_2O_3 sample (black), with additional underlayers ranging from 0.1 -2nm in thickness, for samples undergoing Heat Treatment 2 (550°C for 2 hours, followed by 750°C for 20 minutes in air). All data sets are for backside illumination.

The photocurrent dampening effects of increased temperature likely coincide with the observation that there is no longer a preferred illumination side. As mentioned, the films have a degree of porosity wherein reactions can take place closer to the electrode surface. Annealing at the higher temperatures enable agglomeration of the smaller particles, in detriment to photocurrent and illumination effects.[31] This is confirmed via SEM (Figure 35).

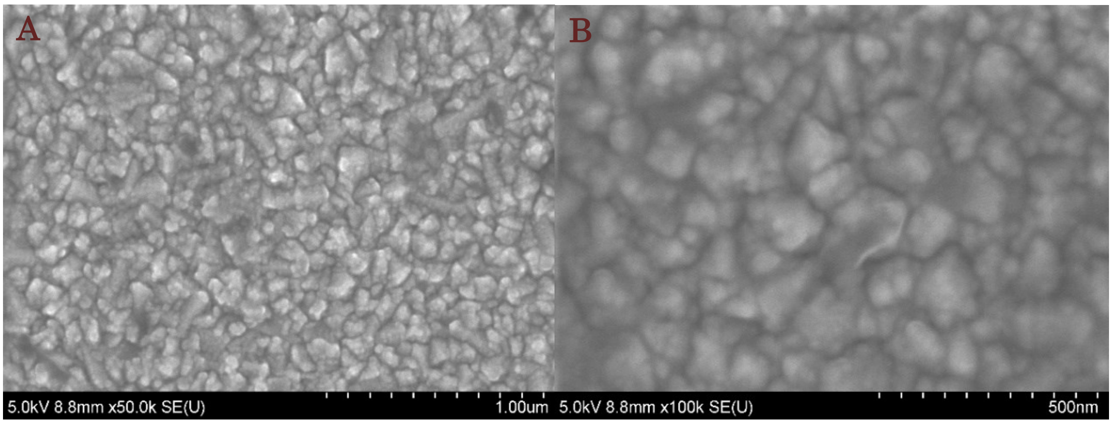

Figure 35: SEM of ALD Fe_2O_3 with Heat Treatment 2 at A) 50,000x and B) 100,000x magnification on a Hitachi S3400.

The individual hematite particles are no longer obvious, with larger masses visible. Crevices can be seen, with the ALD Fe_2O_3 forming a blanket surface layer across the topography.[27,28,32]

5.3.4.3 Overall Trends

The trends in onset and photocurrent across the different heat treatment parameters are outlined in Figure 36 and Figure 37.

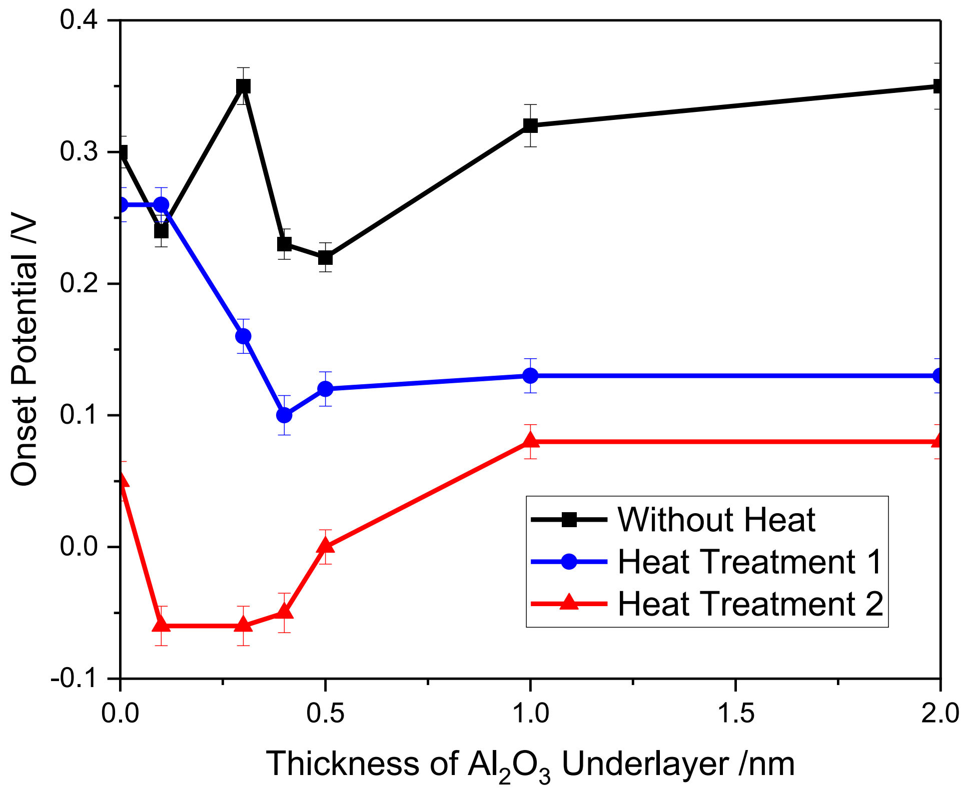

Figure 36: Onset potential plotted as a function of Al_2O_3 underlayer thickness across the three heat treatment parameters.

For onset potential there are two themes observed: the improvement in onset potential with subsequent heat treatments, and a looser trend in underlayer thickness. In general, thinner underlayers exhibited improved onset compared to the pristine sample, with underlayers >1nm exhibiting an improvement on the pristine sample following heat treatments. The heat treatment step appears to be the key for activating these films. This is seen to a lesser degree for photocurrent, where the trend with temperature is less clear (Figure 37).

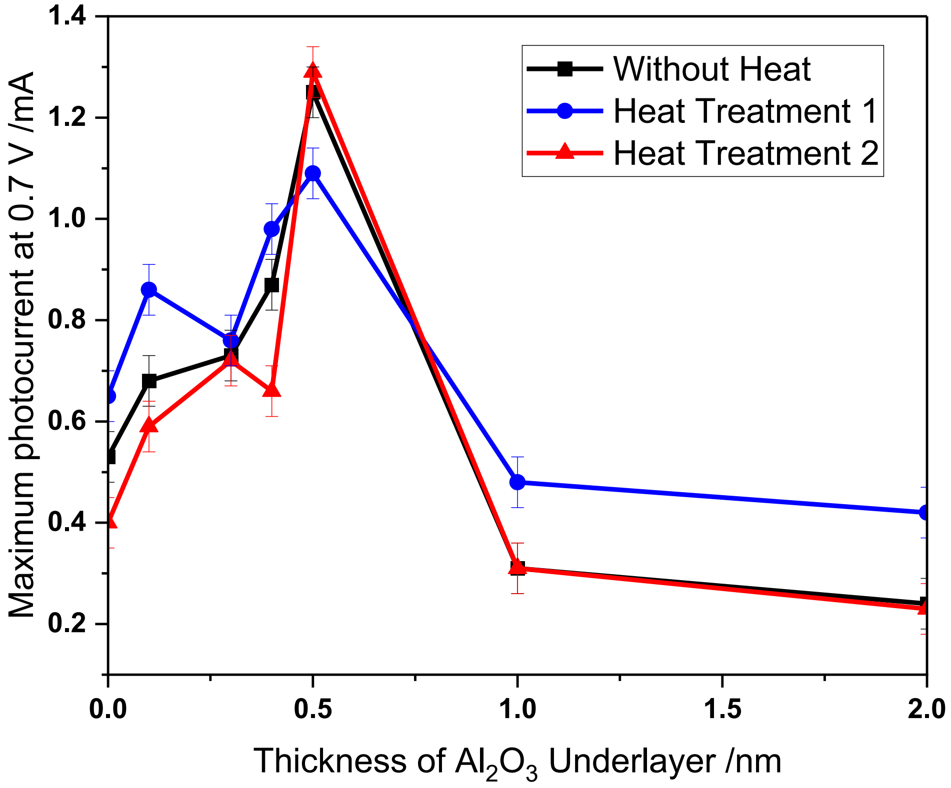

Figure 37: Maximum photocurrent exhibited (all at 0.7 V) plotted as a function of Al_2O_3 underlayer thickness across the three heat treatment parameters.

In this instance, thin underlayers offer a general improvement in photocurrent from the pristine sample, but have a clear drop off exceeding >0.5 nm Al_2O_3. While Heat Treatment 1 (at 550°C) results in a slight improvement for the thicker layers, Heat Treatment 2 reverses this. For the samples <0.5 nm Al_2O_3 there is a less consistent trend with heating, with Heat Treatment 1 appearing to offer a slight benefit over the pristine samples, which is removed once more following Heat Treatment 2.

Overall, the photoelectrochemical results for this study indicate that there is an advantage to the hematite photoanodes having thin Al_2O_3

underlayers, and the heat treatments further benefit this addition. The improvement in onset potential is especially intriguing, as onset potential is typically difficult to target for improvement.[52]

5.3.4.3 Chopped Photocurrents

Chopped photocurrents can be used to indicate levels of recombination within samples. For a typical semiconductor, there is a sharp increase in photocurrent following illumination that correlates to holes transferring to the electrode surface and electrons passing into the circuit.[53] This is the photoresponse expected for a photoactive n-type semiconductor. The subsequent decay in the absence of light is attributed to this build-up of holes, which causes an influx of electrons back to the surface following switch off, as shown with a negative current overshoot.[54] Hence, positive overshoots represent hole accumulation at the electrode–electrolyte interface, with negative overshoots indicating electron recombination. Logically, it is expected that the negative and positive overshoots would be equal in intensity, which is not often observed experimentally. In these samples an increased positive spike can be seen with a reduced negative spike. One explanation for this observation is that hole accumulation at the surface modifies the potential distribution across the space charge layer, a phenomenon known as band edge unpinning.[55] With this occurrence the band edges can move with applied potential and the build-up of holes occurs much faster than the recombination in the dark.[56] At higher potentials this reduces the width of the space charge region and eliminates negative overshoots. [57] It can be theorised that band edge unpinning is present in these samples to some degree, as there is a lack of symmetry in the transient features.

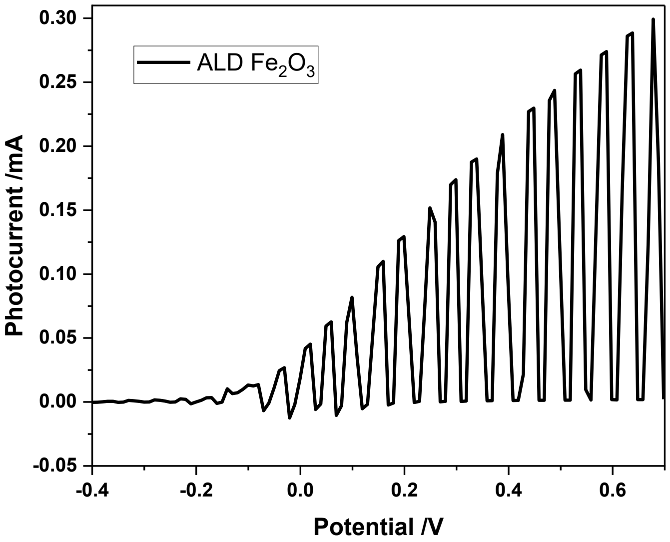

Figure 38: Chopped photocurrents for Pristine ALD Fe_2O_3 with Heat Treatment 2. Experimental parameters maintained for standard LSV, with the addition of light chopping.

For chopped currents taken with the usual 10mV/s sweep rate on the PalmSens3, there is low voltage to time resolution and any small current spikes are averaged out (Figure 38).

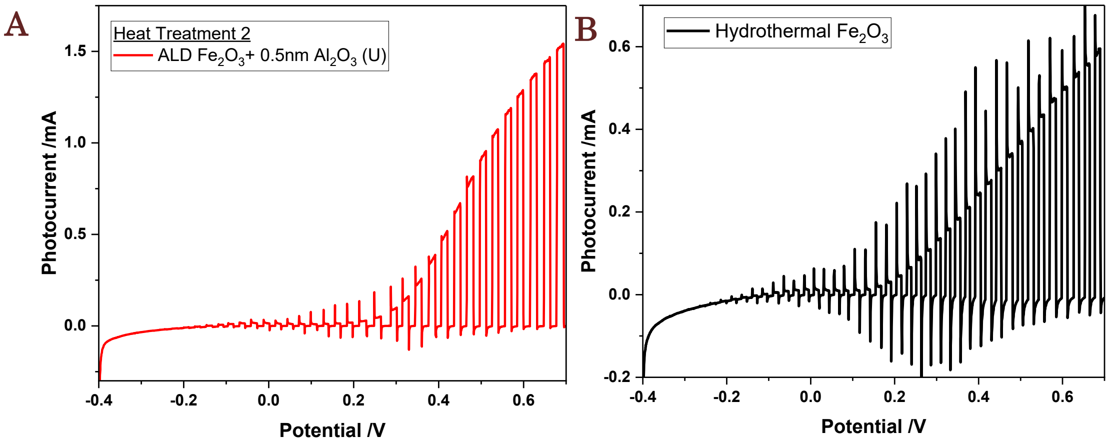

Figure 39: A) Chopped photocurrent for Fe_2O_3 with 0.5nm Al_2O_3 underlayer following Heat Treatment 2. B) Chopped photocurrent for hydrothermally produced α-Fe_2O_3 on modified FTO glass. Positive and negative overshoots indicate high hole accumulation and recombination rates. ALD sample thickness is estimated to be ~100nm, whereas hydrothermal sample is >1 micron thick.

When taken using a lower sweep rate (2 mV/s) on the BioLogic SP200 potentiostat, a much clearer can be seen (Figure 39: A) Chopped photocurrent for Fe2O3 with 0.5nm Al2O3 underlayer following Heat Treatment 2. B) Chopped photocurrent for hydrothermally $_{\text{produced}}$ α-Fe2O3 on modified FTO glass. Positive and negative overshoots indicate high hole accumulation and recombination rates). This observation signifies that the samples have reduced recombination rates, with little to no charge accumulation. This is furthered as the applied potential increases, with overshoots almost non-existent. This is expected for thin, nanostructured compounds, as band bending is limited by particle size.[54] As the applied potential increases, the accumulation ceases, indicating a theoretical limit has been reached and further accumulation is not occurring.[58] When compared to >1 μm hematite produced using the hydrothermal method, there is a clear difference (Figure 39B). The ALD samples exhibit reduced positive and negative overshoots compared to hydrothermal hematite, with almost no observable overshoots beyond 0.4 $V_{Ag/Ag/Cl}$. This reduced recombination provides a solid explanation for the samples exhibiting lower onsets and improved photocurrents compared to hydrothermally produced Fe_2O_3 under similar electrochemical conditions. Sample thickness is the defining quality between these two films. Hematite has poor charge transport properties and thicker films require the charge carriers to travel further through the bulk – this increases the chance of recombination occurring and reduces observable band edge effects.[59]

5.4 LEIS and Further Analysis

Low Energy Ion Scattering (LEIS) has been used in this project to monitor the surface composition and layers within the samples. This extremely surface sensitive technique enables any changes from sample heating to be monitored, offering insight into electrochemical properties. In order to observe all of the expected elements, a 3 keV He^+ analysis beam was used, with an oxygen plasma employed for removing surface hydrocarbon contaminants. A 1 keV Ar^+ sputter beam was used for the dynamic depth profiling measurements and the intensity of scattered He^+ was normalised to the ion beam current. This allowed the intensities of features observed in each spectrum to be compared. For this study, an ALD Fe_2O_3 sample with a 0.4 nm Al_2O_3 underlayer, a 5nm thick ALD Fe_2O_3 sample and an electrodeposited Fe_2O_3 sample (estimated thickness 150-200nm), all on FTO, were investigated.

5.4.1 LEIS of ALD Fe_2O_3 with 0.4 nm Al_2O_3 underlayer

For the ALD Fe_2O_3 with an Al_2O_3 underlayer, there are a few interesting observations when looking at the overall surface spectra of the samples.

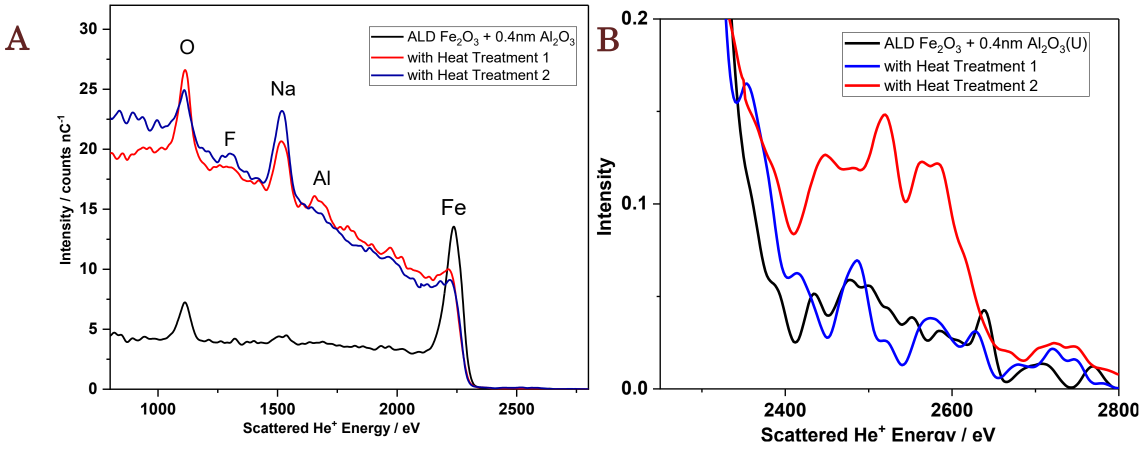

Figure 40: A) LEIS surface spectra for Fe_2O_3 sample with a 0.4nm Al_2O_3 underlayer. B) D) Highlights the change in Sn levels across all three heating conditions. LEIS experiment carried out by Dr Adrian Gardner, Stephenson Institute for Renewable Energy, University of Liverpool.

First, sodium (Na) is always present on the surface of samples, with high amounts detectable following heat treatment. Fluorine (F) is also visible following heat, but to a lesser degree - though this lowered amount may be partially due to the difficulties 'seeing' small F ions with LEIS. There are incremental amounts of aluminium (Al) at the surface with increasing heat. Finally, following the 750°C heat treatment step, tin (Sn) could be seen in small amounts at the surface.

Layered depth profiles for the same sample are shown below (Figure 41A-C). Dynamic depth profiling allows deeper aspects of the film to be analysed, with the use of sputtering to remove layers of material.

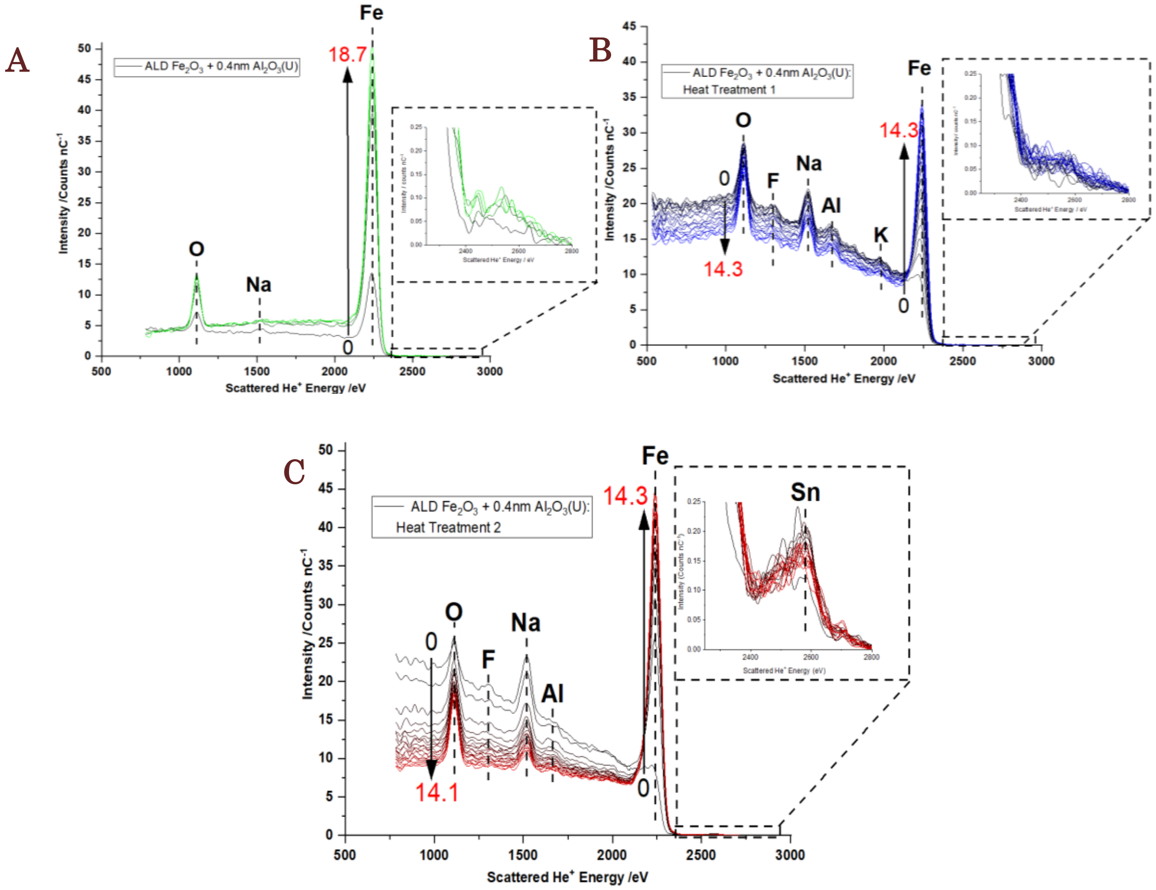

Figure 41; LEIS spectra over multiple layers for Fe_2O_3 samples with 0.4nm Al_2O_3 underlayer for A) as-deposited B) with Heat Treatment 1 and C) with Heat Treatment 2. Expanded windows zoom in on the Sn area of the LEIS spectra. LEIS experiment carried out by Dr Adrian Gardner, Stephenson Institute for Renewable Energy, University of Liverpool.

For the unheated sample, the depth profile is rather simple; Fe and O can be seen in large amounts, with a small Na peak and no Sn visible (Figure 41A). Following Heat Treatment 1, more labile ions are observed, with Na in greater amounts and K and F present in the top layers of the film (Figure 41B). Following Heat Treatment 2 there are fewer changes; a small Al peak can also be found here, with a constant amount in the upper layers. Interestingly, the presence of aluminium at the surface and just below it indicates that this has migrated from the thin underlayers following heat exposure. This will also be the case for F and Na, which will have migrated from the FTO and glass substrate respectively. An Al surface presence suggests that the underlayer could contribute more to the hematite than just improving interfacial charge transfer. Previous studies have highlighted that hydrothermal hematite with Al_2O_3 underlayers had lower recombination in the bulk, as well reduced recombination at the surface and interface.[60] LEIS studies here observed that, following heat treatment, Al does not remain solely as an underlayer, which would explain these previous observations that surface recombination is lowered. Al doping has been shown to result in lowered flatband potentials for hematite, with lower flatband potentials having a synergistic effect on onset.[61,62] This explains the lowered onset trends for the samples with underlayers, as the Al moves from just an underlayer, to dopant throughout the sample and at the surface.

Additionally, the sample following Heat Treatment 2 has a small Sn peak visible, with an intensity of $> 0.2nC^{-1}$, and a sharp peak indicating that Sn is found at the surface for this sample.[63] As Sn is a large ion, it is much easier to detect using LEIS than smaller ions such as Na and F.[64] As FTO deforms with high heat, it is possible that the Sn here is seen through a fissure in the sample, though Sn migration is also a consideration. Heat treatments exceeding 700°C are often carried out to induce Sn doping from the FTO substrate, which at least partially aligns with the observations here.[65]

The improvement seen following high heat exposure is often prescribed to temperature-induced Sn migration for FTO/ITO based photoanodes.[66] The photoelectrochemical results observed here indicate that there is a general improvement in onset potential following heat treatment, though the LEIS results show no Sn present for Heat Treatment 1, and only minimal amounts for Heat Treatment 2. While Heat Treatment 1 is not hot enough to induce Sn migration, there is still an improvement in onset and photocurrent for the samples. By comparing with other hematite thin films on FTO, a stronger understanding of the underlying mechanism can be derived. Dynamic depth profiling of electrodeposited hematite was carried out to determine whether the Sn migration seen for the ALD samples aligns with other hematite production methods.

5.4.2 LEIS of Electrodeposited Fe_2O_3

Depth profiles of the electrodeposited Fe_2O_3 on FTO (with Heat Treatment 2, estimated thickness ~150-200 nm), show a sharp Sn peak, compared to the ALD samples (Figure 42).

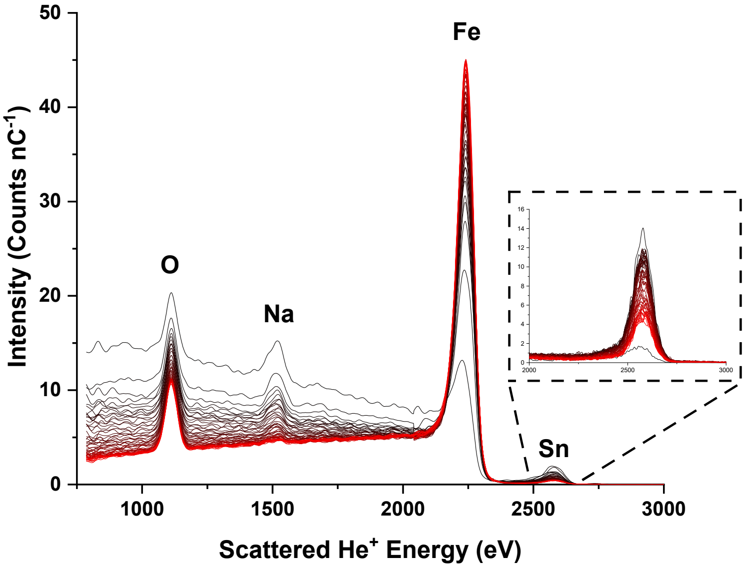

Figure 42: LEIS profile for electrodeposited Fe_2O_3 on FTO following Heat Treatment 2, produced by Dr SocMan Ho-Kimura (Institute of Applied Physics and Materials Engineering, University of Macau). LEIS experiment carried out by Dr Adrian Gardner, Stephenson Institute for Renewable Energy, University of Liverpool.

The intensity of the Sn peak here is ~14 nC^{-1}, compared to an intensity of ~0.15 nC^{-1} for the ALD sample. This is observed for a layer much thicker than the samples in this project, indicating that Sn migration occurs readily for some films. This observation may indicate that Sn movement is suppressed in the ALD-Fe_2O_3 samples; though this would need further study to confirm.

5.4.3 LEIS of 5nm ALD Fe_2O_3

Finally, a 5nm ALD-Fe_2O_3 sample was also tested to compare the surface composition of extremely thin hematite films (Figure 43). This was carried out as a reference sample for comparing the intensity of the surface peaks.

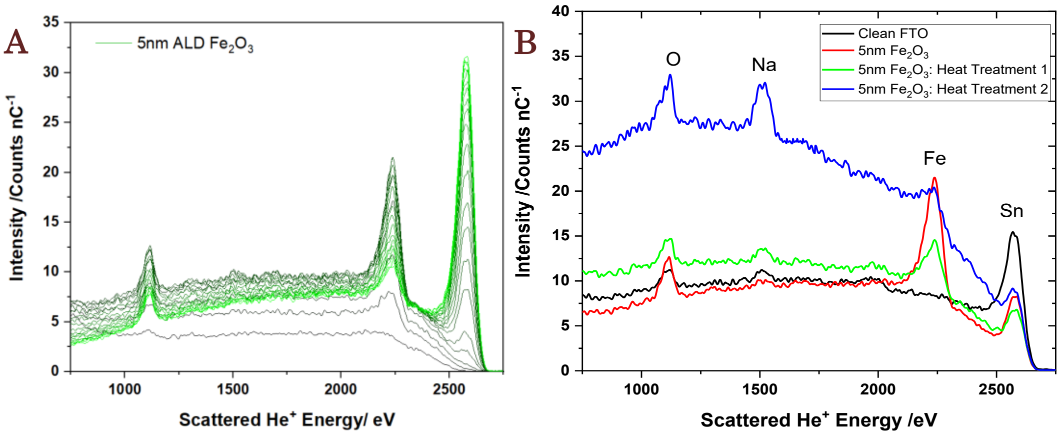

Figure 43: A) Dynamic depth profile for 5nm sample of ALD Fe_2O_3. B) LEIS surface spectra for 5nm sample of ALD Fe_2O_3 under different heat treatments, with bare FTO.

With a thin hematite layer, sputtering of the Fe_2O_3 increases the Sn peak and reduces Fe intensity, as seen with the dynamic depth profile (Figure 43A), while heating also achieves this for the surface spectra (Figure 43B). Surface spectra of bare FTO was also taken, with a Sn intensity of 17 nC^{-1}. This compares to ~14 nC^{-1} for the electrodeposited Fe_2O_3 and ~0.15 nC^{-1} for the ALD Fe_2O_3. Whilst this direct comparison in intensities does not reflect an exact number of Sn ions present, it provides an indication of the general amount of Sn. For the ALD sample with the 0.4 nm underlayer, this number is significantly lower by comparison, somewhat reinforcing the suppression theory.

5.4.4 LEIS Analysis of Samples

This movement of Sn through the sample is what is commonly theorised the high heating step achieves, with Sn doping improving rates of hole transfer for hematite photoanodes.[66] For the ALD hematite layers here, there is an indication that Sn movement is at least partially suppressed. This suggests that the improvement in onset potential is somewhat independent of Sn doping for the ALD Fe_2O_3 samples. As indicated earlier, samples undergoing Heat

Treatment 2 have lowered overall photocurrents from the other samples (as-deposited, Heat Treatment 1). If Sn suppression is in fact occurring, this may partially explain this observation. High temperature heat treatments increase the resistivity if the FTO substrate, but Sn migration counters this, with the overall process having a net positive result.[67,68] However, without the same level of Sn doping this benefit may not be as intense, resulting in reduced photocurrents for the 750°C samples.

The LEIS results offer further insight into the temperature induced improvements in onset potential, with an increase in charge carriers such as Na and F seen on the sample surfaces and within the upper layers. This could indicate an increase in charge carriers following heating, improving charge transport in the films.[69] In looking to literature, no studies for Na-doping of Fe_2O_3 were found, though this has been explored for other photoanodes. For TiO_2, Na^+ presence in the metal oxide lattice generated more oxygen vacancies, improving performance.[70] This Na induced increase in oxygen vacancies and crystal defects were also seen for WO_3, as well as for ZnO.[71] For ZnO, the Na doped samples showed the greatest improvement versus Ni, Co and K doping.[72] The increased levels of Na within the sample and accumulated at the surface are one explanation for the improved onset with high heat treatment. As 20 minutes of high heat exposure is the standard to drive Sn movement, yet no Sn movement is seen here, this is a plausible scenario.[73] This lack of movement is possibly due to the amorphous structure of the hematite produced, preventing the movement of larger atoms such as Sn.

For samples with aluminium underlayers, the improvement in onset potential is likely a combination of factors. FTO/Fe_2O_3 lattice mismatch is a known issue, resulting in poor crystallinity at the interface. Electron transport across this area is vital and thus various interfacial layers have been assessed to be beneficial. [45,74–80] For thicker films, research indicates that the crystallinity improvement is the key method of action, though when used in thin films underlayers also provide a level of doping.[77,81] Band bending in these films is also more pronounced, as well as lower recombination rates due to improved charge transfer.[74,79] On the whole, thinner underlayers offer the greatest improvement, as thicker layers supposedly reduce Sn movement through the samples.[80] As Sn movement is suppressed via the hematite in this study, this explanation can be ruled out.

However, when underlayers with mis-matched bandgaps to the substrate are used (such as Al_2O_3 with Fe_2O_3), electron movement occurs via tunnelling, making thinner layers more important. [76,82,83] This is a reasonable explanation as to why underlayers exceeding 0.5 nm showed decreased electrochemical activity. To add to this theory, aluminium oxide produced via PEALD has been found to contain structural defects that can act as charge traps.[84,85] These defects were found to advantageously fill with electrons under positive bias, but were only beneficial with thinner layers.

5.4 Conclusion

In conclusion, the ALD hematite produced exhibited interesting electrochemical properties that were directly affected by heat treatment. Novel interactions were observed for front and back illumination, while introducing aluminium underlayers further alters film properties. An underlayer thickness of 0.5 nm Al_2O_3 was found to be particularly favourable for performance, with thicker layers exhibiting decreased photoresponse.

Heat treatment has a dualistic effect, with both positive and negative results. A heat treatment of 550°C improves both photocurrent and onset potential for the samples, whereas heating to 750°C offers improvements in onset only. There are a multitude of explanations for these observations, with LEIS analysis providing detail on the compositional changes occurring. In contrast to previous studies, Sn migration was seen in lower amounts for these samples, though Al, Na and F movement was observed in a greater quantity. This highlights that the onset improvement following 750°C Heat Treatment in these samples occurs independently of Sn doping, offering new insight into photoelectrochemical improvement of ALD-Fe_2O_3 films.

References

1 M. García-Tecedor, D. Cardenas-Morcoso, R. Fernández-Climent and S. Giménez, *Adv. Mater. Interfaces*, 2019, **6**, 1900299.

2 B. Z. Yong, .

3 Z. Zhou, S. Wu, L. Li, L. Li and X. Li, *ACS Appl. Mater. Interfaces*, 2019, **11**, 5978–5988.

4 A. Hankin, J. C. Alexander and G. H. Kelsall, *Phys. Chem. Chem. Phys.*, 2014, **16**, 16176–16186.

5 K. Sekizawa, K. Oh-ishi and T. Morikawa, *Dalt. Trans.*, 2020, **49**, 659–666.

6 Z. Lin, J. Hu, B. Zhang, L. Wu and J. Wang, *Appl. Catal. A Gen.*, 2023, **652**, 119024.

7 T. Imrich, M. Neumann-Spallart and J. Krýsa, *Photochem. Photobiol. Sci.*, 2023, **22**, 419–426.

8 A. Breeuwsma and J. Lyklema, *Discuss. Faraday Soc.*, 1971, **52**, 324–333.

9 M. Labbe, K. Cadien and D. G. Ivey, *J. Phys. Chem. C*, 2022, **126**, 19883–19894.

10 Z. Zhang, H. Nagashima and T. Tachikawa, *Angew. Chemie Int. Ed.*, 2020, **59**, 9047–9054.

11 B. Iandolo, B. Wickman, I. Zorić and A. Hellman, *J. Mater. Chem. A*, 2015, **3**, 16896–16912.

12 J. T. Jang, H. Ryu and W. J. Lee, *J. Alloys Compd.*, 2015, **638**, 387–392.

13 P. Dias, A. Vilanova, T. Lopes, L. Andrade and A. Mendes, *Nano Energy*, 2016, **23**, 70–79.

14 I. Rodríguez-Gutiérrez, B. Mouriño, A. L. M. Freitas, C. A. R. Costa, E. L. Pires, R. V Gonçalves, L. Vayssieres and F. L. Souza, *ECS J. Solid State Sci. Technol.*, 2022, **11**, 43001.

15 K. Kang, H. Zhang, J. H. Kim, W. J. Byun and J. S. Lee, *Nanoscale Adv.*, 2022, **4**, 1659–1667.

16 J. Cai, S. Li, Z. Li, J. Wang, Y. Ren and G. Qin, *J. Alloys Compd.*, 2013, **574**, 421–426.

17 N. Liédana, A. Galve, C. Rubio, C. Téllez and J. Coronas, *ACS Appl. Mater. Interfaces*, 2012, **4**, 5016–5021.

18 Z. Fu, T. Jiang, Z. Liu, D. Wang, L. Wang and T. Xie, *Electrochim. Acta*, 2014, **129**, 358–363.

19 N. D. Quang, P. C. Van, D. D. Le, S. Majumder, N. D. Chinh, J.-R. Jeong, C. Kim and D. Kim, *Appl. Surf. Sci.*, 2021, **558**, 149898.

20 A. Taniguchi, T. Taniguchi, H. Wagata, K. Katsumata, K. Okada and N. Matsushita, *CrystEngComm*, 2019, **21**, 4184–4191.

21 S. Selvaraj, H. Moon and D. Kim, *Appl. Surf. Sci.*, 2018, **429**, 42–47.

22 A. Ponti, M. H. Raza, F. Pantò, A. M. Ferretti, C. Triolo, S. Patanè, N. Pinna and S. Santangelo, *Langmuir*, 2020, **36**, 1305–1319.

23 F. Bouhjar, B. Bessaïs and B. Marí, *J. Solid State Electrochem.*, 2018, **22**, 2347–2356.

24 K. C. Bedin, A. L. M. Freitas, A. Tofanello, I. Rodríguez-Gutiérrez and F. L. Souza, *Int. J. Ceram. Eng. Sci.*, 2020, **2**, 204–227.

25 P. Qiu, H. Yang, L. Yang, Q. Wang and L. Ge, *Electrochim. Acta*, 2018, **266**, 431–440.

26 D. A. Bellido-Aguilar, A. Tofanello, F. L. Souza, L. N. Furini and C. J. L. Constantino, *Thin Solid Films*, 2016, **604**, 28–39.

27 V. Zardetto, T. M. Brown, A. Reale and A. Di Carlo, *J. Polym. Sci. Part B Polym. Phys.*, 2011, **49**, 638–648.

28 P. S. Shinde, A. Annamalai, J. H. Kim, S. H. Choi, J. S. Lee and J. S. Jang,

Sol. Energy Mater. Sol. Cells, 2015, **141**, 71–79.

29 H. Kong, J. Kwon, D. Paeng, W. J. Jung, S. Ghimire, J. Dho, J.-H. Yoo, S. Hong, J. Jung, J. Shin, C. P. Grigoropoulos, S. H. Ko and J. Yeo, *ACS Appl. Mater. Interfaces*, 2020, **12**, 48917–48927.

30 J. Y. Kim, D. H. Youn, J. H. Kim, H. G. Kim and J. S. Lee, *ACS Appl. Mater. Interfaces*, 2015, **7**, 14123–14129.

31 M. Rozana, K. A. Razak, C. K. Yew, Z. Lockman, G. Kawamura and A. Matsuda, *J. Mater. Res.*, 2016, **31**, 1681–1690.

32 K. G. Upul Wijayantha, S. Saremi-Yarahmadi and L. M. Peter, *Phys. Chem. Chem. Phys.*, 2011, **13**, 5264–5270.

33 S. Corby, E. Pastor, Y. Dong, X. Zheng, L. Francàs, M. Sachs, S. Selim, A. Kafizas, A. A. Bakulin and J. R. Durrant, *J. Phys. Chem. Lett.*, 2019, **10**, 5395–5401.

34 M. Barzgar Vishlaghi, A. Kahraman and S. Kaya, *J. Phys. Chem. C*, 2019, **124**, 1337–1345.

35 Z. Pan, J. A. Röhr, Z. Ye, Z. S. Fishman, Q. Zhu, X. Shen and S. Hu, *Sustain. Energy Fuels*, 2019, **3**, 850–864.

36 S. Wang, S. Zhu, Z. Kang, X. Wang, Z. Deng, K. Hu, J. Hu, X. Liu, G. Wang, G. Zang and Y. Zhang, *Research*, 2023, **6**, 117.

37 D. F. Abbott, D. Lebedev, K. Waltar, M. Povia, M. Nachtegaal, E. Fabbri, C. Copéret and T. J. Schmidt, *Chem. Mater.*, 2016, **28**, 6591–6604.

38 P. Kumarn, P. Sharma, A. G. Joshi, R. Shrivastav, S. Dass and V. R.

Satsangi, *J. Electrochem. Soc.*, 2012, **159**, H685–H691.

39 P. Liao, M. C. Toroker and E. A. Carter, *Nano Lett.*, 2011, **11**, 1775–1781.

40 X. Li, N. C. Fan and H. J. Fan, *Chem. Vap. Depos.*, 2013, **19**, 104–110.

41 A. Ali, H. Zafar, M. Zia, I. ul Haq, A. R. Phull, J. S. Ali and A. Hussain, *Nanotechnol. Sci. Appl.*, 2016, 49–67.

42 R. Rajendran, Z. Yaakob, M. Pudukudy, M. S. A. Rahaman and K. Sopian, *J. Alloys Compd.*, 2014, **608**, 207–212.

43 M. R. Bindhu, T. D. Willington, M. R. Hatshan, S.-M. Chen and T.-W. Chen, *Environ. Res.*, 2022, **207**, 112108.

44 Z. Li, Y. Meng, H. Nie, R. Gu, X. Wang and D. Xiao, *Analyst*, 2022, **147**, 2361–2368.

45 K. Sivula, R. Zboril, F. Le Formal, R. Robert, A. Weidenkaff, J. Tucek, J. Frydrych and M. Grätzel, *J. Am. Chem. Soc.*, 2010, **132**, 7436–7444.

46 K. B. Kusuma, M. Manju, C. R. Ravikumar, H. P. Nagaswarupa, M. A. S. Amulya, M. R. Anilkumar, B. Avinash, K. Gurushantha and N. Ravikantha, *Sensors Int.*, 2020, **1**, 100039.

47 F. Le Formal, K. Sivula and M. Grätzel, *J. Phys. Chem. C*, 2012, **116**, 26707–26720.

48 H. Zhang, J. H. Kim, J. H. Kim and J. S. Lee, *Adv. Funct. Mater.*, 2017, **27**, 1702428.

49 G. Kumara, K. Tennakone, V. P. S. Perera, A. Konno, S. Kaneko and M. Okuya, *J. Phys. D. Appl. Phys.*, 2001, **34**, 868.

50 D. Hiller, D. Tröger, M. Grube, D. König and T. Mikolajick, *J. Phys. D. Appl. Phys.*, 2021, **54**, 275304.

51 M. Forster, R. J. Potter, Y. Yang, Y. Li and A. J. Cowan, *ChemPhotoChem*, 2017, **2**, 183–189.

52 R. Liu, Z. Zheng, J. Spurgeon and X. Yang, *Energy Environ. Sci.*, 2014, **7**, 2504–2517.

53 L. M. Peter, *J. Solid State Electrochem.*, 2013, **17**, 315–326.

54 L. M. Peter, A. B. Walker, T. Bein, A. G. Hufnagel and I. Kondofersky, *J. Electroanal. Chem.*, 2020, **872**, 114234.

55 D. Meissner, C. Sinn, J. Rimmasch, R. Memming and B. Kastening, eds. W. H. BLOSS and F. B. T.-A. I. S. E. T. PFISTERER, Pergamon, Oxford, 1988, pp. 2999–3002.

56 F. Le Formal, E. Pastor, S. D. Tilley, C. A. Mesa, S. R. Pendlebury, M. Grätzel and J. R. Durrant, *J. Am. Chem. Soc.*, 2015, **137**, 6629–6637.

57 Gurudayal, S. Y. Chiam, M. H. Kumar, P. S. Bassi, H. L. Seng, J. Barber and L. H. Wong, *ACS Appl. Mater. Interfaces*, 2014, **6**, 5852–5859.

58 Q. Zhang, V. Celorrio, K. Bradley, F. Eisner, D. Cherns, W. Yan and D. J. Fermín, *J. Phys. Chem. C*, 2014, **118**, 18207–18213.

59 F. Le Formal, S. R. Pendlebury, M. Cornuz, S. D. Tilley, M. Grätzel and J. R. Durrant, *J. Am. Chem. Soc.*, 2014, **136**, 2564–2574.

60 Z. Zhou, S. Wu, C. Xiao, L. Li and X. Li, *Phys. Chem. Chem. Phys.*, 2020, **22**, 7306–7313.

61 A. Kleiman-Shwarsctein, M. N. Huda, A. Walsh, Y. Yan, G. D. Stucky, Y.-S. Hu, M. M. Al-Jassim and E. W. McFarland, *Chem. Mater.*, 2010, **22**, 510–517.

62 B. Iandolo, H. Zhang, B. Wickman, I. Zorić, G. Conibeer and A. Hellman, *RSC Adv.*, 2015, **5**, 61021–61030.

63 D. Bhowmik and S. Bhattacharjee, *Appl. Phys. A*, 2022, **128**, 605.

64 M. Kamei, Y. Shigesato, S. Takaki, Y. Hayashi, M. Sasaki and T. E. Haynes, *Appl. Phys. Lett.*, 1994, **65**, 546–548.

65 Y. Ling and Y. Li, *Part. Part. Syst. Charact.*, 2014, **31**, 1113–1121.

66 H. K. Dunn, J. M. Feckl, A. Müller, D. Fattakhova-Rohlfing, S. G. Morehead, J. Roos, L. M. Peter, C. Scheu and T. Bein, *Phys. Chem. Chem. Phys.*, 2014, **16**, 24610–24620.

67 J. K. Yang, B. Liang, M. J. Zhao, Y. Gao, F. C. Zhang and H. L. Zhao, *Sci. Rep.*, 2015, **5**, 15001.

68 L. P. de Souza, R. O. G. Chaves, A. Malachias, R. Paniago, S. O. Ferreira and A. S. Ferlauto, *J. Appl. Phys.*, 2016, **119**, 245104.

69 S. Li, W. Xu, L. Meng, W. Tian and L. Li, *Small Sci.*, 2022, **2**, 2100112.

70 S. Shalini, R. Balasundaraprabhu, T. Satish Kumar, N. Muthukumarasamy, S. Prasanna, K. Sivakumaran and M. D. Kannan, *Mater. Lett.*, 2018, **221**, 192–195.

71 A. Enesca, R. Van Der Kroel and J. Schoonman, *Bull. Transilv. Univ. Brasov, Ser. I Eng. Sci.*

72 W. C. Lee, G. E. Canciani, B. O. S. Alwhshe and Q. Chen, *Int. J. Hydrogen Energy*, 2016, **41**, 123–131.

73 R. Morrish, M. Rahman, J. M. D. MacElroy and C. A. Wolden, *ChemSusChem*, 2011, **4**, 474–479.

74 Z. Luo, T. Wang, J. Zhang, C. Li, H. Li and J. Gong, *Angew. Chemie Int. Ed.*, 2017, **56**, 12878–12882.

75 Y. Liang, C. S. Enache and R. van de Krol, *Int. J. Photoenergy*.

76 T. Hisatomi, H. Dotan, M. Stefik, K. Sivula, A. Rothschild, M. Graetzel and N. Mathews, *Adv. Mater.*, 2012, **24**, 2699–2702.

77 O. Zandi, J. A. Beardslee and T. Hamann, *J. Phys. Chem. C*, 2014, **118**, 16494–16503.

78 T.-Y. Yang, H.-Y. Kang, K. Jin, S. Park, J.-H. Lee, U. Sim, H.-Y. Jeong, Y.-C. Joo and K. T. Nam, *J. Mater. Chem. A*, 2014, **2**, 2297–2305.

79 C. Ding, Z. Wang, J. Shi, T. Yao, A. Li, P. Yan, B. Huang and C. Li, *ACS Appl. Mater. Interfaces*, 2016, **8**, 7086–7091.

80 A. Subramanian, A. Annamalai, H. H. Lee, S. H. Choi, J. Ryu, J. H. Park and J. S. Jang, *ACS Appl. Mater. Interfaces*, 2016, **8**, 19428–19437.

81 L. Steier, I. Herraiz-Cardona, S. Gimenez, F. Fabregat-Santiago, J. Bisquert, S. D. Tilley and M. Grätzel, *Adv. Funct. Mater.*, 2014, **24**, 7681–7688.

82 T. Hisatomi, F. Le Formal, M. Cornuz, J. Brillet, N. Tétreault, K. Sivula and M. Grätzel, *Energy Environ. Sci.*, 2011, **4**, 2512–2515.

83 J. W. Park, M. A. Mahadik, H. Ma, G. W. An, H. H. Lee, S. H. Choi, W.-S. Chae, H.-S. Chung and J. S. Jang, *ACS Sustain. Chem. Eng.*, 2019, **7**, 6947–6958.

84 E. Schilirò, P. Fiorenza, C. Bongiorno, C. Spinella, S. Di Franco, G. Greco, R. Lo Nigro and F. Roccaforte, *AIP Adv.*, 2020, **10**, 125017.

85 S. Shi, S. Qian, X. Hou, J. Mu, J. He and X. Chou, *Adv. Condens. Matter Phys.*, 2018, **2018**, 7598978.

Chapter 6:
Layer Doping of Fe_2O_3

6.1 Introduction

Having explored the beneficial effects of aluminium oxide underlayers with varying thicknesses, the next step was to test how doping of the hematite impacts the electrochemical properties. In ALD 'delta-doping' is typically used to introduce dopants into a layer of material. Rather than introducing the dopant continuously, in delta doping, discrete 'layers' of dopant are introduced between thin sheets of the host material to form a multilayer.[348,349] While it is helpful to describe delta-doping in terms of discrete multilayers of dopant, it should be noted that discrete layers are unlikely to be observable in the final structure, especially after any form of heat treatment. For uniform delta doping, where the aim is to introduce a constant level of doping throughout the layer, it is typical to control the doping density by altering the number of ALD cycles of the host material between individual ALD cycles of the dopant.[350] In this study, uniform doping (Figure 44A) as well as gradient doping (Figure 44B and 44C) have been tested.

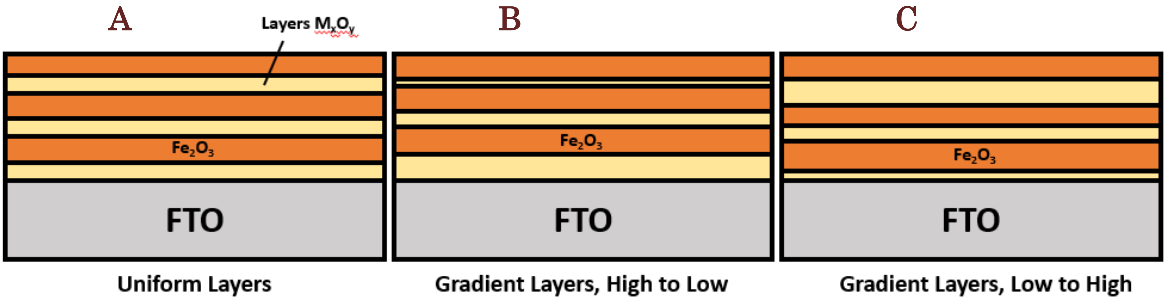

Figure 44: Cross section schematic comparing A) Uniform doping, B) Gradient doping with a high to low direction and C) Gradient doping with a low to high direction.

The uniform layers (“Uniform doping”) here are of equal ALD thickness, whereas gradient layers follow a gradient, increasing or decreasing with thickness throughout the hematite sample. The rationale behind these tests were to possibly address the observation made in Chapter 4; that ALD hematite was ‘exhibiting substrate-inhibited growth’.[279] This is an interesting test to see whether resetting the surface encourages growth throughout the ALD process, rather than reaching the plateau seen with higher deposition sequences.[132] However, the main driving force behind this study was to test the role of Al_2O_3 as a layer dopant, both in a uniform and gradient fashion. The underlayer study indicated that there was a benefit to the addition of Al_2O_3. Thus, exploring what effect the further incorporation of Al_2O_3 into the structure had on performance tests the upper limits of this benefit.

Overall, gradient doping is used for semiconductors to add layers of dopant to a material in a way that introduces a smooth change in band structure, which allows a degree of control of carrier transport mechanisms.[351] This often achieved by adding an underlayer and using heat to drive the gradient formation.[177,178] As Fe_2O_3 is produced via plasma enhanced ALD here, there is the opportunity to add layers of dopant much more precisely. This has been done previously for hematite, though rarely using ALD for the Fe_2O_3 production (less so PEALD) and not with Al_2O_3.[179] Most of the literature found for this area uses TiO_2 as the metal dopant, with polymer-assisted deposition and hydrothermal the main production forms of Fe_2O_3, with heat-induced gradients more common than physically introduced gradients.[177,350,352,353] This chapter explores the results from these experiments, once more noticing the role heat treatments have on the films.

6.2 Experimental Summary

All samples were prepared *in-situ* within the ALD reactor under vacuum. As per the previous experimental, cycles of aluminium oxide were introduced in between thicker layers of hematite using a plasma enhanced ALD sequence. The % doping was calculated based on thickness, as growth rates vary wildly between different metal oxides. For example, if we assume a Fe_2O_3 thickness of 120 nm, 5% doping here would be a total of 6nm of Al_2O_3. Using this estimate, an ALD sequence could be tailored that achieved that goal (Table 6).

Table 6: ALD sequences used to introduce layer doping into samples. (UD) denotes uniform doping throughout and (GD) signifies gradient doping. L-H and H-L indicate the direction of the gradient doping, with L-H being low to high, i.e., low levels of doping near the FTO interface, increasing in thickness towards the surface, and vice versa. This is reflected in the ALD sequence.

Sample	**ALD Sequence**	**Total number of cycles**
ALD Fe_2O_3	2400 cycles $Fe(cp)_2$	2400 Fe_2O_3
ALD Fe_2O_3 + **1.25%** Al_2O_3 (UD)	3 sub-cycles Al_2O_3 with 480 sub-cycles Fe_2O_3, repeated 5 times	15 Al_2O_3 2400 Fe_2O_3
ALD Fe_2O_3 + **2.5%** Al_2O_3 (UD)	6 sub-cycles Al_2O_3 with 480 sub-cycles Fe_2O_3, repeated 5 times	30 Al_2O_3 2400 Fe_2O_3
ALD Fe_2O_3 + **5%** Al_2O_3 (UD)	12 sub-cycles Al_2O_3 with 480 sub-cycles Fe_2O_3, repeated 5 times	60 Al_2O_3 2400 Fe_2O_3
ALD Fe_2O_3 + **10%** Al_2O_3 (UD)	24 sub-cycles Al_2O_3 with 480 sub-cycles Fe_2O_3, repeated 5 times	120 Al_2O_3 2400 Fe_2O_3
ALD Fe_2O_3 + **5%** Al_2O_3 **(GD: L-H)**	4, 6, 10, 15, 25 sub-cycles Al_2O_3 with 480 sub-cycles Fe_2O_3 in between	60 Al_2O_3 2400 Fe_2O_3
ALD Fe_2O_3 + **5%** Al_2O_3 **(GD: H-L))**	25, 15, 10, 4, 6 sub-cycles Al_2O_3 with 480 sub-cycles Fe_2O_3 in between	60 Al_2O_3 2400 Fe_2O_3

This ALD sequencing was planned to keep the total amount of Fe_2O_3 consistent throughout, with the final surface layer also a constant thickness of hematite (480 cycles ≈ 24 nm Fe_2O_3). As an example, the final structure for 5% Al_2O_3 with uniform doping would be layers of ~1.2 nm Al_2O_3 trapped between ~24 nm sheets of Fe_2O_3.

Electrochemical results were obtained using the same parameters as previous, including using 1M NaOH electrolyte with a 150 W Xe lamp and PalmSens3 potentiostat.

6.3 Uniform Layer Doping with Al_2O_3

6.3.1 As deposited

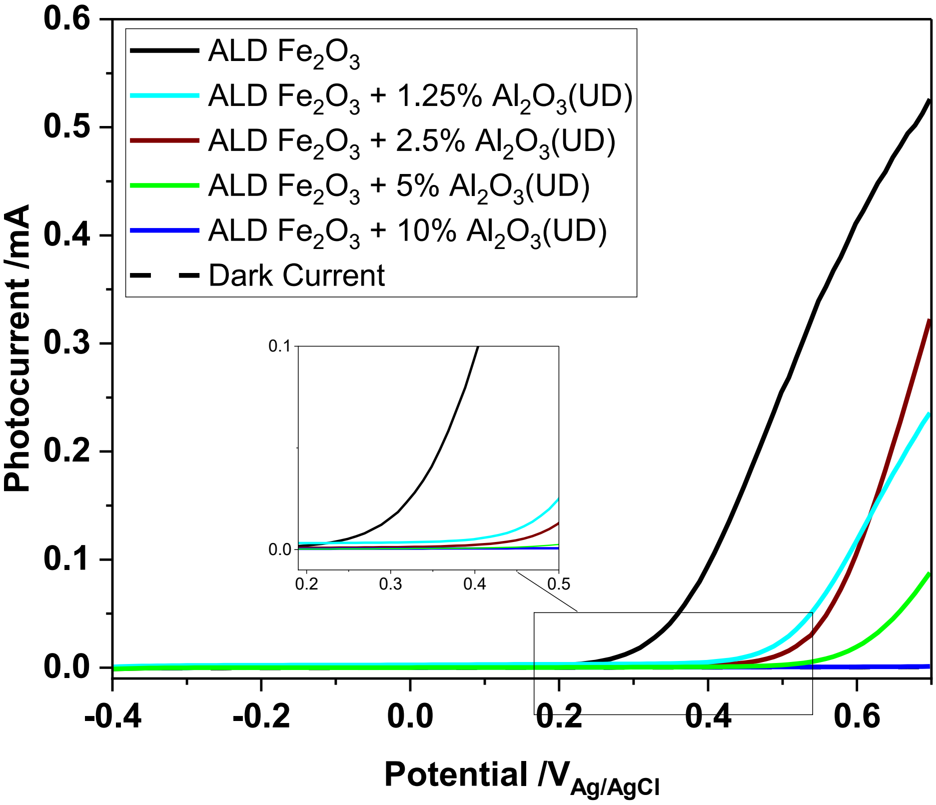

Figure 45: Linear Sweep Voltammetry (LSV) for standard hematite (black) and various % uniform doped (UD) samples as-deposited, without heat exposure.

Electrochemical results for the as-deposited samples were consistent with what was expected based on the results from the underlayer study (Figure 45). In Chapter 5, it was observed that for thicker underlayers (1, 2 nm), there was decreased photoactivity, with the films requiring heat to start showing reasonable activity. The lowest % amounts here, 1.25% and 2.5% uniform doping, have layers of a thickness (0.3 nm, 0.6 nm respectively) comparable to the 0.5nm underlayer sample in the previous study. From that study there was a drop off in performance for underlayers exceeding 0.5 nm thickness. Doping percentages greater that 5% have individual Al_2O_3 layers that are comparable to or exceed the 1 nm and 2 nm underlayers from the previous study. While the overall amount of aluminium is higher for the uniform doped samples, this same pattern of behaviour can be seen here, with a stepwise decrease in performance prior to heat treatment.

Photoactivity was generally quite low across the samples, with 1.25% and 2.5% showing a degree of activity, 5% showing a lowered amount, with 10% uniform doping offering little over the dark current. This indicated that for 10% there was little to no photoactivity occurring. However, this stepwise decrease in performance was anticipated due to the insulating properties of aluminium oxide. Larger amounts of the high bandgap (~7eV) material will hinder electron movement through the samples, worsening photoelectrochemical performance. Mismatch in alignment of the bandgaps and band edges between hematite (~2.2eV) and the aluminium oxide further this issue, with the E_{CB}= -4.8 eV and E_{VB}= -7 eV for Fe_2O_3, and E_{CB}= ~6 eV and E_{VB}= ~ -1 eV for Al_2O_3.[354–356] Having a similarly aligned band gap is beneficial for preventing charge transfer between ions, hence this mismatch will be problematic for thicker layers.[161,357] On the whole, the as-deposited uniform doping with aluminium offers no distinct advantage to the ALD Fe_2O_3, worsening both onset and photocurrent.

6.3.2 Heat Treatment 1

Following a 2 hour 550°C anneal in air, all samples showed an element of improvement (Figure 46). There is a cathodic shift in onset potential for each sample, whilst the 10% doped photoanode was more responsive than previous.

Interestingly, both the 1.25% and 2.5% Al_2O_3 uniform doped samples exhibited lower maximum photocurrents at 0.7V $_{Ag/AgCl}$ following heat exposure.

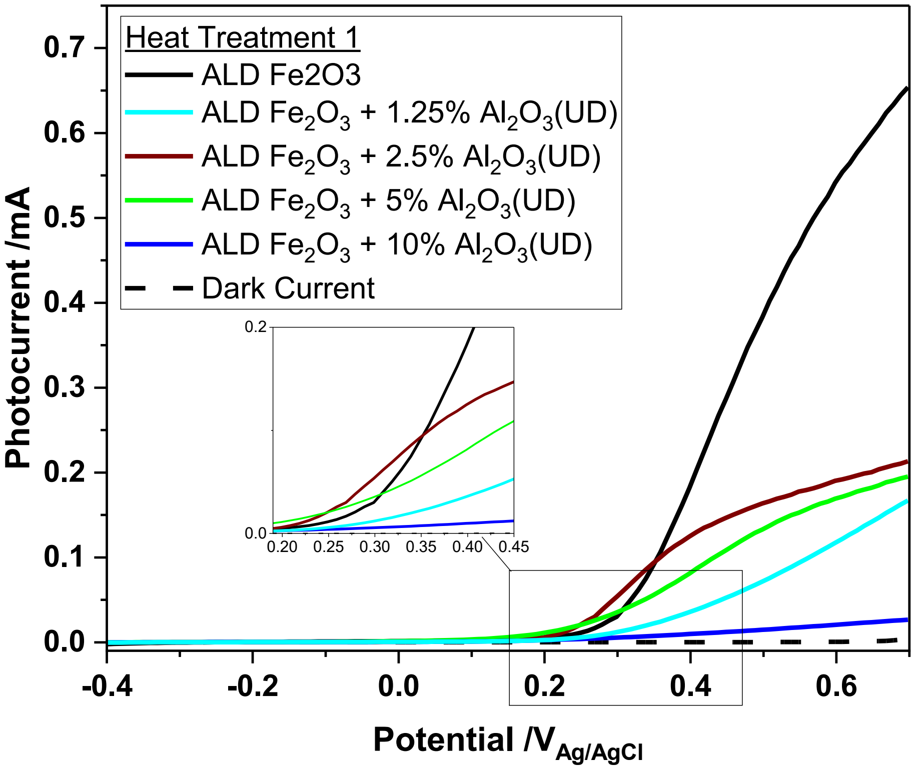

Figure 46: Linear Sweep Voltammetry (LSV) for samples following Heat Treatment 1 (550°C for 2 hours)

This unusual observation for electrochemistry corresponds to the physical appearance of the samples. Figure 47 shows the typical progression seen when heat treating the samples, with the undoped ALD Fe_2O_3 (Fig.3A) partially deepening in colour following Heat Treatment 1. As mentioned previously, this step induces crystallinity changes in the hematite, resulting in a colour change.

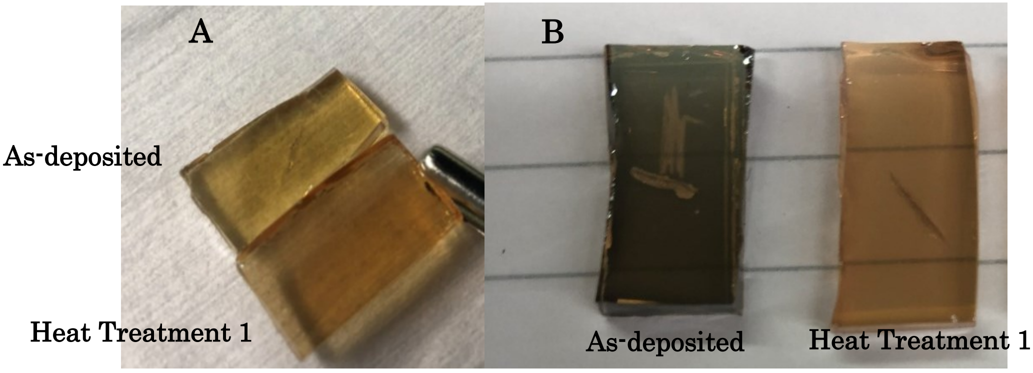

Figure 47: Photo comparison between samples. A) Side to side comparison of ALD Fe_2O_3 sample pre (yellow, paler) and post (orange, darker) Heat Treatment. B) Stepwise comparison for 10% Al_2O_3 uniform doped sample. Greyed sample is as deposited. The right sample is following Heat Treatment 1.

However, these aluminium doped films had a greyer cast upon film deposition, with the higher % doped samples particularly darkened (Fig.3B). This dark grey-black colour is suggestive of magnetite growth (Fe_3O_4) and may partially explain the altered electrochemistry here.[358,359] Interestingly, this observation has been previously noted for iron oxides grown on aluminium oxide, which showed magnetite preference prior to annealing.[360] The suggested cause of this was inhibited growth of α-Fe_2O_3 due to slow activation kinetics, with poor O_2 dissociation. As this observation was made for iron oxide grown on thicker Al_2O_3, this explains why the colour change was not previously seen. Likely, a larger amount of aluminium is required to drive this change, versus the sub 1nm underlayers previously studied. As the 1.25 and 2.5% doped samples were only partially greyed, it is likely a lesser degree of formation occurred with the smaller amounts. However, the presence of magnetite explains the increased photocurrent, as magnetite is more conductive than many other iron oxides, including hematite. The presence of both Fe_{2+} and Fe_{3+} in the magnetite structure results in a significantly smaller bandgap and allows for easier hole and electron movement.[361] However, due to its slow transformation to γ-Fe_2O_3 in air, it is not commonly used as a photoanode material. However, in this context, it is likely that the magnetite is partially protected by further layers of hematite, as the unheated samples remained grey coloured since production. Quite possibly this production method using Al_2O_3 offers a unique pathway to viable magnetite use in the future.

6.3.3 Heat Treatment 2

Similar to the underlayer results, the high temperature anneals resulted in some interesting changes (Figure 48). All samples showed improvement in onset potential, with the doped samples exhibiting impressive onsets.

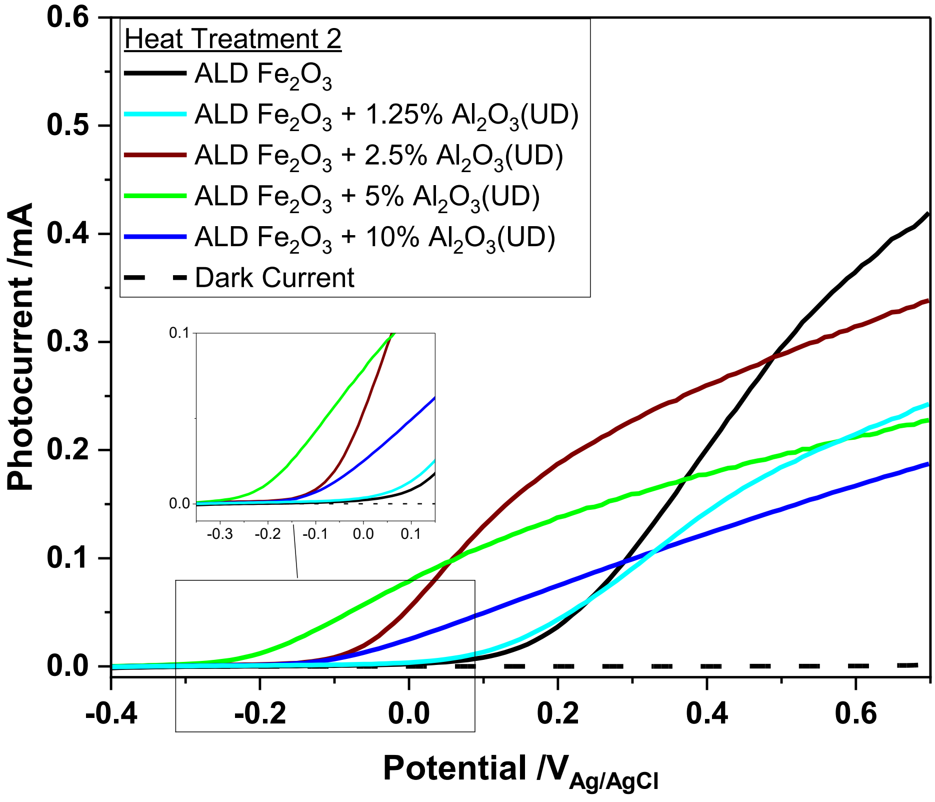

Figure 48: Linear Sweep Voltammetry (LSV) for samples with Heat Treatment 2 (550°C for 2 hours, followed by 20 minutes at 750°C)

The aluminium doped samples also have increased photocurrent compared to Heat Treatment 1. The 10% doped sample shows vast improvement, but, as with the underlayer study, too much Al_2O_3 has a dampening effect on performance. However, 2.5% and 5% doped samples exhibit very good onset potentials, with 5% having an onset of -0.29 $V_{Ag/AgCl}$, or 0.73 V $_{RHE}$. This is comparable to some well performing nano samples, which exhibit very low onsets in the 0.7 V_{RHE} range, though is not a record low.[362] Specifically, Ti-modified dendritic hematite exhibited an onset potential (V_{on}) of 0.78 V_{RHE}, nanotubular Zr-doped hematite a V_{on} of 0.62V_{RHE} and S-doped nanorods a V_{on} of 0.75 V_{RHE}.[362,363] The lowest recorded onset potential for Fe_2O_3 without surface modification is 0.61 V_{RHE}, for 'grey' hematite.[364] Directly comparing sample performance is not simple due to the number of variables and differences between samples. However, the lowest onset value found for a film comparable in nature (Fe_2O_3 produced via ALD, sample heated to 800°C and uniform doped with Sn), was V_{on} = 1.05V_{RHE}. This highlights the value of Al doping in this capacity, with the onset value achieved impressive for ALD-hematite.

6.3.4 Uniform Doping Summary

The trend between performance and increasing the % Al_2O_3 doping amount for the hematite samples is non-linear (Figure 49). The peak photocurrent obtained fluctuated following heat exposure and with % Al doping. The highest recorded photocurrent was for the pristine Fe_2O_3 sample with Heat Treatment 1 at 0.65 $mA.cm^{-2}$, wherein Heat Treatment 2 shows diminished output for the same specimen (0.41 $mA.cm^{-2}$). Yet 1.25% doping exhibits a reversal of this trend, with Heat Treatment 1 performing the least favourably.

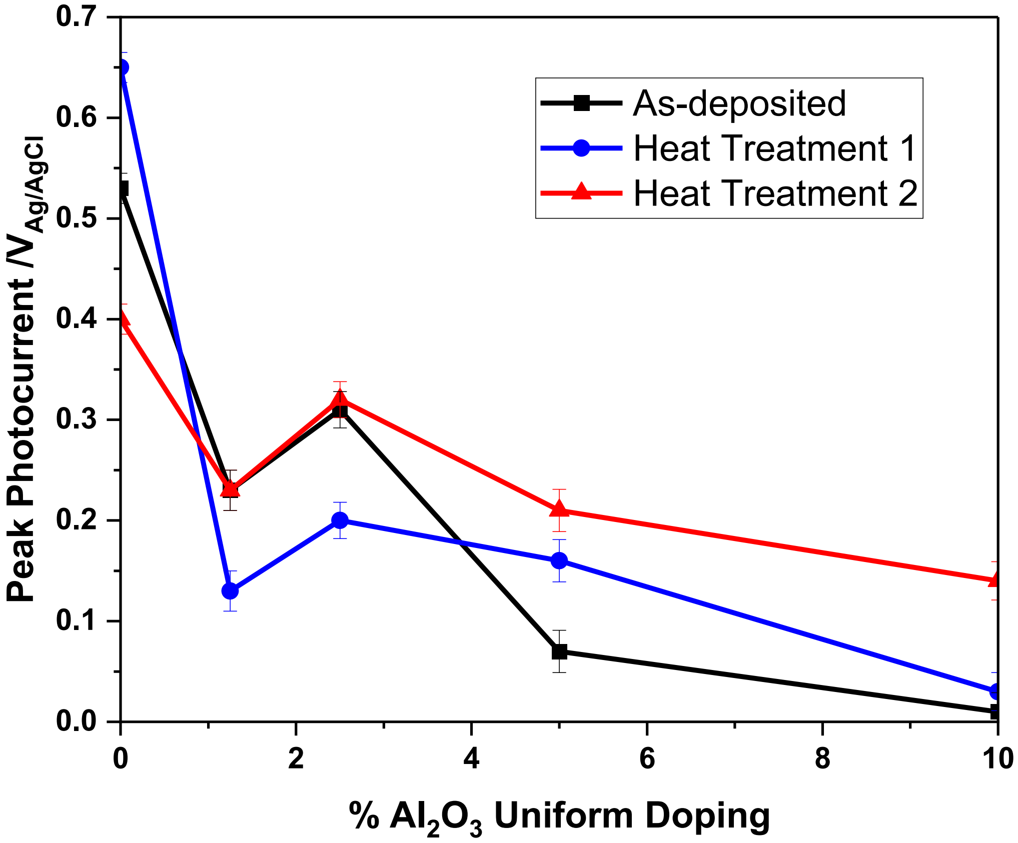

Figure 49: Relationship between % doping and photocurrent over different heat exposures.

A clear pattern exists beyond 5% doping, where increased heat exposure improves photocurrent – though photocurrent is diminished for high doping levels overall. For samples with less than 5% Al_2O_3 content, there is no clear pattern. Overall, these photocurrents are unremarkable, by both the highest achieved value (>4 mA.cm^{-2}) and compared to the photocurrents obtained for the underlayer samples in Chapter 5.[365] The peak photocurrent obtained in Chapter 5 was 1.29 mA.cm^{-2} for Fe_2O_3 with a 0.5 nm Al_2O_3 underlayer. It can be concluded from these results that doping with larger amounts of Al results in diminished photocurrents.

In contrast to photocurrent, there is a distinct trend in onset potential with increasing aluminium content and following heat exposure (Figure 50). V_{on}

for as-deposited samples diminished with increased Al_2O_3 levels, with 10% Al_2O_3 doped hematite exhibiting the worst onset (the most positive) across all samples.

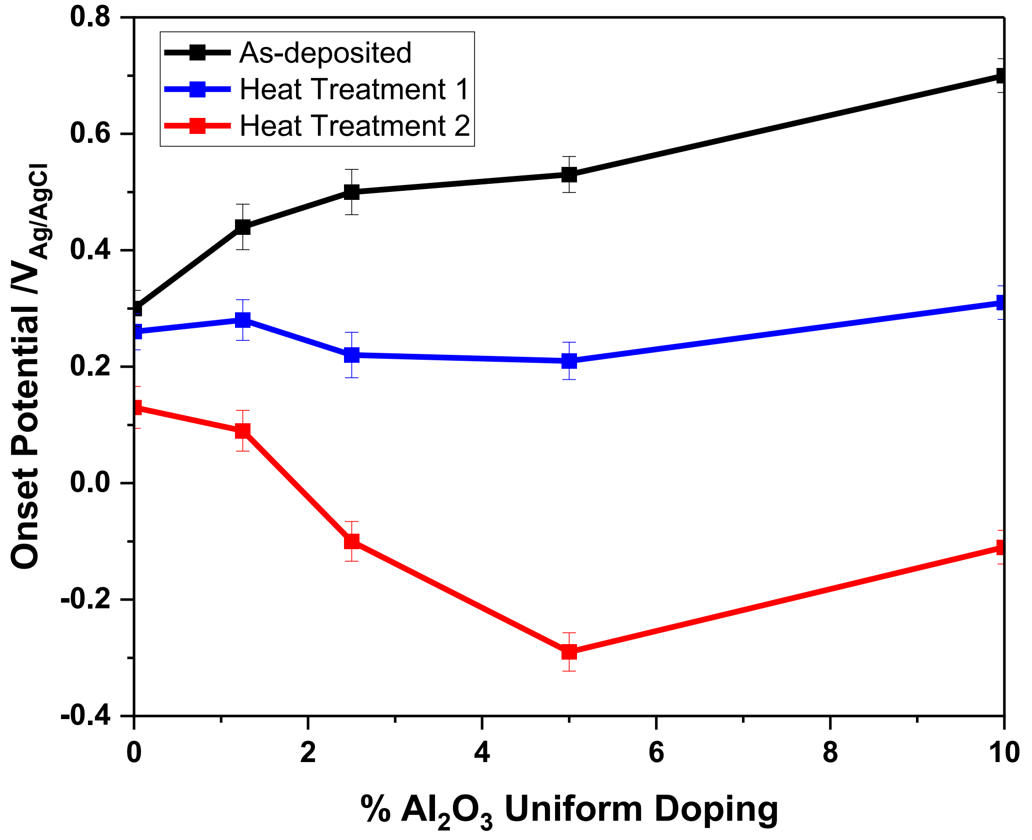

Figure 50: Relationship between % doping and onset over different heat exposures.

With Heat Treatment 1 and 2, there was a stepwise decrease in onset compared to the non-heated equivalents. Increased levels of aluminium doping are not favourable until the high heat exposure of 750ºC occurs. At this point, the introduction of aluminium greatly improves the onset potential, though there is a plateau in the decrease as Al_2O_3 increases. 10% Al_2O_3 uniform doping has a marginally lowered onset from 2.5%, but a maximum degree of improvement is reached before this point, highlighting that there is a preferred level. This sweet spot is reached at 5% Al_2O_3 uniform doping. Interestingly, this observation is in line with many other doping studies, where 5% doping was found to be the optimum level for other metal oxides.[154,179,366] These onset values show great improvement from the underlayer samples, with the lowest V_{on} -0.06 $V_{Ag/AgCl}$ for 0.3-nm Al_2O_3 underlayer, versus -0.29 $V_{Ag/AgCl}$ for 5% Al doping here. This highlights that Al doping massively lowers onset potential for these hematite films, possibly at the expense of photocurrent.

6.4 Gradient Doping with Al_2O_3

6.4.1 Introduction

Understanding whether the placement of aluminium affects performance is important for these samples, as this may potentially highlight the manner in which Al acts on the hematite. The thickness of the underlayer on the electrode surface was previously shown to be consequential for performance in Chapter 5, so exploring whether thickness throughout the sample has an impact here is an equally valid question. The 5% Al doped sample was shown to have much improved onset behaviour compared to all other samples for uniform doping. This section will investigate if the placement of the aluminium is relevant, with the amount of Al introduced via ALD held constant, but the structure in which it is placed varied.

As mentioned previously, gradient doping has been highlighted as a potential avenue for improving electrochemical performance, hence this experiment also aims to answer whether gradient doping offers benefits for aluminium doped hematite. To assess this, aluminium oxide was introduced following a high-low gradient (GD: H-L), with thicker layers introduced close to the electrode interface and diminished towards the surface. A low-high sample

(GD: L-H) that followed the reverse of this was also tested. Specific details of how this was achieved are outlined in Table 1.

6.4.2 Gradient Doping with Al_2O_3 Results

Similar to the 5% uniform doped (UD) sample, the 5% gradient doped (GD) samples offer no improvement from the pristine ALD-Fe_2O_3 following A) no heat exposure and B) Heat Treatment 1 (Figure 51).

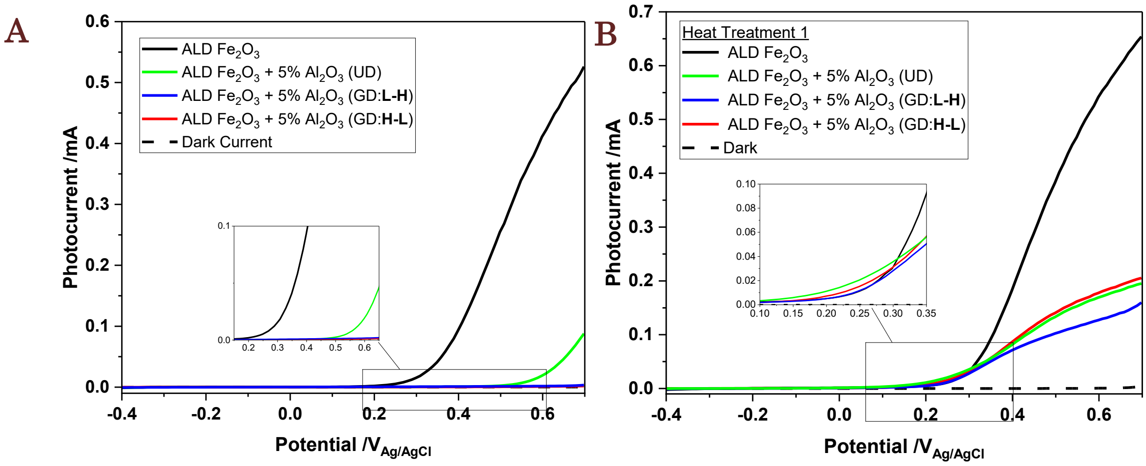

Figure 51 (A and B): A) Electrochemical results for 5% doped samples. B) Results following Heat Treatment 1.

When tested, the as-deposited GD samples exhibited little to no photoactivity, even when compared to the UD sample. This is likely a consequence of the thicker (2.5 nm) aluminium oxide layer present within both GD samples. Though the placement of this layer varies, with the thick layer at the electrode interface for H-L and closer to the surface for L-H, this is over double the thickness of the layers in the 5% UD sample (1.2 nm). This layer is comparable in thickness to those found in the 10% UD sample and the 2 nm underlayer sample, with both of these samples exhibited limited activity prior to heat treatment. Without heat treatment to disperse this layer, the thick Al_2O_3

layer will act as an insulator and inhibit electron movement through the sample.[209,300]

Heating at 550ºC lifts this effect, with all 3 doped samples exhibiting almost identical onsets. Similarly, photocurrent for the samples is comparable, with the high-low GD sample overlapping the UD sample almost perfectly. The low-high GD sample has a slightly diminished photocurrent at 0.7 $V_{Ag/AgCl}$ from the other samples, but this is still within 0.05 mA cm^{-2}. The temperature treatment likely benefits these samples in two ways: i) by reducing remaining iron oxide species to Fe_2O_3 and ii) by partially dispersing the layer of Al_2O_3. Temperature induced movement of ions is common for heat treated photoanodes and has been explored in Chapter 5 with LEIS. In this instance the temperature is likely blending the boundaries between the Al_2O_3 and Fe_2O_3, decreasing internal resistances and allowing charge transfer across this previously unpassable layer. [168,233]

Following very high heat exposure (Heat Treatment 2), there were drastic changes in the hematite films (Figure 52). All samples had the cathodically shifted onset seen previously following Heat Treatment 2, with the Al samples significantly lower than the un-doped Fe_2O_3. The low-high GD sample had a marginally improved photocurrent at 0.7 $V_{Ag/AgCl}$, reaching ~ 0.15 mA cm^{-2}.

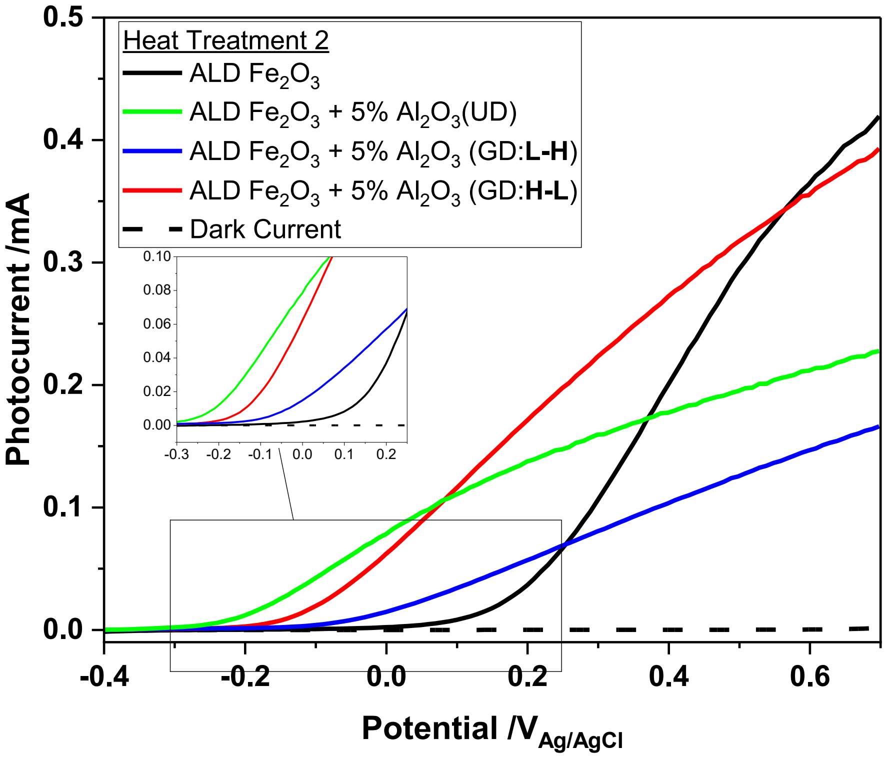

Figure 52: LSV for samples with Heat Treatment 2 (550°C for 2 hours, followed by 20 minutes at 750°C).

However, the uniform doped sample and high-low GD sample far outperformed this, with large improvements in both photocurrent and onset potential compared to previous. Interestingly, in contrast to the high-low GD sample, the UD sample had an improved onset potential but a decreased photocurrent at 0.7 $V_{Ag/AgCl}$. For the H-L GD photoanode, a photocurrent comparable to pristine ALD-Fe_2O_3 can be noted, as well as a modest onset of ~ -0.17 $V_{Ag/AgCl}$, showing similar behaviour to the 2.5% UD sample. While the onset is not as reduced as for uniform doping, the high-low gradient doping clearly offers advantages when looking to preserve photocurrent. Low-high doping appears to perform the least favourably, which offers insight into preferential doping structure for Al_2O_3/Fe_2O_3.

Overall, both UD and GD % doping with Al is extremely beneficial if looking to illicit vast improvements in onset potential. The peak photocurrents seen here are unimpressive when compared to other modified hematite photoanodes, highlighting that onset improvement would be the purpose behind adding aluminium dopants. This is especially the case when larger amounts of aluminium inhibit peak photoanode performance, though gradient doping offers a possible route around this. In depositing thicker Al layers closer to the FTO surface and using heat to distribute the Al, the photocurrent can be somewhat preserved while the onset potential also sees a modest improvement.

6.5 Gradient Doping with TiO_2

As the gradient doped aluminium samples showed a clear preference in the high-low direction, exploring whether this pattern existed for other dopants was important when looking at the mechanism of action. If the pattern existed solely for Al doped samples, then this would indicate that it is a dopant specific trend. If, however, the pattern occurs for other dopants, then this points towards it being a hematite specific trend. In either case it offers invaluable insight into hematite as a photoanode.

To investigate this question, high-low and low-high titanium dioxide (TiO_2) gradient doped Fe_2O_3 samples were produced. The gradient doping percentage was held at 5% of the total film thickness to remain consistent with the previous experiments, with the hematite layers also constant. TiO_2 was grown via ALD using a TTIP precursor and oxygen plasma process. Reactor conditions such as flow rate and temperature were unchanged across all processes, to ensure consistency with Fe_2O_3 growth. Differences in Al_2O_3 and TiO_2 ALD growth rates were accounted for in the sequence, with larger amounts of TiO_2 added to meet the same thickness requirements as previously set for the aluminium (Table 7).

Table 7: ALD sequences used to introduce TiO_2 layer doping into samples. TiO_2 growth was ~0.05nm/cycle, approximately half that of the TMA Al_2O_3 process.

Sample	ALD Sequence	Total number of cycles
ALD Fe_2O_3 + 5% TiO_2 **(GD: L-H)**	6, 14, 20, 30, 50 with 480 cycles of Fe_2O_3 in between	120 TiO_2 2400 Fe_2O_3
ALD Fe_2O_3 + 5% TiO_2 **(GD: H-L)**)	50, 30 20, 14, 6 with 480 cycles of Fe_2O_3 in between	120 TiO_2 2400 Fe_2O_3

6.5.1 Gradient Doping with TiO_2 Results

The first observation for the TiO_2 samples is that, when compared to the GD Al_2O_3 samples, they were photoactive without heat exposure (Figure 53). Though both onset potential and photocurrent response were poorer than for pristine ALD hematite, these samples performed well above the dark current, showing improved electrochemistry than for UD and GD Al doped samples under similar conditions.

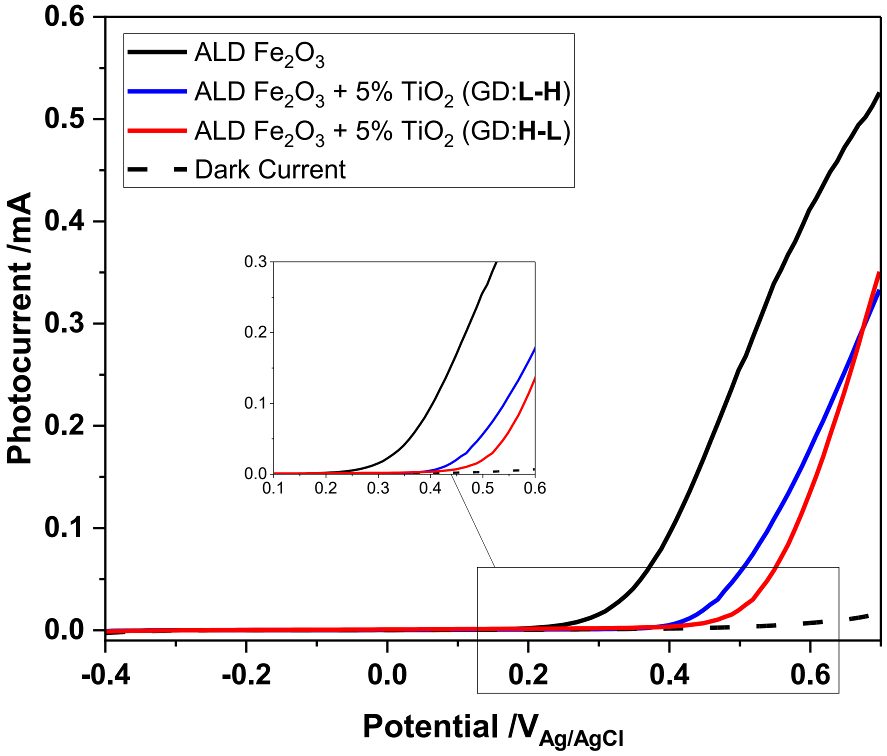

Figure 53: LSV for as-deposited TiO_2 gradient doped Fe_2O_3 samples.

Both high-low and low-high samples performed similarly, as was observed for the GD Al samples. The presence of a clear photocurrent here furthers the theory that thicker aluminium oxide layers inhibit charge transport, since there is a modest photo-response for the same thickness of TiO_2. The diminished photo-response compared to pristine hematite indicates that transport across the TiO_2/Fe_2O_3 boundary may not be favourable, which results in higher levels of recombination.[302,304] Band alignment may be of issue here, with the TiO_2 misaligned in conduction band 0.6 eV more negative than that of Fe_2O_3, meaning electron transfer requires a degree of tunnelling to pass the boundary.[170]

Following Heat Treatment 1, similar trends are observed as for the aluminium doped samples, in which temperature appears to activate the films (Figure 54). Onset was reduced beyond that of undoped hematite, and there was a slight positive increase in photocurrent. Though, for Ti doped samples, there is a marginal increase in photocurrent for the low-high gradient doping, which is dissimilar to the trend highlight for aluminium GD hematite. However, the onset potential is almost identical for the two samples following this heat treatment, which was also observed for the 5% Al_2O_3 UD/GD samples.

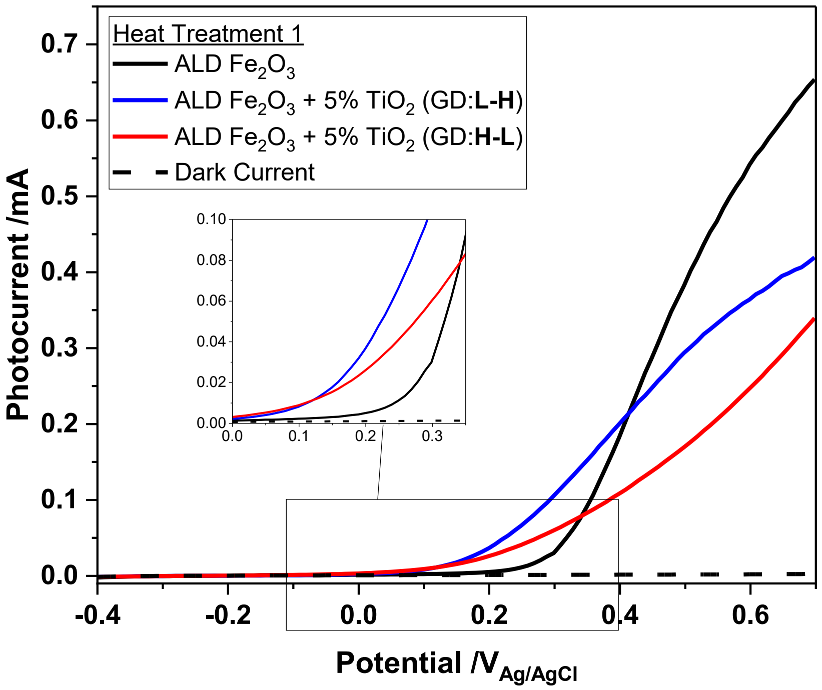

Figure 54: : LSV for GD TiO_2 samples with Heat Treatment 1.

Following Heat Treatment 2 there was a clear difference with TiO_2 doping (Figure 55). Photocurrent far surpassed that of pristine ALD hematite, topping 0.75 mA.cm^{-2}, though the onset potential was similar. After high heat exposure the high-low TiO_2 gradient doped sample was preferred, in line with what was observed for the Al GD samples.

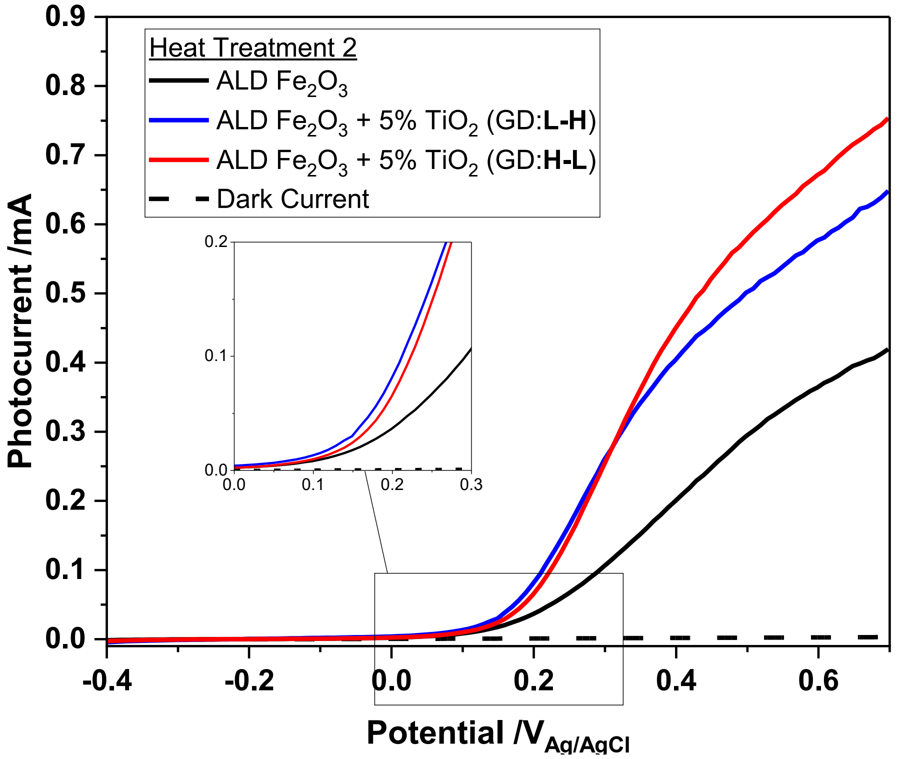

Figure 55: LSV for GD TiO_2 samples with Heat Treatment 2.

When compared to the aluminium GD samples, Ti doping has the opposite effect on photocurrent/onset. Photocurrent for Al_2O_3 samples have typically been reduced compared to pristine hematite following Heat Treatment 2, whereas the onsets massively reduced. For Ti doping there is little improvement in onset potential but a large increase in overall photocurrent. This indicates a different method of action for the two dopants.

There are five factors that determine the efficiency of a photoanode: efficiencies of charge transport, charge generation and charge transfer, and the oxidative/reduction power of holes/electrons.[93] Al^{3+} has been shown to improve charge transport in tantalum doped hematite, as the discrepancy between Fe^{3+} and Al^{3+} in ionic radius allows charge hopping.[367] However Ti^{4+} incorporation increases donor density.[199] The charge transfer improvement for Al reduces the potential required to initiate a photocurrent response, whereas the higher level of electron density from Ti doping increases the maximum achievable photocurrent.[368,369] This difference can be observed between the gradient doped Al/Ti samples, with the onset potential and photocurrent behaviour.

6.6 LEIS and Further Analysis

6.6.1.1 Uniform doping with Al_2O_3: LEIS

LEIS analysis of the samples highlights similar trends to those explored previously. Surface spectra for 1.25% Al_2O_3 uniform doping shows increased levels of aluminium following heat exposure (Figure 56), with aluminium migration to the surface for these samples following heat treatment. The as-deposited sample has no observable Al peak, however. This heat-induced migration was observed for the underlayer samples in Chapter 5, highlighting that this is consistent behaviour for heat exposed aluminium samples. No observable Sn peak can be seen on the surface of these samples, whereas a small (intensity= 0.2 nC^{-1}) sharp peak could be observed following Heat Treatment 2 for the underlayer sample.

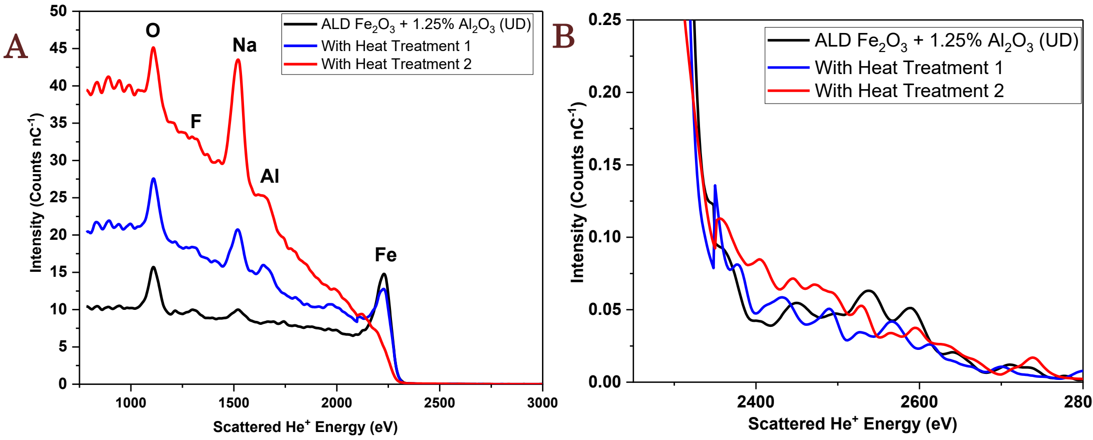

Figure 56: A) LEIS surface spectra for 1.25% Al uniform doped samples across different heat parameters. B) LEIS surface spectra across Sn region for 1.25% Al_2O_3 UD. Experiment carried out by Dr Adrian Gardner, Stephenson Institute for Renewable Energy.

Depth profiles highlight compositional changes following heat exposure (Figure 57). Similar to the hematite samples with aluminium underlayers, Na is present in the surface layers in high amounts, while sputtering reveals more aluminium with increasing depth. There is likely a degree of surface signal suppression occurring from the Na layer, with other atoms seen in greater amounts as the surface Na is sputtered away.

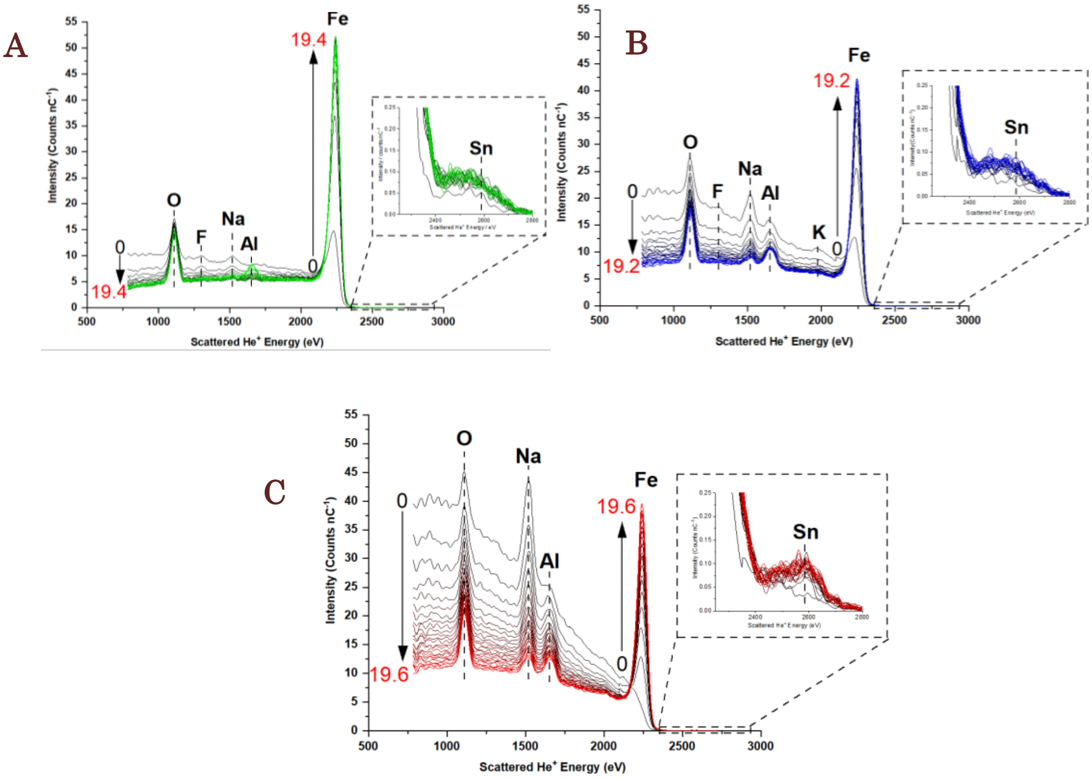

Figure 57: Depth profiling for 1.25% uniform doped Al_2O_3/Fe_2O_3, with A) no heat, B) Heat Treatment 1 and C) Heat Treatment 2. Sputtering was carried out using an Ar ion sputter gun with a dose of ~7×10^{14} ions/cm. Experiment carried out by Dr Adrian Gardner, Stephenson Institute for Renewable Energy. Also shown is the corresponding change to the baseline signal at a scattered He^+ energy ~1000 eV and the intensity of the Fe surface peak are shown with an arrow to orientate the reader.

Depth profiling across the as-deposited sample shows a clear onset for the Al_2O_3 layer, which was placed ~24nm below the surface. Once uncovered, the Al intensity remains approximately constant with increasing depth, suggesting that either Al is not fully removed by the sputtering process, or that there is a sustained level of Al through the sample.[247] For the as-deposited sample, the Fe peak is comparable in intensity to non-doped samples, but the increased levels of Na and Al on the surface following heat exposure suppress this peak for the heat-treated samples. Increased amounts of aluminium can be seen following Heat Treatment 2, which once again highlights migration of Al from deeper Al_2O_3 layers. The same observation was made for the samples containing <1 nm Al_2O_3 underlayers, suggesting that Al moves very easily through these films.

Higher sodium content is once again observed at the surface following heating, which will have moved from the glass substrate. This peak extends into the bulk for all samples, indicating that Na moves through the samples, as opposed to just depositing on the surface in the furnace. A broad signal of low intensity (< 0.15 nC^{-1}) can be observed in the Sn region, indicating that there could be buried layers of Sn in this region, versus the sharper peaks observed in Chapter 5.4.2. Similar to the previous samples, this suggests that Sn migration is suppressed for these films, compared to what was observed for the electrodeposited hematite.

6.6.1.2 Uniform doping with Al_2O_3: XPS

Previous studies have highlighted that some metal species form new metal complexes with iron, resulting in a $M_xFe_yO_z$ type structure. The presence of these structures can be found with XPS, with the binding energy for the metal atoms shifting to reflect changes in oxidation state.[339] Temperature treatment for these samples results in the compositional changes seen previously (Figure 58).

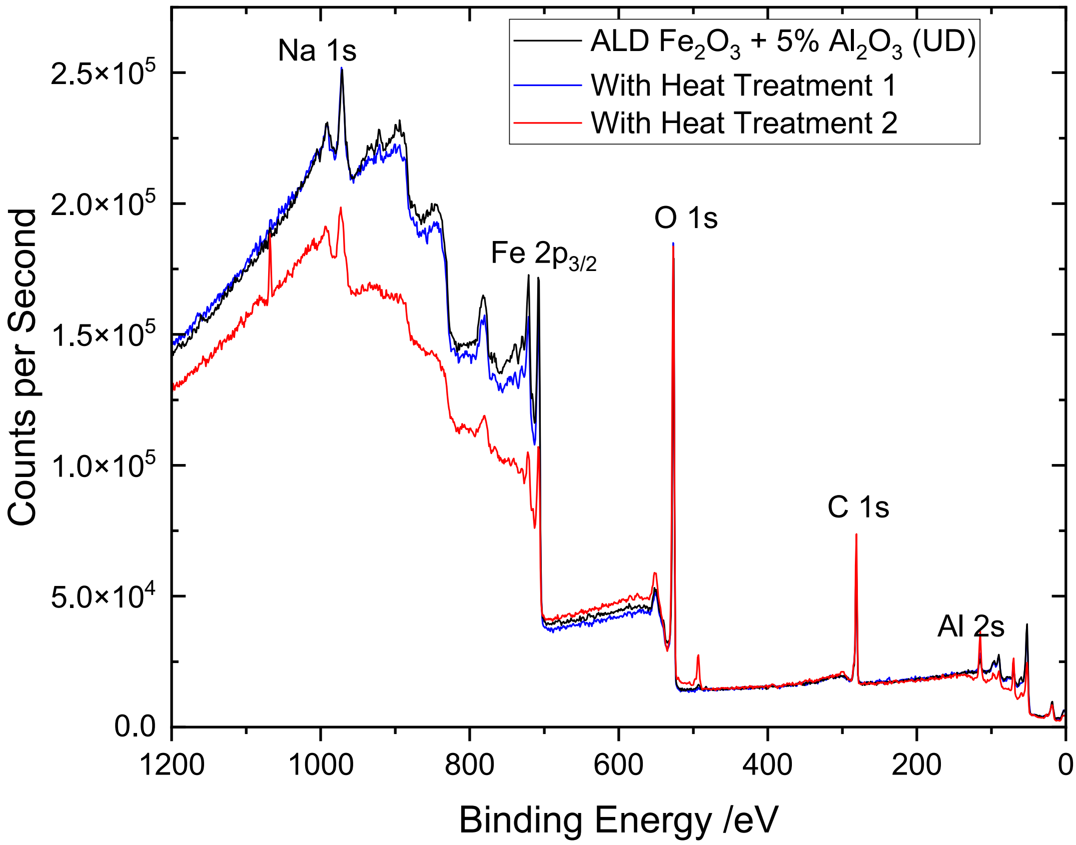

Figure 58: XPS Spectra for 5% aluminium uniform doped hematite. Experiment carried out by Dr Shamsal Haq, University of Liverpool.

Increased levels of Na and Al can be observed following heating, with decreased Fe on the surface as a result of this. Carbon impurities caused by exposure to the atmosphere are also obvious here.[370] No obvious changes to structure are highlighted in the XPS data for the 5% UD Al_2O_3/Fe_2O_3 (Figure 59).

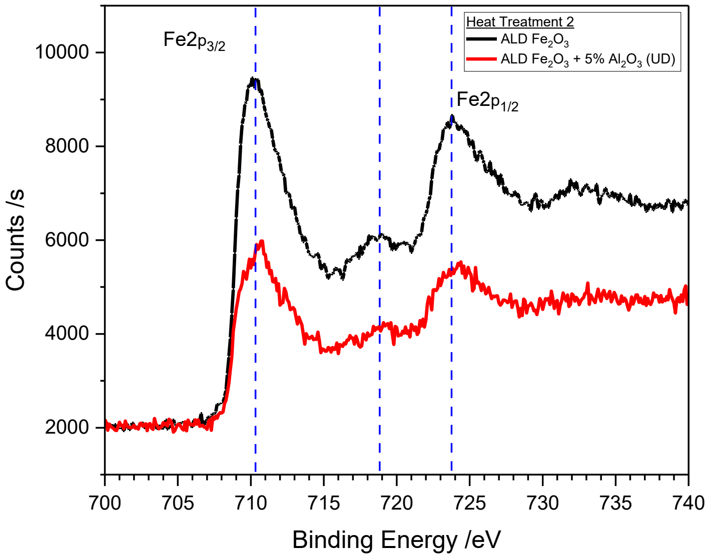

Figure 59: XPS: Fe binding energy for 5% aluminium uniform doped hematite (red) compared to undoped hematite (black).

Though lower in intensity due to the migration of Al to the surface, the Fe peaks are aligned and show the 3 characteristic peaks of α-Fe_2O_3. Similarly, for both unheated and heated UD 5% Al_2O_3 samples, there is no shift in Al peaks (Figure 60).

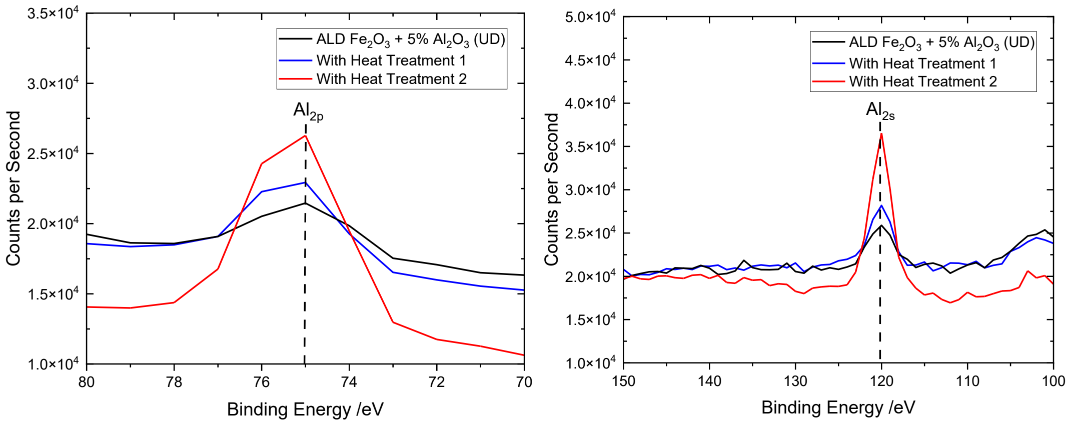

Figure 60: XPS: Al binding energies across the 3 heat parameters for 5% aluminium uniform doped hematite.

Al_{2p} binding energy can be found at almost exactly 75eV, indicating aluminium is present as Al^{3+} as Al_2O_3.[371] These spectra exclude the formation of

$Al_xFe_yO_z$ type structures, which would see deviations in peak shape and binding energy.[372]

6.6.1.3 Uniform doping with Al_2O_3: UV-Vis

For Heat Treatment 2, across the different aluminium doping profiles, slight changes in optical properties can be seen (Figure 61).

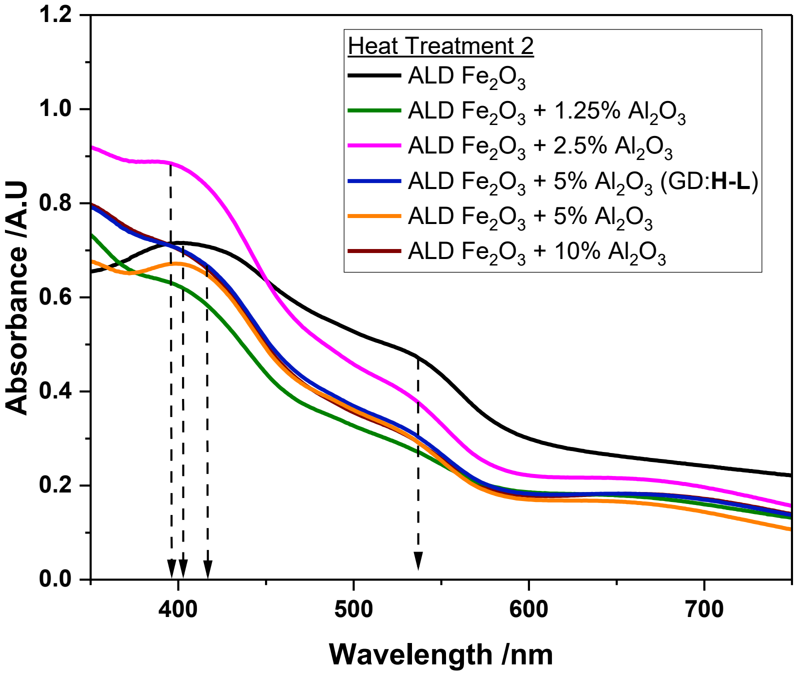

Figure 61: UV-Vis spectra for different % doping profiles. As-deposited hematite is compared to uniform doped Al_2O_3/Fe_2O_3 and gradient doped high-low Al_2O_3/Fe_2O_3.

The addition of aluminium blue shifts the 410nm peak maxima slightly compared to pristine hematite, with increased absorption below 400nm. The aluminium doped samples exhibit similar UV-Vis spectra, outside of 1.25% and 2.5% Al_2O_3 UD sample, which appear to be shifted between the pristine sample and >5% UD samples. This indicates that there is a degree of change with doping, as the 5% and 10% samples have almost identical spectra. Interestingly, the gradient doped sample overlaps almost perfectly with 10% uniform doping and is very similar to the 5% UD sample.

6.6.2 Gradient doping with Al_2O_3: LEIS

The surface spectra for the gradient doped aluminium samples is comparable to that of uniform doping, with Al at the surface following heating and suppression of the Fe peaks as a result of this (Figure 62). Na is visible in high amounts for Heat Treatment 2, with no surface Sn visible. Minor peaks can be seen for F at ~1250 eV and K at 1850 eV, further highlighting the lability of these ions.

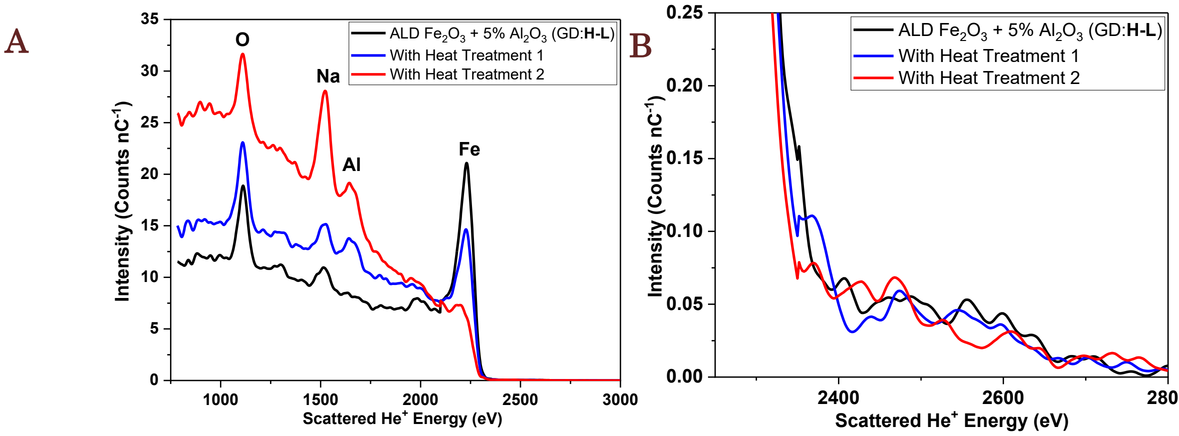

Figure 62: A) LEIS surface spectra for 5% Al_2O_3 gradient doped (high-low) samples across different heat parameters. B) Zoomed in surface spectra across Sn region. Experiment carried out by Dr Adrian Gardner, Stephenson Institute for Renewable Energy.

Dynamic depth profiling with sputtering shows further changes throughout the material (Figure 63). A broad peak in the Al region peak can be observed for the unheated sample following sputtering, with rising intensity of this peak as depth increases. This indicates the presence of buried layers, similar to what was observed for Sn previously.[373] For the heated samples the amount of surface Al remains approximately constant with increasing sputter dose; though less Al is observed for Heat Treatment 1 than Heat Treatment 2. This indicates that high temperatures drive greater migration of Al from within the samples. Compared to previous samples that have showed miniscule changes in Sn, there is no evidence of surface Sn and no change in Sn intensity with heat. Again there is a small broad hump of very low intensity in this region, indicating that there may be buried layers of Sn , but no strong presence was found.

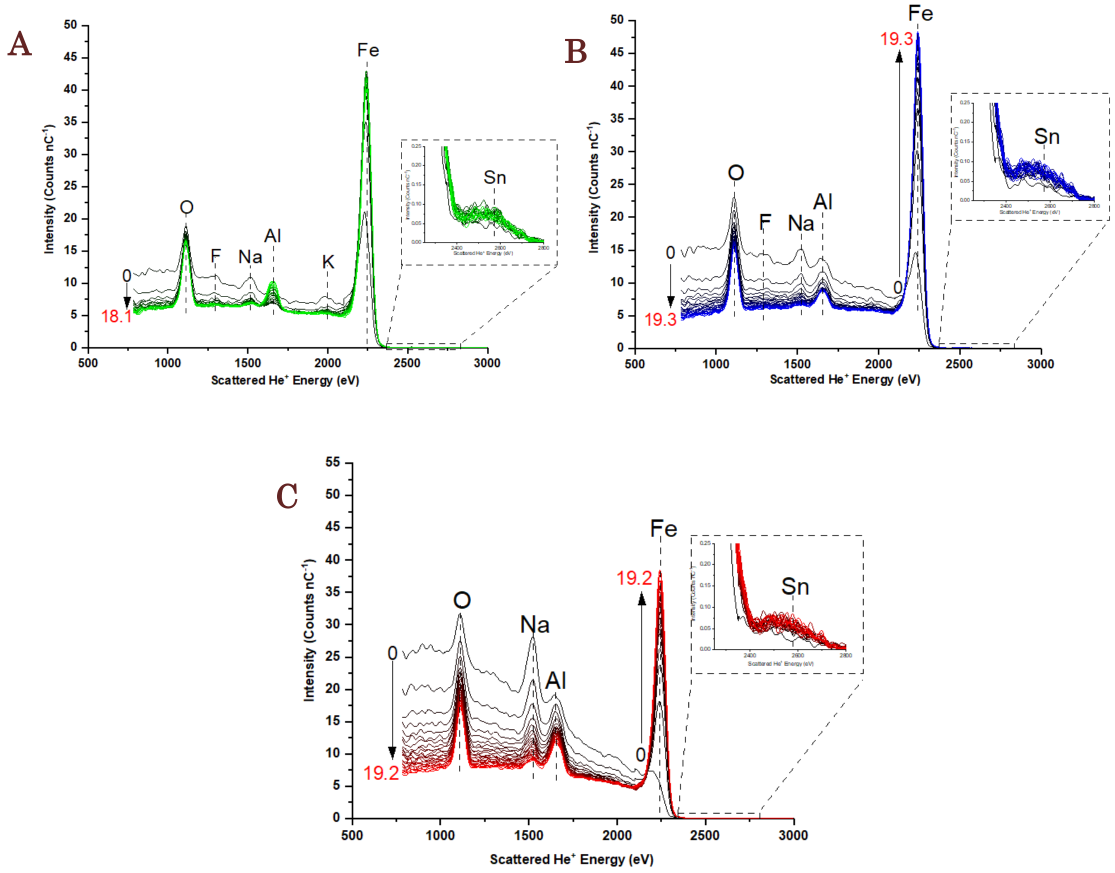

Figure 63: Depth profiling for 5% gradient doped (high-low) Al_2O_3/Fe_2O_3, with A) no heat, B) Heat Treatment 1 and C) Heat Treatment 2. Experiment carried out by Dr Adrian Gardner, Stephenson Institute for Renewable Energy.

Overall, the LEIS results for GD are fairly consistent with the previous observations for these samples. The largest discrepancy between the uniform and gradient doped samples is the Na content following heating. For GD the intensity here is reduced from that of UD following both Heat Treatment 1 and

2. Al_2O_3 content is consistent between samples at 5%, indicating that the structure may play a role in ion migration. Some surface Na impurities are expected, similar to carbon layers, but there is a clear increase following heat treatment, indicating more is moving from the glass here. The presence of thicker layers likely inhibits this movement to a degree, resulting in the slight changes observed for Na and Sn.

6.6.3 Gradient Doping with TiO_2: LEIS

The LEIS surface spectra of TiO_2 high-low gradient doped samples highlights some changes compared to the aluminium doped samples (Figure 64). The baseline trends for O, Na and Fe similar to those observed for the other samples, with and without heat treatment. Surface Fe is suppressed after high heat exposure, indicating an almost complete surface layer consisting of labile elements such as Na and K. Titanium can be found following heat exposure, as well as a small, yet present near surface Sn peak.

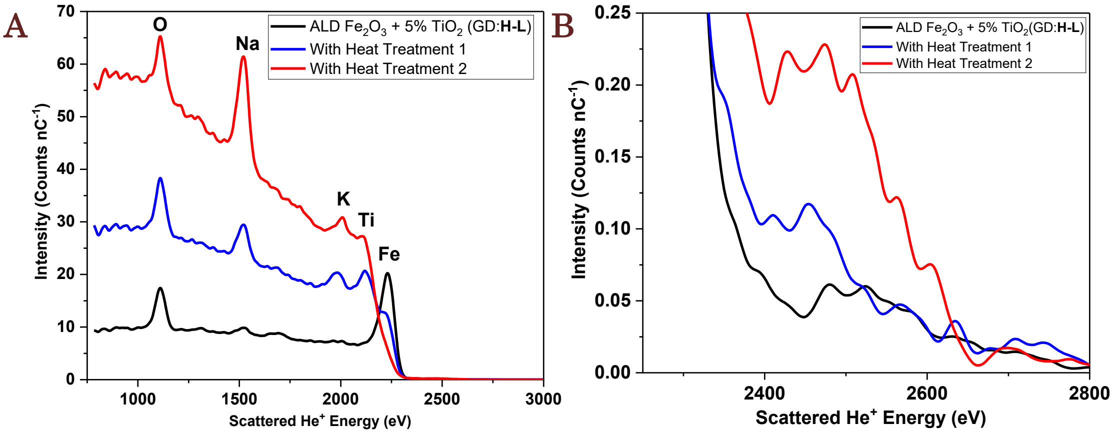

Figure 64: A) LEIS surface spectra for 5% TiO_2 gradient doped (high-low) samples across different heat parameters. B) Zoomed in surface spectra across Sn region. Experiment carried out by Dr Adrian Gardner, Stephenson Institute for Renewable Energy.

Dynamic depth profiling of these samples follows similar trends to those seen previously for Al doped samples (

Figure 65). Sputtering of the as-deposited sample showed no titanium presence in the unheated sample, indicating the titanium has not moved within the structure. Once heated, titanium can be observed in increasing amounts with each additional sputter treatment.

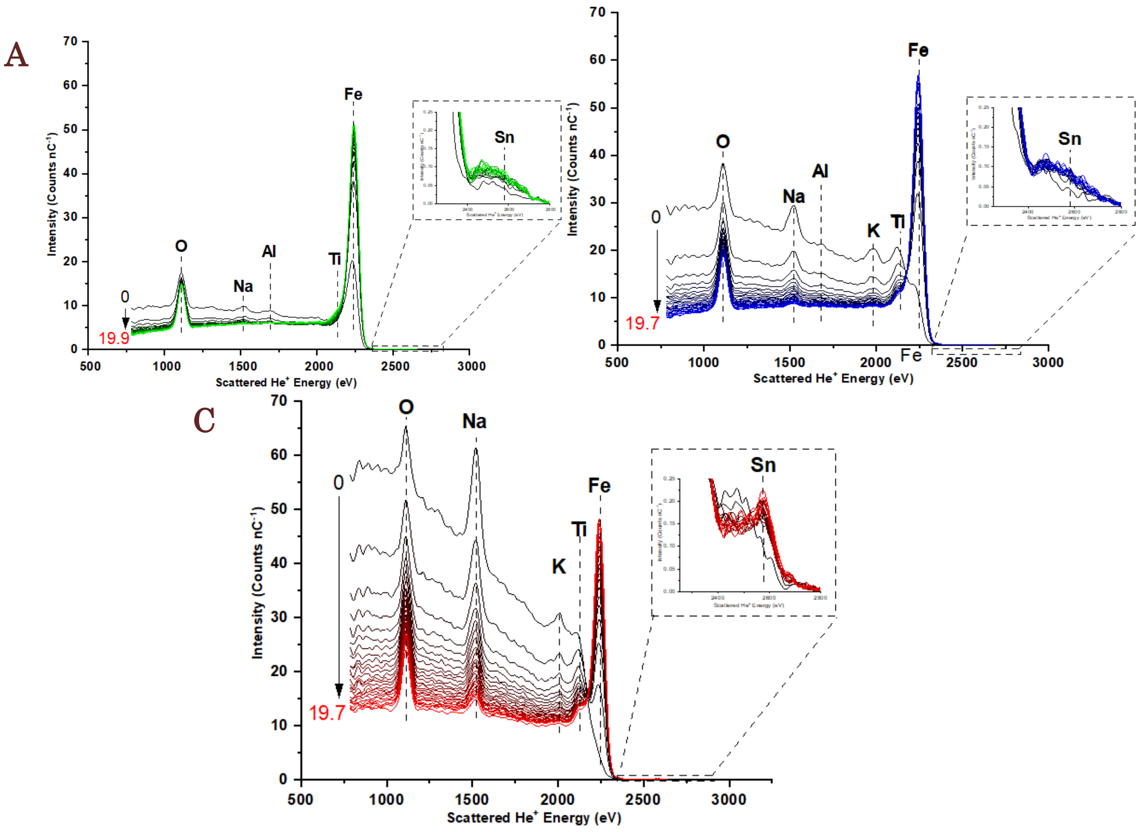

Figure 65: Depth profiling for 5% gradient doped (high-low) TiO$_2$/Fe$_2$O$_3$, with A) no heat, B) Heat Treatment 1 and C) Heat Treatment 2. Experiment carried out by Dr Adrian Gardner, Stephenson Institute for Renewable Energy.

Peak shape is important again here. Previous experiments have presented a broadened Sn peak, indicating Sn is present somewhere below the surface. Direct collisions however present as a sharper spectral peak, versus the near-collision broader peaks that result from non-discrete energy loss and scattering.[338,374] This slight Sn peak suggests that some degree of migration has occurred for the titanium doped sample, whereas this cannot be seen for aluminium doped samples. Possibly this alludes to a blocking action caused by the increased aluminium that does not exist for the titanium doped samples. Notably, this Sn peak is comparable in shape and intensity to the Fe_2O_3 sample with the 0.4nm aluminium underlayer. A small peak was seen for the UD sample, but the intensity was ~ 0.2 nC^{-1}, which was much lower than that observed for the electrodeposited hematite (14 nC^{-1}).

The combination of these results indicates that (following Heat Treatment 2) Sn does not reach the surface for Al % doped ALD hematite samples, but tiny amounts of Sn can be found for the samples doped with Ti/with Al underlayers. The literature consensus is that heat treatments > 700°C drive Sn migration from the FTO, resulting in Sn-doping and improved photo performance as a result.[243,339,375,376] This was observed in Chapter 5 for the thicker electrodeposited hematite sample, with a notable Sn peak. The observations for the Al-doped films do not align with this consensus however, as Sn is not present in any observable quantity. Broad peaks are observable that indicate it is present further beneath the sputtered layers – but as these are thin films, it is difficult to ascertain if that is due to a degree of low-level Sn migration or the FTO substrate itself.[247] As for the other ALD-Fe2O3 samples, there is also an indication of reduced Sn migration. Overall, the improvement in onset and photocurrent for the Al doped samples following the 750°C heat treatment here cannot be attributed to Sn-doping, which is an interesting conclusion for heat treated hematite.

6.7 Additional Modifications

In this project, underlayers and interlayers have been tested as a method of improvement, with surface layers excluded. However, surface modifications are a more common and usually favourable adaptation for Fe_2O_3 photoanodes, improving charge transfer and recombination due to surface passivation. For most samples, they offer benefits due to the ease of application; applying a surface layer to an existing sample is easier to achieve than adding layers below/within the structures.

Cobalt phosphate complex (CoPi) surface layers in particular are a quick, easy modification that can be added to a photoanode to improve electrochemical properties. CoPi are added by electrochemical deposition, wherein the sample is submerged in CoPi solution, and a potential applied to create adherence. The thickness of the layer can be controlled by increasing the voltage or the duration of treatment.[377] These layers can improve photocurrent and onset potential for various semiconductors, but typically diminish in alkaline solution over time.[378]

For this project, adding a CoPi layer is a quick way to test possible further adaptations of the samples produced. As the 5% Al_2O_3 uniform doped sample exhibited an impressively low onset potential, a CoPi surface layer could further indicate the value of these samples with additional testing.

6.7.1 Experimental

A CoPi overlayer was added to a 5% UD Al_2O_3/Fe_2O_3 sample via the deposition method detailed by Bouhjar et al., 2019.[246] Here, 0.5 mM cobalt nitrate was mixed with 0.1M potassium phosphate buffer solution to create the electrolyte. The UD photoanode was then submerged, with the same cell setup as used for electrochemical measurements (Ag/AgCl reference, Pt counter, 150W Xe lamp). A voltage of 0.9 $V_{Ag/AgCl}$ was applied with a constant current of 6 $mA.cm^{-2}$ for 300 seconds, to produce a thin surface film. Deposition times between 100-750 seconds have been highlighted as beneficial, with reduced benefits as layers gain excessive thickness.[377,379] Following deposition the sample was rinsed with distilled water and air dried.

6.7.2 CoPi Layer Results

A CoPi overlayer offered an immediate photoelectrochemical improvement (Figure 66). Photocurrent almost doubled, reaching 0.36 $mA.cm^{-2}$, while onset decreased further, reaching -0.41 $V_{Ag/Ag/Cl}$ from -0.29 $V_{Ag/Ag/Cl}$.

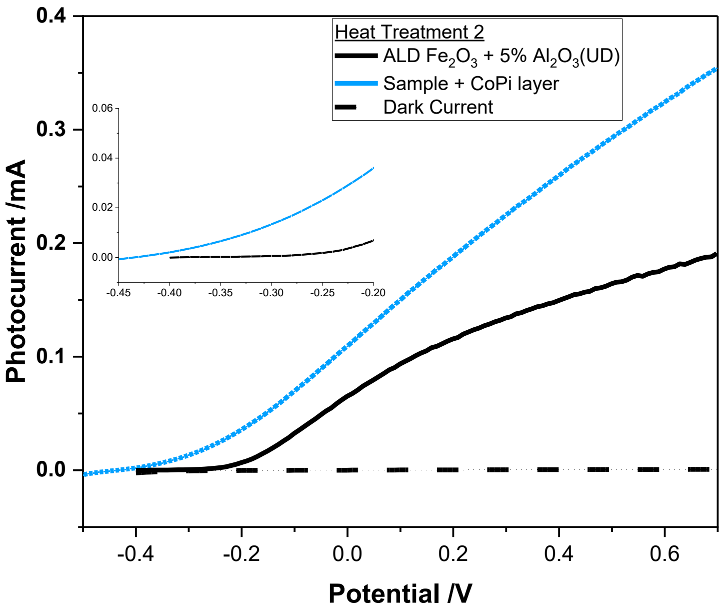

Figure 66: LSV for 5% uniform doped Al_2O_3/Fe_2O_3*, with (blue) and without (black) a CoPi overlayer.*

There was no obvious change in optical absorption properties with UV-Vis spectroscopy (Figure 67). Peaks and troughs are aligned, with no changes to overall shape for the uncoated and coated samples. A lack of blue/red shift indicates that there have been no alterations to bandgap.[380] The increase in absorption is expected with the slightly increased film thickness. Overall, this is a standard UV-Vis spectra for CoPi overlayers on Fe_2O_3; CoPi layers typically do not alter the optical properties of Fe_2O_3.[381,382]

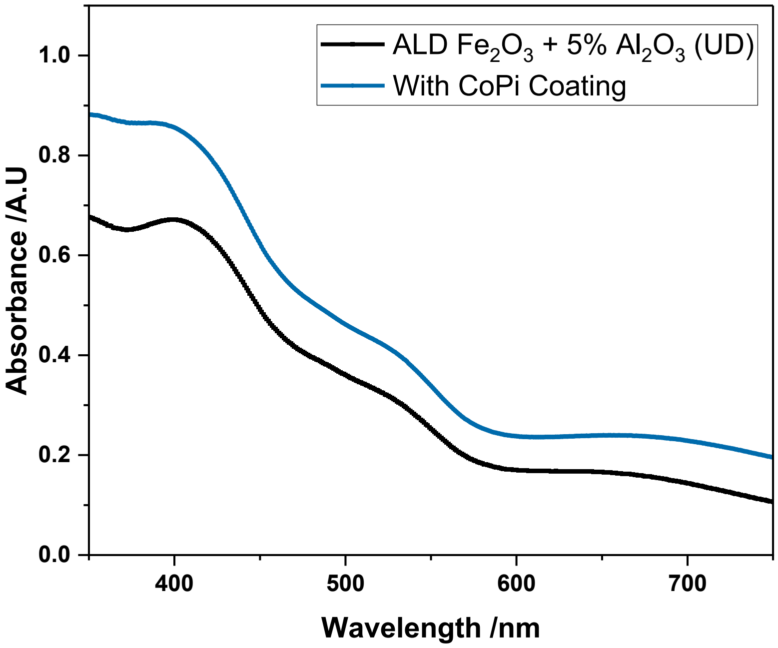

Figure 67: UV-Vis Spectra for 5% uniform doped Al_2O_3/Fe_2O_3, with (blue) and without (black) a CoPi overlayer.

This data aligns with the method of action of CoPi overlayers, wherein they behave as a co-catalyst, with the Co oxidation state varying between 3+ and 2+. The Co acts as a hole acceptor, regenerating following charge transfer.[383] Hence, CoPi layers act as a charge mediator, reducing the impact of Fe_2O_3 surface trap states and lowering the recombination rate.[384] This behaviour explains the improved photocurrent and onset data obtained, with vast improvements seen for both.

The low onset of 0.61 V_{RHE} in particular is impressive for hematite photoanodes. Previous records have hovered in this region, with 0.62 V_{RHE} the lowest value found for more traditional hematite growth methods.[376,385] A lower onset potential of ~0.45 V_{RHE} has been achieved through a regrowth method.[34] This process requires the partial destruction of the hematite sample in acidic media, with simultaneous addition of $NiFeO_x$. A further study accomplished an onset potential of 0.58 V_{RHE} for Fe_2O_3 produced by heating iron foil in a H_2-O_2 flame.[386] When assessing the role of dopants on performance, these methods are not comparable to traditional doping in which dopant layers are added to untouched Fe_2O_3. While this is not the overall record for lowest hematite onset, this result highlights the low onset achievable for aluminium doped, surface modified samples. Further study in this area may highlight additional benefits to this doping composition.

6.9 Conclusions

The results of this chapter highlight a few interesting observations for Al gradient and uniform doped samples, as well as Ti gradient doped hematite. A stepwise improvement in onset potential was seen for UD Al samples, with samples requiring heat activation. This trend was also observed for the gradient doped Al samples, with a defined onset potential improvement compared to pristine hematite following Heat Treatment 2.

High to low gradient doping was shown to offer improvement over low-high GD, for both Al and Ti-doped hematite. For high-low GD Al hematite, there was also an improved photocurrent versus the uniform doped sample, which suggests that gradient doping offers the best of both worlds for hematite photoanodes. CoPi surface layers also brought additional benefits when added to a 5% Al UD doped sample, with a very low onset potential of 0.61 V_{RHE} achieved. This indicates that these samples can be further modified to enhance photoelectrochemical performance.

Finally, LEIS analysis for these samples showed migration of Ti and Al for the respective samples, with labile atoms such as Na, F and K visible in varying amounts. Most notably, Sn suppression was observed for these samples, as indicated previously for the underlayer samples. Particularly, the Al % doped samples showing no obvious Sn presence when compared to other hematite production methods. This has implications for the high temperature heat treatment of these samples, with Sn migration ruled out as the reason behind the photoelectrochemical improvements seen.

References

1 R. S. Balmer, I. Friel, S. Hepplestone, J. Isberg, M. J. Uren, M. L. Markham, N. L. Palmer, J. Pilkington, P. Huggett and S. Majdi, *J. Appl. Phys.*, 2013, **113**, 33702.

2 J. J. Harris, *J. Mater. Sci. Mater. Electron.*, 1993, **4**, 93–105.

3 R. R. Gade, 2015.

4 T. Arroval, L. Aarik, R. Rammula, V. Kruusla and J. Aarik, *Thin Solid Films*, 2016, **600**, 119–125.

5 M. Rooth, A. Johansson, K. Kukli, J. Aarik, M. Boman and A. Hårsta, *Chem. Vap. Depos.*, 2008, **14**, 67–70.

6 M. Wang, F. Ren, J. Zhou, G. Cai, L. Cai, Y. Hu, D. Wang, Y. Liu, L. Guo and S. Shen, *Sci. Rep.*, 2015, **5**, 12925.

7 Z. Luo, C. Li, S. Liu, T. Wang and J. Gong, *Chem. Sci.*, 2017, **8**, 91–100.

8 D. Chen and Z. Liu, *ChemSusChem*, 2018, **11**, 3438–3448.

9 O. Zandi, B. M. Klahr and T. W. Hamann, *Energy Environ. Sci.*, 2013, **6**, 634–642.

10 H. Zhang, D. Li, W. J. Byun, X. Wang, T. J. Shin, H. Y. Jeong, H. Han, C. Li and J. S. Lee, *Nat. Commun.*, 2020, **11**, 1–11.

11 K.-H. Ye, P. Hu, K. Liu, S. Tang, D. Huang, Z. Lin, S. Zhang, Y. Huang, H. Ji and S. Yang, *Sol. RRL*, 2022, **6**, 2100701.

12 Z. Zhang, Y. Guo and J. Robertson, *Appl. Phys. Lett.*, 2019, **114**, 161601.

13 S. Hejazi, M. Altomare and P. Schmuki, 2020, **234**, 615–631.

14 E. O. Filatova and A. S. Konashuk, *J. Phys. Chem. C*, 2015, **119**, 20755–20761.

15 H. K. Dunn, J. M. Feckl, A. Müller, D. Fattakhova-Rohlfing, S. G. Morehead, J. Roos, L. M. Peter, C. Scheu and T. Bein, *Phys. Chem. Chem. Phys.*, 2014, **16**, 24610–24620.

16 Z. Zhang, Y. Guo and J. Robertson, *Microelectron. Eng.*, 2019, **216**, 111039.

17 U. S. Khan, A. Manan, N. Khan, A. Mahmood and A. Rahim, *Mater. Sci.*, 2015, **33**, 278–285.

18 F. Fajaroh, H. Setyawan, W. Widiyastuti and S. Winardi, *Adv. Powder Technol.*, 2012, **23**, 328–333.

19 M. Lübbe, A. M. Gigler, R. W. Stark and W. Moritz, *Surf. Sci.*, 2010, **604**, 679–685.

20 S. C. Pang, W. H. Khoh and S. F. Chin, *J. Mater. Sci.*, 2010, **45**, 5598–5604.

21 H. Liu, X. Fan, Y. Li, H. Guo, W. Jiang and G. Liu, *J. Environ. Chem. Eng.*, 2023, **11**, 109224.

22 R. Zhang, Y. Fang, T. Chen, F. Qu, Z. Liu, G. Du, A. M. Asiri, T. Gao and X. Sun, *ACS Sustain. Chem. Eng.*, 2017, **5**, 7502–7506.

23 P.-F. Liu, C. Wang, Y. Wang, Y. Li, B. Zhang, L.-R. Zheng, Z. Jiang, H. Zhao and H.-G. Yang, *Sci. Bull.*, 2021, **66**, 1013–1021.

24 P. Sharma, J.-W. Jang and J. S. Lee, *ChemCatChem*, 2019, **11**, 157–179.

25 R. Mazzaro, S. Boscolo Bibi, M. Natali, G. Bergamini, V. Morandi, P. Ceroni and A. Vomiero, *Nano Energy*, 2019, **61**, 36–46.

26 S. S. Shinde, R. A. Bansode, C. H. Bhosale and K. Y. Rajpure, *J. Semicond.*, 2011, **32**, 13001.

27 B. Z. Yong, .

28 X. Li, N. C. Fan and H. J. Fan, *Chem. Vap. Depos.*, 2013, **19**, 104–110.

29 Z. Luo, T. Wang, J. Zhang, C. Li, H. Li and J. Gong, *Angew. Chemie Int. Ed.*, 2017, **56**, 12878–12882.

30 A. Lale, E. Scheid, F. Cristiano, L. Datas, B. Reig, J. Launay and P. Temple-Boyer, *Thin Solid Films*, 2018, **666**, 20–27.

31 Y. Ling and Y. Li, *Part. Part. Syst. Charact.*, 2014, **31**, 1113–1121.

32 C. D. Wagner, A. V Naumkin, A. Kraut-Vass, J. W. Allison, C. J. Powell and J. R. J. Rumble, *Available online http/srdata. nist. gov/xps/(accessed 12 May 2022).*

33 S. S. Shinde and K. Y. Rajpure, *J. Solid State Chem.*, 2010, **183**, 2886–2894.

34 P. Wang, C. Ding, D. Li, Y. Cao, Z. Li, X. Wang, J. Shi and C. Li, *Dalt. Trans.*, 2022, **51**, 9247–9255.

35 E. Kim, S. Kim, Y. M. Choi, J. H. Park and H. Shin, *ACS Sustain. Chem. Eng.*, 2020, **8**, 11358–11367.

36 F. Bouhjar, L. Derbali, B. Marí and B. Bessaïs, *Sol. Energy Mater. Sol. Cells*, 2019, **195**, 241–249.

37 D. K. Zhong, M. Cornuz, K. Sivula, M. Grätzel and D. R. Gamelin, *Energy Environ. Sci.*, 2011, **4**, 1759–1764.

38 S. Mizuno and H. Yao, *J. Magn. Magn. Mater.*, 2021, **517**, 167389.

39 Q. Liu, C. Chen, Y. Wei, L. Jiang, L. Wang and G. Li, *J. Alloys Compd.*, 2023, **947**, 169673.

40 L. Fu, H. Yu, C. Zhang, Z. Shao and B. Yi, *Electrochim. Acta*, 2014, **136**, 363–369.

41 K. C. Bedin, D. N. F. Muche, M. A. Melo Jr., A. L. M. Freitas, R. V Gonçalves and F. L. Souza, *ChemCatChem*, 2020, **12**, 3156–3169.

42 D. Li, R. Wei, H. Yin, H. Zhang, X. Wang and C. Li, *Chem. Sci.*, 2023, **14**, 1861–1870.

43 C. Du, X. Yang, M. T. Mayer, H. Hoyt, J. Xie, G. McMahon, G. Bischoping and D. Wang, *Angew. Chemie Int. Ed.*, 2013, **52**, 12692–12695.

44 C. Li, Z. Luo, T. Wang and J. Gong, *Adv. Mater.*, 2018, **30**, 1707502.

45 J.-W. Jang, C. Du, Y. Ye, Y. Lin, X. Yao, J. Thorne, E. Liu, G. McMahon, J. Zhu, A. Javey, J. Guo and D. Wang, *Nat. Commun.*, 2015, **6**, 7447.

46 J. Han, X. Zong, Z. Wang and C. Li, *Phys. Chem. Chem. Phys.*, 2014, **16**, 23544–23548.

7.0 Conclusions and Future Work

In this thesis, plasma enhanced atomic layer deposition (ALD) is used to produce hematite, α-Fe_2O_3, for use in a photoelectrochemical (PEC) cell. In this role, hematite photoanodes are employed to assist in the photolysis of water, acting as a photoanode and driving forward the oxygen evolution reaction (OER).

The mechanisms of this reaction and the issues surrounding it were explored in Chapter 2, along with the role of semiconductors in PEC cells and the qualities that define a good photoanode. Hematite and the problems of hematite photoanodes were also covered, as well as some of the common methods used to address these difficulties. Nanostructuring in particular was highlighted as a possible solution to the electron transport problems that hematite was found to have, as well as the addition of dopants and layers to the photoanodes to further boost performance.

Chapter 4 discussed the development of a plasma enhanced ALD process to produce thin hematite films using a ferrocene precursor and an O_2/Ar plasma. This used a heated, custom built precursor pot with a vapour push mechanism to combat the low vapour pressure exerted by the ferrocene powder. This process was honed by exploring the effects of altering different experimental parameters, with a final growth sequence of 2.5s-5s-5s-4s. A 50 W plasma power setting and 250°C platen temperature was found to be ideal for this process, though substrate inhibited growth could be seen at higher thicknesses.

The photoelectrochemical performance of the ALD hematite was explored in Chapter 5, along with the effects of heat treating the samples and adding an aluminium oxide (Al_2O_3) underlayer. Heat treatment was seen to increase performance of the pristine hematite samples, with the Al_2O_3 underlayers further boosting this. In particular, thin underlayers were beneficial, with 0.5 nm Al_2O_3 exhibiting vast improvement over the pristine hematite. Underlayers exceeding 0.5 nm were found to offer some limited improvement in onset potential compared to the unmodified Al_2O_3 though were not as beneficial as thinner layers.

Chapter 6 studied the effect of adding more aluminium to the samples, with the use of layer doping. Aluminium layers were added in between sheets of hematite in various thicknesses, with heat treatments used to diffuse the layers. These samples required heat to activate them, as the aluminium layers reduced charge transfer through the bulk. Larger amounts of aluminium were once again found to be non-favourable, while lower amounts massively improved the onset potential of the hematite photoanodes. This came at a cost of photocurrent however, which was reduced from that of pristine hematite for the Al doped samples. The structure in which the aluminium was added was then varied, with a gradient doping strategy tested for 5% Al_2O_3 doped hematite. Here, high-low gradient doping was shown to offer a combined improvement in both onset and photocurrent compared to uniform doped samples, indicating that the layer structure is important for photoelectrochemical performance. This was further confirmed by testing titanium gradient doped samples, which showed this same favoring of high-low gradient doping, though not to the same magnitude as for the Al.

Additionally, a cobalt phosphate complex (CoPi) surface layer was added to test the effects of further modifications. This was assessed for the heat treated (to 750°C) 5% Al uniform doped sample, which previously had showed an impressive onset potential of -0.29 $V_{Ag/AgCl}$ (0.73 V $_{RHE}$). The addition of the CoPi surface layer improved both onset and photocurrent for this sample, with an impressive onset potential of -0.41 $V_{Ag/Ag/Cl}$ (0.61 V_{RHE}) obtained. Overall this indicates that surface modifications offer further improvements for these samples.

Finally, Low energy ion scattering (LEIS) was explored to assess possible compositional differences in the films produced, with both surface and depth profiles explored. This highlighted that heat exposure at 550°C drove the migration of labile ions such as Na, as well as Al and Ti from the respective doped films. Further migration could be observed for 750°C heat treatments, highlighting the role of temperature in altering the compositional formations of the films. Most interesting for the LEIS results was the absence of Sn migration following the 750°C heat treatment. Miniscule amounts were observed for the underlayer samples and Ti-doped gradient doped samples, but when compared to a thicker electrodeposited sample the lack of Sn migration was apparent. For the Al % doped samples, no defined Sn peak was observed, indicating that Sn was not present in the layers studied. This suggests that the improvement seen for these films following the 750°C heat treatment was not caused by Sn-doping.

Instead, the improvement here was suggested to be due to Al doping effects, with increased charge carriers from the glass also playing a role.